Theoretical and Numerical Study of Air Entrainment and Bubble Size Distribution in Strong Free-surface Turbulent Flow at Large Froude and Weber Number

by

Xiangming Yu

B.S., Shanghai Jiao Tong University (2010)
S.M., University of Texas at Austin (2012)

Submitted to the Department of Mechanical Engineering
in partial fulfillment of the requirements for the degree of

Doctor of Philosophy

at the

MASSACHUSETTS INSTITUTE OF TECHNOLOGY

September 2019

Author .....
Department of Mechanical Engineering
July 31, 2019

Certified by .....
Dick K. P. Yue
Philip J. Solondz Professor of Engineering
Professor of Mechanical and Ocean Engineering
Thesis Supervisor

Accepted by .....
Nicolas G. Hadjiconstantinou
Chairman, Department Committee on Graduate Theses

Theoretical and Numerical Study of Air Entrainment and Bubble Size Distribution in Strong Free-surface Turbulent Flow at Large Froude and Weber Number

by

Xiangming Yu

Submitted to the Department of Mechanical Engineering
on July 31, 2019, in partial fulfillment of the
requirements for the degree of
Doctor of Philosophy

Abstract

Strong turbulence near an air-water interface, characterized by large Froude (Fr) and Weber number (We), leads to significant interactions and exchanges between gas and liquid, resulting in measurable air entrainment. Air entrainment influences a number of physical processes in the nature, including air-sea gas transfer, production of the sea-salt aerosol and scavenging of biological surfactant. The key factor in controlling these processes is the size distribution of entrained bubbles. However, the underlying mechanisms/physics of air entrainment driven by free-surface turbulence (FST) and the resulted bubble size distribution still remain unclear. Therefore, detailed studies on air entrainment in strong free-surface turbulence (SFST) are of fundamental scientific interest. With recent interest in modeling the white bubbly water in ship wakes, these studies are also of practical importance to the design and analysis of modern surface vessels.

In this thesis, we perform both theoretical and numerical studies on air entrainment and bubble size distribution in SFST at large Fr and We. The thesis work 1) characterizes the unique turbulence characteristics of SFST; 2) quantifies the entrainment volume and the corresponding size distribution of SFST air entrainment; 3) elucidates the mechanisms/physics of the bubble size distribution of SFST entrainment; 4) provides useful insight and guidance to the development of sub-grid air entrainment models.

A new theoretical model considering the bubble size spectrum $\mathcal{N}_a^E(r)$ of SFST entrainment is derived in this thesis. We provide both a detailed physical derivation by connecting the energy of near-surface turbulence and the energy required for bubble entrainment, and a direct dimensional argument for the model. Depending on the bubble radius r, there exist two regimes of $\mathcal{N}_a^E(r)$, separated by a scale r_0. For $r > r_0$, bubble entrainment is under strong effects of gravity g relative to surface tension σ/ρ, and $\mathcal{N}_a^E(r) \propto g^{-1}\epsilon^{2/3}r^{-10/3}$, where ϵ is the turbulence dissipation rate. For $r < r_0$, surface tension is more important and $\mathcal{N}_a^E(r) \propto (\sigma/\rho)^{-1}\epsilon^{2/3}r^{-3/4}$. From the model,

we show that $r_0{=}r_c{=}\frac{1}{2}\sqrt{\sigma/\rho g}$, the capillary length scale, and not the Hinze scale r_H as is generally assumed. For air-water interface and earth gravity, $r_c \approx 1.5$mm. The theoretical work also provides for an $\epsilon{-}r$ entrainment regime map which identifies a critical dissipation rate ϵ_{cr} (constant for given g and σ/ρ) above which there is appreciable air entrainment, thus separating SFST and weak FST (WFST).

A direct numerical solver is developed for the three-dimensional two-phase incompressible Navier-Stokes equations with a fully nonlinear interface resolved by the conservative volume-of-fluid method (cVOF). We perform DNS of a canonical FST flow with turbulent kinetic energy supplied by a sheared underlying bulk water flow. Different than WFST with anisotropic near-surface turbulence and distinct inner/outer surface layers, the inner/outer surface layers disappear in SFST, resulting in nearly isotropic turbulence with $\sim k^{-5/3}$ scaling of turbulence kinetic energy near the interface. To obtain the bubble size distribution of SFST entrainment, we develop a cavity/bubble identification scheme based on the union-find algorithm to identify individual entrained bubbles in the bulk flow and calculate the corresponding bubble size spectrum from DNS results. The theoretical model of $\mathcal{N}_a^E(r)$ is confirmed by high-fidelity DNS results: the respective power-laws of $\mathcal{N}_a^E(r) \propto r^{-10/3}$ and $r^{-4/3}$ for $r > r_0$ and $r < r_0$; the value $r_0{=}r_c$; the scaling $\mathcal{N}_a^E(r) \propto g^{-1}$ under strong g and $\mathcal{N}_a^E(r) \propto (\sigma/\rho)^{-1}$ under strong σ/ρ; the scaling $\mathcal{N}_a^E(r) \propto \epsilon^{2/3}$; and the predictions of the $\epsilon{-}r$ entrainment regime map.

In SFST, coherent vortical structures near the free surface are observed to induce entrainment events. To understand vortex induced air entrainment, we consider two vortex structures, a pair of counter-rotating vortices and a ring-structured vortex, and perform numerical simulations of the interactions of the two vortex structures with the free surface. The entrainment volume V is found to scale as g^{-1} for entrainment under strong g relative to σ/ρ. V scales as $(\sigma/\rho)^{-1}$ when σ/ρ becomes more important. The two scalings are found to be consistent with those obtained in the SFST flow. We also find a linear dependence of the entrainment volume on an averaged quantity of vorticity flux which can be used for modeling of the sub-grid terms of entrainment in the two-phase RANS governing equations in order to achieve closures.

Thesis Supervisor: Dick K. P. Yue
Title: Philip J. Solondz Professor of Engineering
Professor of Mechanical and Ocean Engineering

Acknowledgments

First of all, I would like to express my sincere gratitude to my supervisor Prof. Dick K.P. Yue for his continuous support and guidance during the last seven years. He does not only educate me with fluid mechanics, but inspires me to be a good researcher.

I also want to thanks Dr. Kelli Hendrickson for her help during my graduate study. Instead of my co-supervisor or mentor, she is more like a good friend and a big sister. She taught me everything about computational fluid mechanics when I first joined the group. More importantly, she always encourages me to stay optimistic and helps me go through one of the toughest periods.

I appreciate my other two committee members, Prof. Emilio Baglietto and Prof. Lydia Bourouiba, for their insightful inputs and suggestions to this thesis work. I have been greatly inspired through the discussion with them in my committee meetings.

My sincere gratitude also goes to every group member of VFRL. It is not possible to name them all, but I would like to especially thank: Yuming Liu, Areti Kiara, Grgur Tokic, Bryce Campbell, Wenting Xiao, Yulin Pan, Meng Shen, Yusheng Qi, Chengxi Li, Sha Miao, Jun Fan, Emma Edwards, Joao Seixas de Medeiros, Cheng Li, and Mary Thompson. Thanks everyone for making the group as a family for me.

The seven-year study at MIT is the most memorable experience in my lift. During the time, I get the chance to know some of the most valuable friends of mine. I would like to thank Wujie Huang, Yu Xin, Jiexi Zhang, Rong Zhu, Hongyu Yang, Xing Huang, Xuntuo Wang, Yongbin Sun, Xiaoyu Wu, Hongyu Wang, Yang Liu, Yan Han, Xi Rong, Qing Zhao, You Wu, Zhibiao Rao, Dixia Fan, Yu Zhang, Yu Ma, Leixin Ma. Thanks all for their accompanies and encouragements during my stay at MIT.

Finally, I would like to express my deepest thanks to my family, my parents Xiaosheng Yu and Guixia Liu, and my wife Longyue Yu. Without their selfless love and support, I could have never survived and made today's achievements.

Contents

List of Figures

List of Tables

Chapter 1

Introduction

Strong free-surface turbulence (SFST) leads to significant interactions between gas and liquid resulting in surface phenomena not observed in weak free-surface turbulence (WFST). When free-surface turbulence (FST) is energetic enough to overcome the stabilizing effects of gravity and surface tension, the free surface becomes strongly distorted, resulting in surface waves, projections, dimples and finally surface breakups. The surface breakups create complex two-phase gas-liquid mixtures such as drops and entrained bubbles near the interface. The study of SFST, including the turbulence characteristics near a highly distorted free surface and air entrainment driven by SFST, are of fundamental scientific interest. With recent interest in modeling the white bubbly water in ship wakes, the study of SFST and corresponding air entrainment are also of practical importance to the design and analysis of modern surface vessels.

1.1 Strong free-surface turbulence

Brocchini & Peregrine (2001*a*) proposed a diagram of (L, ϵ)-plane to describe a wide range of free surface deformations when turbulence exists in the bulk liquid near the free surface (neglecting dynamic effects of the gas). By considering the stabilizing effects of gravity and surface tension against the free-surface disturbance due to turbulence, they defined different flow regimes in which the free surface exhibits distinct

features. When turbulence is sufficiently strong, neither gravity nor surface tension can maintain the cohesion of the surface, resulting in droplets and air entrainment. This near-surface two-phase flow regime or the "strong turbulence regime" occurs under large Froude (Fr) and Weber (We) numbers. On the other hand, when turbulence is relatively weak, the free surface remains nearly flat due to the stabilizing effect of either gravity or surface tension. This regime or the "weak turbulence regime" corresponds to small Froude or Weber numbers.

Many studies on WFST in the weak turbulence regime have been performed numerically (Handler *et al.*, 1993; Pan & Banerjee, 1995; Borue *et al.*, 1995; Walker *et al.*, 1996; Shen *et al.*, 1999; Nagaosa, 1999; Fulgosi *et al.*, 2003; Guo & Shen, 2010; Yamamoto & Kunugi, 2011) and experimentally (Walker *et al.*, 1995; Smolentsev & Miraghaie, 2005; Savelsberg & van de Water, 2008, 2009). Hunt *et al.* (2011) performed a linearized rapid-distortion analysis to investigate viscous coupling of turbulence at a nearly flat interface. In WFST, the (almost) flat free surface has a large blockage effect, which strongly constrains the liquid movements normal to the surface, resulting in a blockage layer wherein horizontal velocity fluctuations are enhanced at the expense of vertical velocity fluctuations. Closer to the free surface where the dynamic boundary condition of (almost) zero stress is felt, a thinner surface layer characterized by fast variations of the horizontal vorticity components appears. The characteristic thicknesses and features of these two layers are summarized in figure 1-1 according to Shen *et al.* (1999). As expected, no air entrainment occurs in the weak turbulence regime.

In the strong turbulence regime with large Fr and We, Brocchini & Peregrine ($2001a$) pointed out that the surface blockage effect is significantly reduced due to the weak effects of gravity and surface tension. Therefore, turbulence near the free surface shows qualitatively different characteristics between WFST and SFST. Significantly, SFST is accompanied by large surface deformations, surface breakup/breaking, formation of liquid droplets and sprays, and entrainment of air cavities and bubbles. Compared to WFST, there exists little research on SFST in the strong turbulence regime. Hong & Walker (2000), Brocchini & Peregrine ($2001b$), and Brocchini (2002)

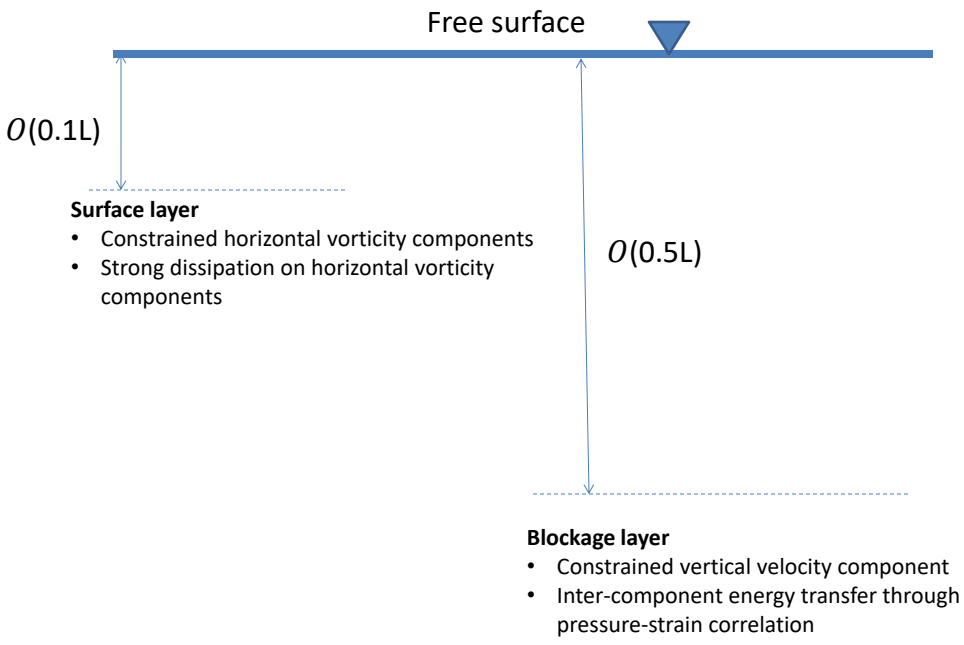

Figure 1-1: Schematic of the inner surface and outer blockage layers in WFST according to Shen *et al.* (1999), where L is the characteristic length scale.

derived a set of Reynolds-averaged governing equations and averaged boundary conditions for SFST. Mortazavi *et al.* (2016) performed DNS of a turbulent hydraulic jump where they found that the energy spectrum of near-surface turbulence approximately follows the Kolmogorov spectrum with a power-law of $k^{-5/3}$.

1.2 Air entrainment and bubble size distribution in SFST

Air entrainment occurs and plays important roles in both natural processes and engineering applications. For instance, air entrainment which occurs naturally in ocean breaking waves enhances the head and gas transfer across the air-sea interface, the production of the sea-salt aerosol and the scavenging of biological surfactant. In civil engineering, aeration cascades have been widely used in water treatment plants to increase oxygen concentration in water. There are various designs of aerator, but the

same idea is to generate strong free-surface turbulence (SFST), which significantly separates the interface and results in substantial entrainment bubbles of broad scales. The key factor of air entrainment in these processes is the size distribution of entrained bubbles which determines the contact area of gas and liquid. The specific bubble size distribution is believed to be mainly controlled by the free-surface turbulence (FST).

To better understand the bubble size distribution in turbulence, Garrett *et al.* (2000) performed a dimensional analysis in which the bubble size spectrum per unit volume $N(r)$ (of dimension L^{-4}) is assumed to depend only on turbulence dissipation rate ϵ (of dimension $L^2T{-}3$), the average rate of supply of air Q (of dimension T^{-1}) and the bubble radius r (of dimension L). The dimensional analysis suggests the following parameterization model:

$$N(r) \propto Q\epsilon^{-1/3}r^{-10/3} \tag{1.1}$$

Deane & Stokes (2002) pointed out that equation (1.1) is only valid for bubbles of radius larger than the Hinze scale r_H. For bubbles of radius smaller than r_H , surface tension becomes important, resulting in a different scale dependence than equation (1.1). They performed a similar dimensional analysis as Garrett *et al.* (2000) did, but considered bubbles of radius smaller than r_H. They assumed that $N(r)$ is a multiplicative function of surface tension σ, liquid density ρ, jet velocity v and bubble radius r. By that, they obtained that $N(r)$ scales as:

$$N(r) \propto Q(\sigma/\rho)^{-3/2}v^2r^{-3/2} \tag{1.2}$$

In addition, they measured $N(r)$ inside breaking waves in the laboratory. In the acoustic phase when bubbles are primarily formed, they detected two distinct regimes of size distribution, depending on bubble size. The critical radius r_a separating the two regimes was found to be around 1mm. They argued that r_a is the Hinze scale r_H. In the two regimes, $N(r)$ shows different power-laws with respect to r. For bubbles of radius larger than r_a, $N(r)$ scales as $r^{-10/3}$, consistent with the model by Garrett *et al.* (2000) in equation (1.1). For bubbles of radius smaller than r_a, their measurement

is close to the power-law of $N(r) \propto r^{-3/2}$ in equation (1.2). The scale dependence $N(r) \propto r^{-10/3}$ for large bubbles has been confirmed by other experimental measurements (Loewen *et al.*, 1996; Rojas & Loewen, 2007; Blenkinsopp & Chaplin, 2010) and numerical simulations (Wang *et al.*, 2016; Deike *et al.*, 2016) of breaking waves. For small bubbles, Rojas & Loewen (2007) and Wang *et al.* (2016) obtained similar result as Deane & Stokes (2002) did. However, the measurements by Blenkinsopp & Chaplin (2010) and Loewen *et al.* (1996) give very different results of $N(r)$. In the quiescent phase, $1.5s$ after the acoustic phase, the bubble plume evolves rapidly under the influences of bubble fragmentation, degassing and advection, and causes the evolution of $N(r)$.

Despite some success of the parameterization models of equation (1.1) and (1.2), there still exist three major concerns remaining unclear, leaving a gap of understanding of the mechanisms of SFST bubble entrainment. First of all, the current parameterization models were obtained by heuristic dimensional arguments. There is a lack of concrete physical/mechanistic arguments to support them. New physics-based models are necessary for two main reasons: 1) to improve our understanding of the basic mechanisms of bubble entrainment/formation in SFST. 2) to provide theoretical confirmation of the power-laws of $N(r)$ in the two bubble size regimes, especially in the small r regime. Experimental measurements and numerical simulations of bubbles in the small r regime are technologically difficult, and different results have been reported by researchers. Therefore, theoretical/physical models are of importance to provide guidance to find the correct power-law in this regime. Second, the negative/independent dependence of $N(r)$ on ϵ in equation (1.1)/(1.2) is questionable. Brocchini & Peregrine (2001*a*) pointed out that turbulence provides energy for bubble entrainment and formation in FST flows. Since ϵ reflects the turbulence intensity, larger ϵ is expected to result in an increase of the magnitude of $N(r)$. In another words, $N(r)$ is expected to scale as ϵ^m, where m is positive. Deike *et al.* (2016) argued that the average rate of supply of air Q is a function of ϵ, and the combination of Q and $\epsilon^{-1/3}$ in equation (1.1) should lead to a positive power of ϵ. Third, the argument that the transition scale r_a separating the two bubble size regimes is

the Hinze scale r_H may not be true. Even though this argument is generally assumed, there is no detailed study or concrete evidence to support that. r_H provides a critical length scale for bubble fragmentation in turbulence. Under the strong restoring forces of surface tension against turbulent fluctuations, bubbles of size smaller than r_H do not fragment. There is no doubt that r_H influences the formation of small bubbles and may affect $N(r)$ at small r. However, the detailed influences of r_H on $N(r)$ still remain unclear. It is too early to claim that r_a is r_H. Further theoretical and experimental studies are necessary to understand r_a.

Murzyn *et al.* (2007) and Chachereau & Chanson (2011) performed experimental studies on air entrainment in hydraulic jumps and found that it is highly dependent on Fr. They observed that air entrainment happens as Fr becomes larger than a critical value. In addition, the volume of air entrainment was observed to increase with increasing Fr. Chanson & Toombes (2003) measured the chord length of entrained bubbles in a supercritical open channel flow down a cascade. For bubble chord length greater than a critical scale, the probability density function shows a power-law (if re-plotted in log-log scale). However, further investigation on the detailed power-law slope and the underlying physics were not covered in their study.

1.3 Interaction of coherent vortical structures and free surface

Two recent studies of SFST by Yu *et al.* (2016) and André & Bardet (2017) showed that vortex structures near the free surface play an important role on entrainment events. Yu *et al.* (2016) performed DNS of a sheared free-surface turbulent flow. They observed that a vortex structure parallel to the surface induces a very local surface deformation and air is entrained into water when the free surface reconnects. André & Bardet (2017) studied a similar flow in the lab and further detected an entrainment process induced by a $\Omega-$shaped vortex structure. The interactions of these two vortex structures and the free surface are illustrated in the sketch figure 1-2.

However, in the previous studies on the interactions between vortical structures and the free surface, air entrainment was not generally covered. Shen *et al.* (1999) studied the features of FST under a nearly flat free surface through DNS. They identified a typical hairpin-shaped vortex structure and its interaction with the flat free surface. It was found that as the vortex structure approaches the free surface, its head part is dissipated quickly and then its two legs connect to the free surface. Zhang *et al.* (1999) considered a laminar oblique vortex ring impinging upon a nearly flat free surface. They observed the same vortex-surface connection process. Sarpkaya & Suthon (1991) experimentally investigated the problem of a vortex dipole rising to a free surface. They found that the rising vortex pair creates a local depression at the trailing of vortices, called a scar. Ohring & Lugt (1991) studied the same problem numerically. They found that surface tension and gravity stabilize the free surface when the surface interacts with the vortices. Yu & Tryggvason (1990) studied a two-dimensional flow with a shear layer (approximated by a two-dimensional point vortex) under a free surface. They found that the interaction of the vortex and the free surface is mainly controlled by Fr and the geometric parameters describing the initial vortex configuration. Even though air entrainment was not considered, the results in these studies clearly suggest that potential entrainment processes due to the strong interactions between vortical structures and the free surface. In general, when the vortices are strong enough to overcome the stabilization effects of gravity and surface tension, the free surface deforms significantly, leading to air entrainment eventually. The above cited work improves our understanding of the vortex-surface interactions and motivates further investigations on air entrainment in vortical flows.

In complex FST flows, numerous vortical structures are formed below the free surface. They are connected and interact with each other, so it is impossible to identify these vortical structures and predict the induced entrainment events. In the numerical simulations of FST flows using a two-fluid algorithm, a challenge problem remains due to the lack of comprehensive models for the sub-grid terms of entrainment in the governing equations. These sub-grid terms must be modeled in terms of averaged quantities in order to achieve closures. Ma *et al.* (2011) proposed an air entrainment

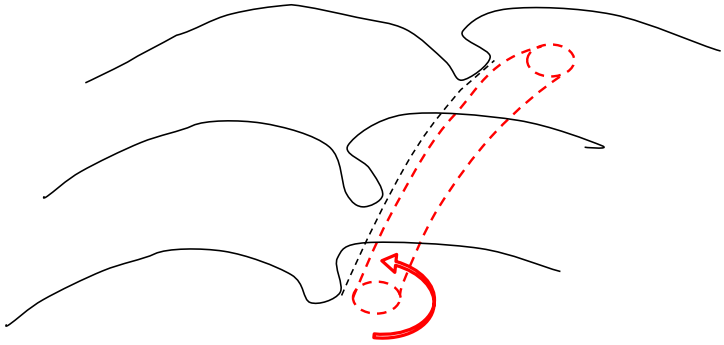

(a)

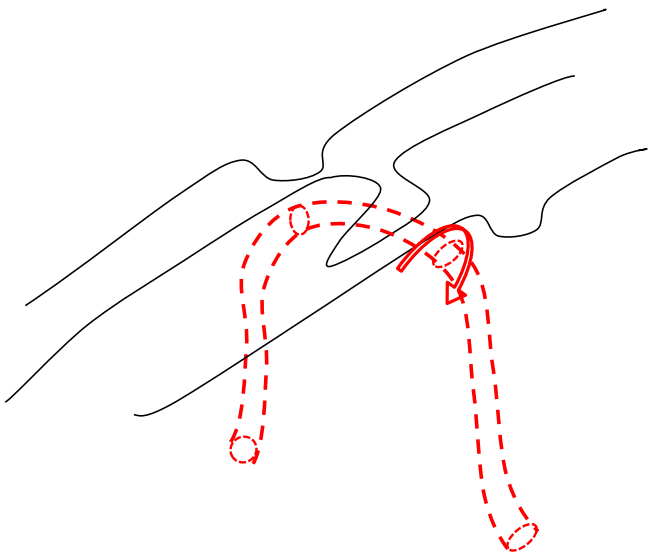

(b)

Figure 1-2: Sketch of potential air entrainment (· · ·) events caused by interactions between coherent vortical structures (- - -) and the free surface (——). (a) a vortex structure parallel to the free surface; (b) a Ω-shaped vortex structure.

model for RANS. In their model, they chose turbulent kinetic energy (TKE) as the averaged quantity to model the entrainment rate. Further research is necessary to find more appropriate quantities for the development and improvement of the closure models.

1.4 Thesis outline

This thesis focuses on the study of air entrainment in SFST. The main objectives of this thesis include:

- Understand the characteristics of near-surface turbulence in SFST flows.
- Understand air entrainment in SFST flows and the corresponding size distribution of entrained bubbles.
- Develop a physical/mechanistic model for bubble size distribution of SFST entrainment.
- Study air entrainment induced by near-surface vortex structures.

1.4.1 Characteristics of FST at large Fr and We

In the strong turbulence regime with large Fr and We, Brocchini & Peregrine (2001*a*) pointed out that the surface blockage effect is significantly reduced due to the weak gravity and surface tension relative to the disrupting effect of near-surface turbulence, leading to significant surface distortions. Turbulence near the deformed free surface, thus, shows unique characteristics. To understand the quantitative differences in the turbulence characteristics between SFST and WFST. We perform DNS of a WFST and a SFST case. Our numerical results confirm the strong blockage effect of the free surface in the WFST case by identifying the inner surface and the outer blockage layers. Due to the strong surface blockage effect, turbulence near the free surface shows strong anisotropy. In contrast, the two layers observed in WFST disappear in SFST due to the significant reduction of the surface blockage effect, leading to

nearly isotropic turbulence near the free surface. The corresponding turbulence energy spectrum follows the $k^{-5/3}$ Kolmogorov spectra of isotropic turbulence. The isotropy of near-surface turbulence in the SFST case is further confirmed by quantifying the anisotropy tensor and an isotropic parameter.

1.4.2 Air entrainment and bubble size distribution in SFST

In SFST case, turbulence is sufficiently strong that neither gravity nor surface tension can maintain surface cohesion, resulting in substantial air entrainment. We use a cavity identification algorithm based on the union-find algorithm to identify entrained bubbles in the bulk flow and calculate the corresponding bubble size spectrum (as a function of bubble radius r). In SFST, air entrainment is found to occur over a broad range of scales and the bubble size spectrum follows a power-law of $r^{-10/3}$. The spectrum then deviates from this power-law in time due to the fragmentation of entrained bubbles in turbulence. To quantify bubble fragmentation and provide qualitative insight into the evolution of bubble size spectrum in SFST , we consider a canonical problem of the fragmentation of a population of bubbles following a prescribed size spectrum in isotropic homogeneous turbulence (IHT). Combining the SFST entrainment and the bubble fragmentation, we provide a heuristic convolutional model to describe the bubble size spectrum in the bulk flow and have the model checked against DNS results.

1.4.3 Parameterization model for bubble size spectrum of SFST entrainment

A new parameterization model for the bubble size spectrum of SFST entrainment is proposed through a physical/mechanistic derivation by connecting the energy of turbulence and the energy required for entrainment. This model can be derived by a direct dimensional argument as well. The new model predicts two regimes of bubble size spectrum depending on the bubble radius r. In each of the regimes, the bubble size spectrum shows an unique power-law. The scale separating the two

regimes is the capillary length scale r_c . In the regime of large $r > r_c$, the bubble size spectrum shows a scaling of $g^{-1}\epsilon^{2/3}r^{-10/3}$, where g is gravity and ϵ is turbulence dissipation rate. In the regime of large $r < r_c$, the bubble regime shows a power-law of $(\sigma/\rho)^{-1}\epsilon^{2/3}r^{-4/3}$, where σ is the surface tension coefficient. The new model provides physical/mechanistic explanations and insights into the bubble size spectrum for the first time. It also confirms that the transition scale separating the two regimes is the capillary length scale r_c instead of the Hinze scale r_H. In addition, the upper and lower bounds of the bubble size of SFST entrainment are derived, and a diagram of (r, ϵ)-plane (analogous to the (L, q)-plane by Brocchini & Peregrine (2001*a*)) is proposed.

To provide support to the model predictions, we perform DNS of the SFST case over ranges of We and Fr. The dependencies of the magnitude of bubble size spectrum on g^{-1}, $(\sigma/\rho)^{-1}$ and $\epsilon^{2/3}$ are confirmed by our DNS results. The power-laws in the two regimes are also checked against the DNS results. The scale separating the two regimes is proved to be r_c instead of r_H.

1.4.4 Air entrainment induced by near-surface vortex structures

The new parameterization model describes the statistical distribution of the bubble size of SFST entrainment. However, the detailed entrainment processes/events still remain unclear. Recent studies by Yu *et al.* (2016) and André & Bardet (2017) showed that near-surface vortex structures play a key role in entrainment events in SFST flows. In the last chapter of the thesis, we consider air entrainment induced by two different near-surface vortex structures: a pair of counter-rotating vortex tubes and a ring-shaped vortex. The detailed interactions between the vortex structures and the free surface are studied in great detail. The dependencies of vortex-induced entrainment on relaxant controlling factors are carefully investigated as well. In particular, the dependencies of the entrainment volume on g and σ obtained in single vortex induced entrainment events are consistent with those obtained in SFST flows where

numerous entrainment events happen. In the numerical simulation of SFST using a two-fluid algorithm, a challenge problem remains due to the lack of a comprehensive modeling of sub-grid terms of air entrainment, which require averaged quantities in order to achieve closures. In the study of the vortex pair, we find a linear dependence of the entrainment volume on an averaged quantity of vertical vorticity flux. This linear dependence is general and always vali no matter how the initial vorticty field changes.

1.4.5 Thesis organization

This thesis is organized as follows: In Chapter 2, the numerical implementations of the DNS solver are presented. In Chapter 3, DNS of a SFST flow is performed to investigate the unique characteristics of SFST and SFST air entrainment. Chapter 4 is devoted to the derivation of a new parameterization model for bubble size spectrum of SFST entrainment. The DNS evidences and supports to the theoretical model are presented in Chapter 5. The study in Chapter 6 focuses on air entrainment induced by near-surface vortex structures. Summary and potential future works are described in Chapter 7.

1.5 Important notations used in this thesis

In this section, we first briefly summarize several important notations regarding the quantity of bubble size spectrum used in this thesis. In the models of Garrett *et al.* (2000) and Deane & Stokes (2002), the notation $N(r)$ is defined as the bubble size spectrum per unit volume. In this thesis, we specifically focus on air entrainment across a free surface induced by SFST and study the corresponding bubble size distribution. To quantify the entrainment bubble size distribution, we define $\mathcal{N}_a^E(r)$ as the bubble size spectrum per unit area of the initial flat free surface. To be noticed, the different normalization in the definition of $\mathcal{N}_a^E(r)$ and $N(r)$ do not change the scale dependence of interest, but only influences the magnitude. Here we use $\mathcal{N}_a^E(r)$ to represent the specific bubble size spectrum resulted by SFST driven entrainment

only. The actual bubble size spectrum in the bulk is also influenced by other physical processes such as fragmentation and degassing. In reality, $\mathcal{N}_a^E(r)$ is difficult to be directly measured. To obtain $\mathcal{N}_a^E(r)$, the bubble size spectrum in the bulk, $N_a(r)$, needs to be measured first before significant bubble fragmentation and degassing happen. Then $\mathcal{N}_a^E(r)$ can be obtained by normalizing $N_a(r)$ using the area of the initial flat free surface.

- $N(r)$: bubble size spectrum per unit volume used in the previous models by Garrett *et al.* (2000) and Deane & Stokes (2002).

- $\mathcal{N}_a^E(r)$: entrainment bubble size spectrum per unit area of the initial interface introduced in our new theoretical model.

- $N_a(r)$: bubble size spectrum measured by labeling and sizing entrained bubbles in the bulk from DNS results.

The study of bubble size spectrum also involves several length scales. First, there exist two regimes of $N(r)/\mathcal{N}_a^E(r)$ depending on the bubble radius r. We use the notation r_a to represent the transition scale of the two regimes. Previous, r_a is assumed to be the Hinze scale r_H. In this thesis, we prove that r_a is the capillary length scale r_c. Besides, we also introduce two length scales r_l and r_u to represent the lower and upper bound of the range of entrainment bubble size.

- r_a: transition scale of the two regimes of bubble size spectrum

- $r_c = 0.5\sqrt{\sigma/\rho g}$: capillary length scale at which Bond number $Bo = \frac{\rho g(2r_c)^2}{\sigma}$ is equal to 1.

- $r_H = 2^{-8/5}(\sigma/\rho We_c)^{3/5}\epsilon^{-2/5}$: Hinze scale at which (turbulence) Weber number $We_t = \rho\overline{v^2}(2r_H)/\sigma$ is equal to a critical value We_c. Experimental measurements suggest that We_c is in a range between 3 and 4.7 (MARTÍNEZ-BAZÁN *et al.*, 1999; Lewis, 1982). $\overline{v^2}$ is the turbulence fluctuation over a distance d. For isotropic homogenous turbulence, $\overline{v^2} \approx 2.0(\epsilon d)^{2/3}$.

- $r_l = 2^{-8/5}(\sigma/\rho We_l)^{3/5}\epsilon^{-2/5}$: lower bound of the bubble size range of SFST entrainment at which $We_t = \rho\overline{v^2}(2r_l)/\sigma = We_l \ll 1$

- $r_u = 4(Fr_u^2 g)^{-3}\epsilon^2$: upper bound of the bubble size range of SFST entrainment at which the (turbulence) Froude number $Fr_t^2 = \overline{v^2}/g(2r_u) = Fr_u^2 \ll 1$

Chapter 2

DNS solver for two-phase incompressible flows

In this chapter, the numerical algorithms implemented in the DNS solver for two-phase incompressible flows are introduced first. Then a bubble/cavity identification algorithm used for post-processing is introduced. In the final part of this chapter, the DNS solver is applied to perform a numerical simulation of a small amplitude standing wave driven by surface tension on the interface between two viscous fluids. The numerical results are compared with the theoretical solution for the purpose of solver verification.

2.1 Numerical implementations of DNS solver

In this thesis, high-resolution DNS is performed by solving the three-dimensional two-phase incompressible Navier-Stokes equations with a fully nonlinear interface. We assume atmospheric conditions and do not consider the solubility of air (and other chemical reactions). The three-dimensional two-phase incompressible Navier-Stokes

equations in a single-fluid form with variable density ρ and viscosity μ are:

$$\begin{aligned} \frac{\partial \mathbf{u}}{\partial t} + \nabla \cdot (\mathbf{uu}) &= -\frac{1}{\rho}\nabla p + \frac{1}{\rho Re}\nabla \cdot \mu(\nabla \mathbf{u} + \nabla \mathbf{u}^T) + \frac{\mathbf{e}_z}{Fr^2} + \frac{1}{We}\kappa \delta_s \mathbf{n} \\ \nabla \cdot \mathbf{u} &= 0 \\ \frac{\partial f}{\partial t} + \mathbf{u} \cdot \nabla f &= 0\,, \end{aligned} \tag{2.1}$$

where $f(\mathbf{x}, t)$ represents the volume fraction implemented by the conservative volume-of-fluid method (cVOF) (Weymouth & Yue, 2010). In (2.1), the density and viscosity are defined as $\rho(f) = f + (1-f)\rho_2/\rho_1$, $\mu(f) = f + (1-f)\mu_2/\mu_1$, where ρ_1, ρ_2 and μ_1, μ_2 denote the density and viscosity of the two fluids respectively and $\mathbf{e}_z$ denotes a unit vector in vertical direction, δ_s is the interfacial Dirac delta function, κ is the interface curvature, and $\mathbf{n}$ is the normal vector to the interface. The equation is non-dimensionalized by characteristic velocity scale U and length scale L and the water density ρ_1 and viscosity μ_1 such that the relevant parameters of the problem are Reynolds number $Re = \rho_1 UL/\mu_1$, Froude number $Fr = U/\sqrt{gL}$, and Weber number $We = \rho_1 U^2 L/\sigma$ (using the surface tension coefficient σ).

The numerical implementation of (2.1) is a second-order (in space and time) finite volume scheme, with sharp interface, utilizing a staggered grid. Time integration is a two-stage Runge-Kutta method. A projection method is used to conserve mass and solve for the pressure. The resulting variable coefficient Poisson equation is solved using the HYPRE library (Falgout *et al.*, 2006; Falgout & Yang, 2002). Finally, surface tension effects are implemented through the continuous surface force (CSF) method (Brackbill *et al.*, 1992) along with a height-function method for the interface curvature calculation described in Popinet (2009); Cummins *et al.* (2005).

2.1.1 Finite volume method

To discretize the momentum equations, we use the finite volume algorithm, where the conservative principles of mass and momentum are applied to a small control volume. We simply integrate each term in (2.1) over the computational cell. The velocity at

the center of the cell:

$$\boldsymbol{u}_c = \frac{1}{V}\int_V \boldsymbol{u}(\boldsymbol{x})dv \tag{2.2}$$

where V is the volume of the computational cell. For the advection term $\boldsymbol{A} = \nabla\cdot(\boldsymbol{uu})$, the average value over a computational cell is defined as:

$$\boldsymbol{A}_c = \frac{1}{V}\int_V \nabla\cdot(\boldsymbol{uu})dv = \frac{1}{V}\oint_S \boldsymbol{u}(\boldsymbol{u}\cdot\boldsymbol{n})ds \tag{2.3}$$

Here we use the divergence theorem to rewrite the volume integral as a surface integral over the boundary S of the computational cell. For the diffusion term $\boldsymbol{D} = \nabla\cdot\mu(\nabla\boldsymbol{u}+\nabla u^T)$, the corresponding average value is given by:

$$\boldsymbol{D}_c = \frac{1}{V}\int_V \nabla\cdot\boldsymbol{T}^V dv = \frac{1}{V}\oint_S \boldsymbol{n}\cdot\boldsymbol{T}^V ds \tag{2.4}$$

where $\boldsymbol{T}^V = \mu\left[\nabla_h\boldsymbol{u} + (\nabla_h\boldsymbol{u})^T\right]$ is the viscous stress tensor for incompressible flow. The subscript h stands for numerical approximations. The average value of the pressure gradient is:

$$(\nabla p)_c = \frac{1}{V}\int_V \nabla p dv = \frac{1}{V}\oint_S p\,\boldsymbol{n}\,ds \tag{2.5}$$

For the surface tension force, the CSF method approximates the surface tension term $\kappa\delta_s\mathbf{n}$ in (2.1) as $\kappa\nabla f$. Together with the gravity force, we can combine the two forces together as a body force $\boldsymbol{F}_b = \frac{\mathbf{e}_z}{Fr^2} + \frac{1}{We}\kappa\nabla f$ has the average value:

$$\boldsymbol{F}_c = \frac{1}{V}\int_V \boldsymbol{F}\,dv \tag{2.6}$$

The continuity equation in (2.1) is approximated in the integral form by evaluating:

$$\oint_S \boldsymbol{u}\cdot\boldsymbol{n}\,ds = 0 \tag{2.7}$$

The integrals above allows us to rewrite (2.1) in the integral form and apply discrete approximations on a staggered grid. We use centered differencing for all spatial variables and the detailed expressions of the discretization can be found in chapter 3

of Tryggvason *et al.* (2011).

2.1.2 Pressure projection method

The pressure field is solved by using a projection method to force the divergence of the velocity field to be zero. Given the velocity field at the current time step $\boldsymbol{u}^{(k)}$, the pressure filed p is described by a discrete Poisson equation:

$$\nabla_h \cdot \left(\frac{1}{\rho^{(k)}} \nabla_h p \right) = \nabla_h \cdot \left(\frac{\boldsymbol{u}^{(k)}}{\Delta t} - \boldsymbol{A}_h^{(k)} + \frac{1}{\rho^{(k)}} \left(\boldsymbol{D}_h^{(k)} + \boldsymbol{F}_h^{(k)} \right) \right) \tag{2.8}$$

2.1.3 Runge-Kutta method for time integration

A second-order Runge-Kutta method is used for the time integration and the advection of volume fraction. Given $\boldsymbol{u}^{(k)}$, we first obtain the pressure field $p^{(k+\frac{1}{2})}$ by solving (2.8). $p^{k+\frac{1}{2}}$ is used to project the velocity onto a divergence free velocity field by:

$$\boldsymbol{u}^{(k+\frac{1}{2})} = \boldsymbol{u}^{(k)} + \Delta t \left(-\boldsymbol{A}_h^{(k)} + \frac{1}{\rho^{(k)}} \left(\boldsymbol{D}_h^{(k)} + \boldsymbol{F}_h^{(k)} \right) - \frac{1}{\rho^{(k)}} \nabla_h p^{(k+\frac{1}{2})} \right) \tag{2.9}$$

The volume fraction is updated through a forward Euler step:

$$f^{(k+\frac{1}{2})} = f^{(k)} + cVOF\left(\boldsymbol{u}^{(k)}, f^{(k)}, \Delta t \right) \tag{2.10}$$

For brevity, the procedures to update the volume fraction including the reconstruction and advection algorithms of cVOF are denoted by $cVOF$. The complete description of cVOF can be found in Weymouth & Yue (2010). The above processes are repeated for the second step of the Runge-Kutta method. The Poisson equation of the pressure field is in the form:

$$\nabla_h \cdot \left(\frac{1}{\rho^{(k+\frac{1}{2})}} \nabla_h p^{(k+1)} \right) = \nabla_h \cdot \left(\frac{\boldsymbol{u}^{(k)} + \boldsymbol{u}^{(k+\frac{1}{2})}}{\Delta t} - \boldsymbol{A}_h^{(k+\frac{1}{2})} + \frac{\boldsymbol{D}_h^{(k+\frac{1}{2})} + \boldsymbol{F}_h^{(k+\frac{1}{2})}}{\rho^{(k+\frac{1}{2})}} \right) \tag{2.11}$$

With $p^{(k+1)}$, the velocity field next step $\boldsymbol{u}^{(k+1)}$ is obtained by:

$$\boldsymbol{u}^{(k+1)} = \frac{\boldsymbol{u}^{(k)} + \boldsymbol{u}^{(k+\frac{1}{2})}}{2} + \frac{\Delta t}{2}\left(-\boldsymbol{A}_h^{(k+\frac{1}{2})} + \frac{\boldsymbol{D}_h^{(k+\frac{1}{2})} + \boldsymbol{F}_h^{(k+\frac{1}{2})}}{\rho^{(k+\frac{1}{2})}} - \frac{\nabla_h p^{(k+1)}}{\rho^{(k+\frac{1}{2})}}\right) \tag{2.12}$$

The volume fraction next step is updated by:

$$f^{(k+1)} = f^{(k)} + cVOF\left(\frac{\boldsymbol{u}^{(k)}+\boldsymbol{u}^{(k+\frac{1}{2})}}{2}, f^{(k)}, \Delta t\right) \tag{2.13}$$

2.1.4 Height function for surface curvature calculation

To calculate the surface curvature κ, the hight function algorithm in Popinet (2009); Cummins *et al.* (2005) is applied. This algorithm can be summarized into three main steps.

- Consider a 3×7 stencil centered on the target cell where the curvature needs to be evaluated.

- Estimate the interface orientation and find the direction of the maximal normal direction to orient the height function.

- Build a discrete approximation of the interface height by summing the volume fractions in each volume along the maximum normal direction.

- Use finite difference approximation to compute the curvature.

As an two-dimensional example shown in figure 2-1(a), say the maximum normal direction of the interface is $y-$ direction. We use $\boldsymbol{n} = (n_x, n_y)$ to represent the normal direction of the interface. In the example, $|n_y| > |n_x|$. Then the discrete interface height can be estimated by:

$$Y_{ij} = \sum_{j-3}^{j+3} f_{ij} \tag{2.14}$$

The the curvature of the 2D interface at cell (i, j) can be determined by:

$$\kappa = sign(n_y)\frac{Y_{xx}}{(1+Y_x^2)^{3/2}} \tag{2.15}$$

where Y_x and Y_{xx} are estimated with central differences. For a 3D space interface with normal direction $\boldsymbol{n} = (n_x, n_y, n_z)$, assume the maximum normal direction is $y-$ direction. Then the corresponding curvature can be obtained by:

$$\kappa = sign(n_y)\frac{Y_{xx} + Y_{zz} + Y_{xx}Y_z^2 + Y_{zz}Y_x^2 - 2Y_{xz}Y_xY_z}{(1+Y_x^2+Y_z^2)^{3/2}} \tag{2.16}$$

Figure 2-1(b) shows an example that the height function does not lie within the cell (i, j), in which case the described algorithm above may introduces larger errors. Advanced techniques are required in the future to address this issue and improves the precision of interface curvature calculation. For a typical sphere, the current algorithm needs 3 or 4 grid cells to resolve the sphere radius in order to obtain reasonable curvature. With less than 3 grid cells for the radius resolution, the numerical errors of the computed curvature become comparable to the true value.

2.2 Post-processing bubble/cavity identification algorithm

A bubble/cavity identification algorithm based on the union-find algorithm (Cormen *et al.*, 2009) is developed to identify entrained air bubbles from the information of f in the computational domain. In this scheme, instantaneous air entrainment is defined as the void fraction not connected to the air domain. The total entrainment volume V is the sum of the air entrainment void fraction identified. Individual air bubbles are disjoint subsets of the entrained void fraction. The union-find algorithm has been widely used for disjoint-set data structures and takes O(n) time in the worst case. Figure 2-2 shows examples of different sets of void fraction in the water domain. For the void fraction set number 1, the bubble/cavity identification algorithm detects

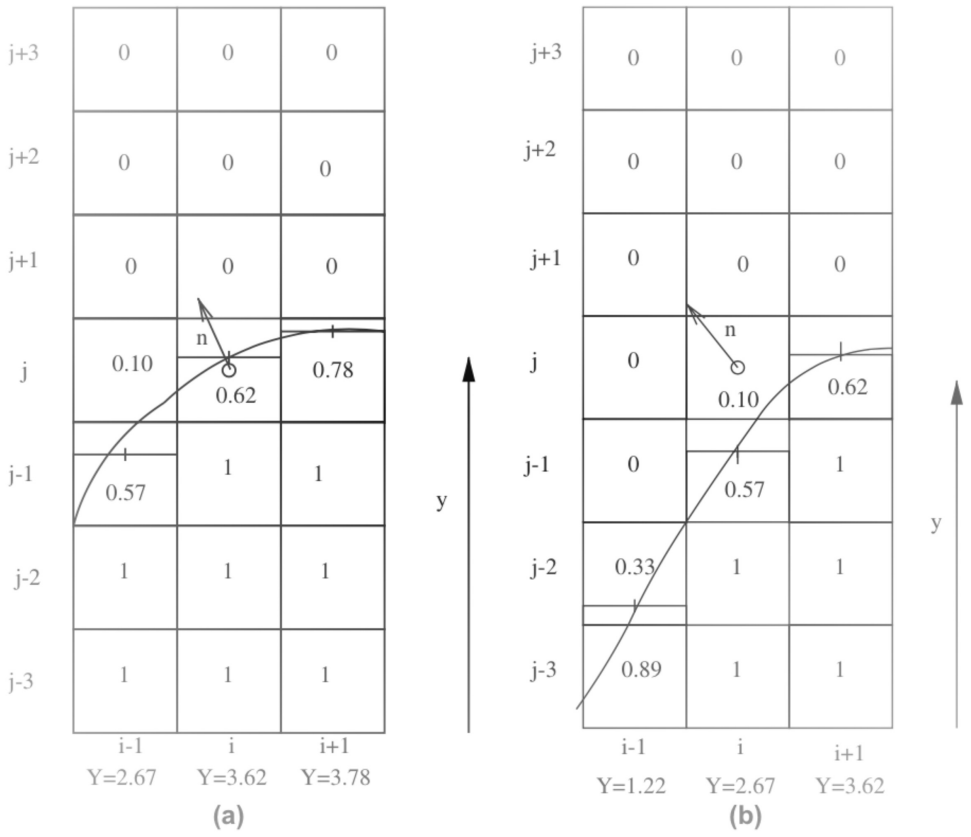

Figure 2-1: Examples of the height function method for 2D problem (Cummins *et al.*, 2005). (a) the hight function lies within cell (i, j); (b) where the height function does not lie within cell (i, j).

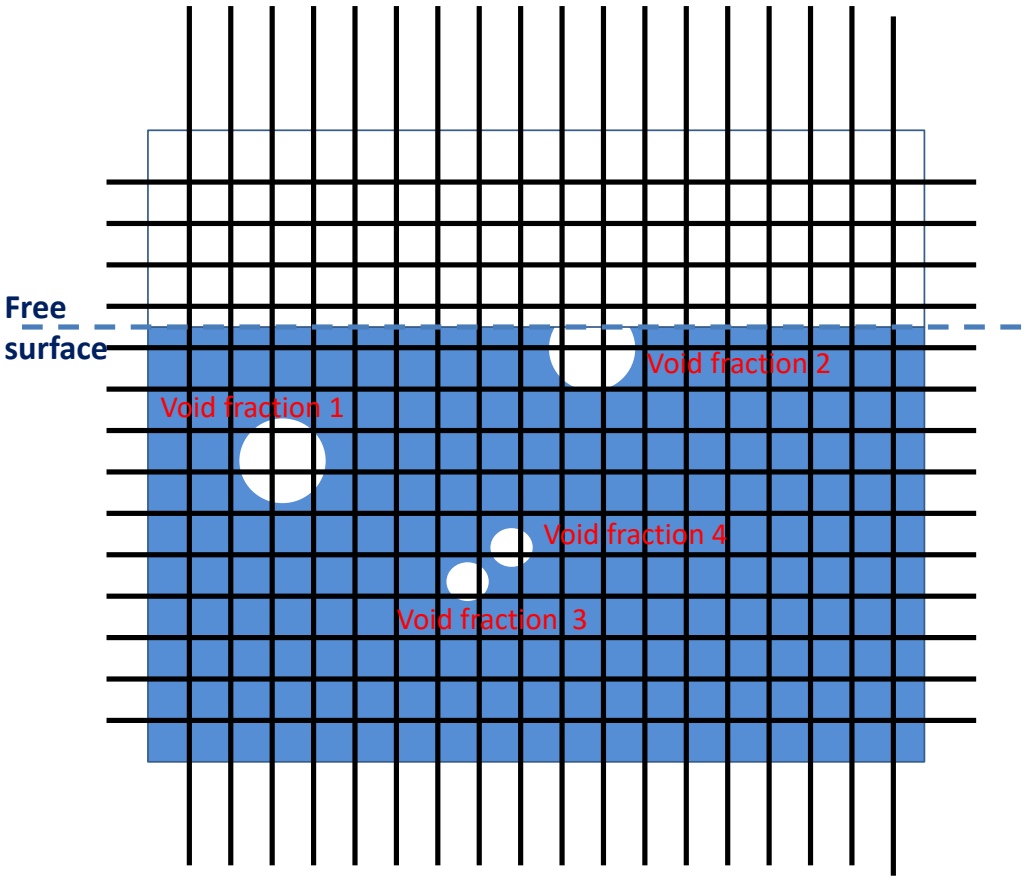

Figure 2-2: Examples of void fraction sets in the water domain.

it as an individual entrained bubble since the computational cells that contain void fraction are joint with each other and not connected to the air domain. The void fraction set number 2, however, cannot be identified as an entrained bubble because the cells with void fraction are connected to the air domain. For the void fraction set number 3 and 4, the identification algorithm considers them together as a single entrained bubble instead of two, due to the limitation of the numerical resolution. Instead of two disjoint sets, the cells of the two sets that contain void fraction are connected and become a joint set. Thus, the current algorithm detects the two void fraction sets as a single bubble.

For the problem we consider, the total void fraction is small ($\lesssim 1\%$), and a precise quantification of entrained volume is essential. To this end, the cVOF we use is shown to conserve volume to machine accuracy (Weymouth & Yue, 2010). With the cavity

identification algorithm, the bubble size spectrum of the entrained bubbles in the computational domain can be calculated in terms of the equivalent spherical radius r for the given volumes.

2.3 Solver Verification

Extensive verification and validation of the solver are documented in Campbell (2015). The three-dimensional Navier Stokes solver accurately predicts turbulent wall boundary layer flows (see figure 6-1 in Campbell, 2015). The cVOF method conserves volume to machine accuracy and is second-order accurate (Weymouth & Yue, 2010). Here the solve is applied to perform a DNS of a small amplitude standing wave driven by surface tension on the interface between two viscous fluids. The solution of an interfacial standing wave has the form $h(x,t) = a(t)cos(kx)$. Here, we consider two fluids of the same constitutive properties ($\rho_1/\rho_2 = 1$ and μ_1/μ_2=1) and Re=1280 and We=550. The domain is a unit cube with periodic boundary conditions in the horizontal directions and no-flux boundary conditions in the vertical direction. The simulation results are compared with the analytical theory of Prosperetti (1981). Figure 2-3(a) compares the wave amplitude $a(t)$ of numerical simulations with the theoretical solution. Figure 2-3(b) shows the L^2 norm of the numerical error as a function of grid size Δ confirming the expected second-order convergence.

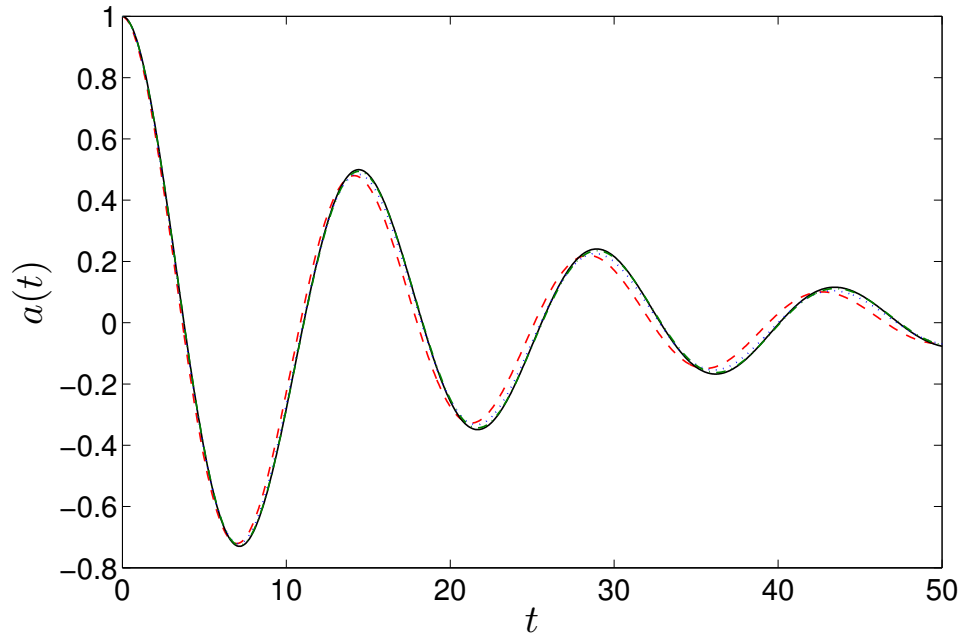

(a)

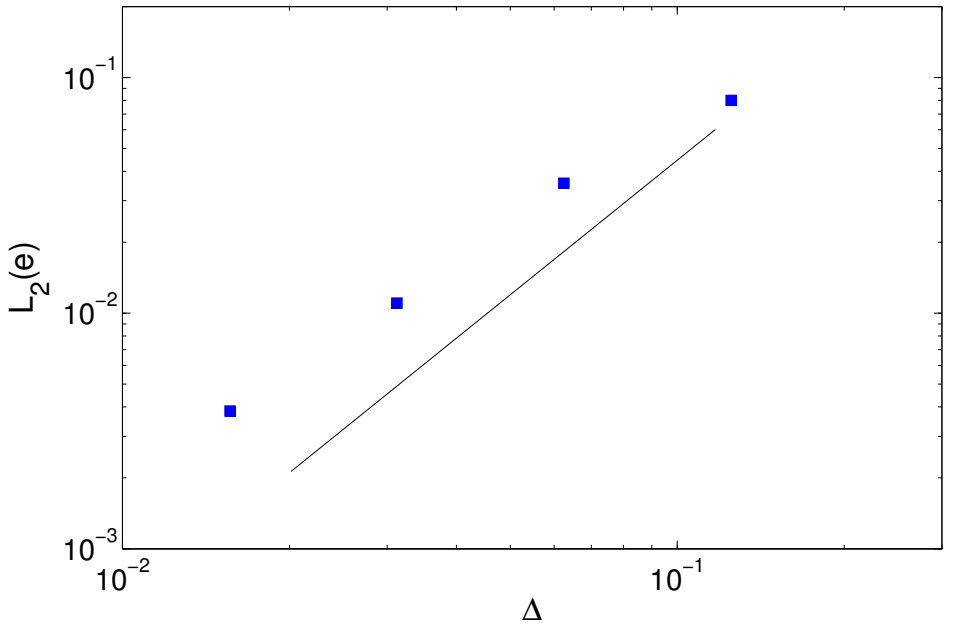

(b)

Figure 2-3: (a) Time evolution of wave amplitude $a(t)$ at the interface of two superposed viscous fluids. ——, theoretical solution (Prosperetti, 1981); - - -, numerical result with 32^3 grids; · · ·, with 64^3 grids; — · —, with 128^3 grids; (b) Error of the numerical result compared to the theoretical solution as a function of grid size. — second-order convergence.

Chapter 3

Strong free-surface turbulence and air entrainment

In this chapter, we consider a canonical problem of a three-dimensional incompressible two-phase (air and water) viscous turbulent flow with turbulent kinetic energy supplied by a sheared underlying bulk water flow. The main research targets are to: (i) elucidate the characteristics of turbulence in SFST compared to that in WFST; (ii) obtain the size distribution of the entrained bubbles and its evolution as the entrainment process continues. We perform DNS at different Fr to show the characteristics of near-surface turbulence in SFST. We find that for sufficiently large Fr, the blockage layer and surface layer observed in WFST disappear, with the SFST obtaining near surface isotropy and energy spectrum following the $k^{-5/3}$ power-law. The free surface exhibits large deformations due to the strong underlying turbulence. We also characterize the size distributions of the entrained bubbles. We find that bubble size spectrum follows a power-law size spectrum $N_a(r) \propto r^{-10/3}$ in the early phase of the entrainment process. This scaling law is obtained using a simple energy argument. With continuing air entrainment and ongoing turbulence fragmentation of the (already) entrained bubbles, the bubble size spectrum starts to evolve with time and deviate from the initial power-law. To provide some qualitative insight into this evolution, we suggest a heuristic model which combines the two main mechanisms of ongoing SFST entrainment and subsequent fragmentation cascades of these bubbles.

3.1 DNS configurations

3.1.1 Problem definition

Figure 3-1 shows a definition sketch. The initial shear flow has a mean velocity profile $U(z, t = 0)$ in the x-direction given by Mattingly & Criminale (1972):

$$U(z/L, t = 0) = 1 - 0.9988 sech^2(0.88137 z/L). \tag{3.1}$$

This canonical shear-flow free-surface turbulence problem with the initial profile (3.1) has been used in a number of previous studies of weak free-surface turbulence e.g. Shen *et al.* (1999, 2000, 2001); Shen & Yue (2001). For the problem in figure 3-1, we choose the initial mean shear flow depth L as the characteristic length scale and the velocity deficit U as the velocity scale. Hereafter, all the variables are normalized by U and L unless otherwise stated. The domain size is $10.472 \times 10.472 \times 6$. The initial flat free surface is at $z = 0$. The water domain is $z \in [-4, 0]$ and the air domain is $z \in [0, 2]$. The boundary conditions are periodic boundary in the horizontal x-y plane and no-flux at the top and bottom of the domain. As in Shen *et al.* (1999), the simulations are initialized using (3.1) with small (isotropic) turbulence seed of magnitude of 0.08. The direct numerical simulations are continued through $T = Ut/L = 160$ (during which time the FST develops, reaches a quasi-steady phase, and has begun to decay). Our main focus in this work are the effects of Fr and We on FST characteristics, the associated surface deformation and resulting air entrainment. We perform simulations for a broad range of Fr and We to elucidate and quantify these effects. For sufficiently large Re, the effects on the mechanisms above are less direct, and are not expected to change for moderate variations of Re (amendable to DNS). In this study, we fix $Re = 1000$ which provides turbulence with a sufficient inertial range (see figure 3-14 for example). Higher Re shows affects mainly in the smaller-scale turbulence structures, resulting in a wider inertia range, but has limited direct effect on the large-scale FST and air entrainment mechanisms.

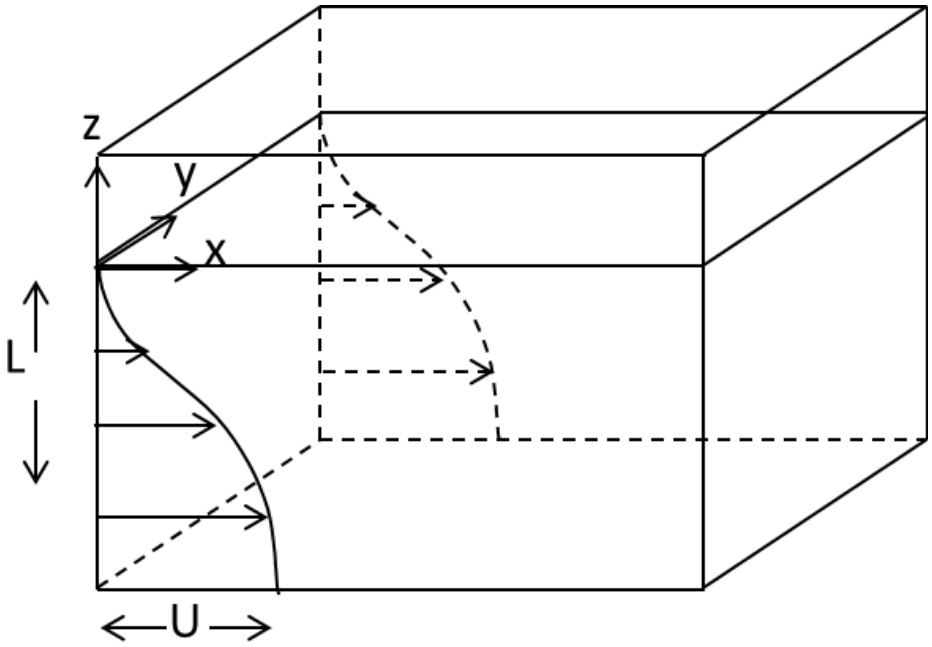

Figure 3-1: Definition sketch showing a free surface present at $z = 0$ separating a stationary gas and a turbulent liquid with a sheared flow $U(z)$, where U is the deficit velocity and L is the flow depth.

3.1.2 Convergence study

To establish that our numerical resolution is sufficient for DNS of the problem, we consider a SFST case ($Fr^2 = 10$ and $We = \infty$) on three different grids $256^2 \times 192$, $384^2 \times 256$, and $512^2 \times 384$ with the corresponding grid size Δ_{256}, Δ_{384}, $\Delta_{512} \approx 0.041$, 0.027, 0.020. Figure 3-2 shows the convergence trend and general agreement of the evolution for the mean velocity profile $\langle u(z) \rangle$, where $\langle \cdot \rangle$ denotes average in the horizontal plane, obtained using these three grids. We estimate the Kolmogorov scale based on the estimated turbulence dissipation rate $\epsilon \sim O(5 \times 10^{-4})$ (see figures 5-4(b) and 5-8(b)). Using this value of ϵ assuming isotropic homogeneous turbulence, the Kolmogorov scale $\eta \sim \epsilon^{-1/4} Re^{-3/4} \approx 0.04$. Thus the medium resolution grid with $\Delta_{384} \approx 0.027$ is sufficient to resolve the turbulence. Figure 3-3 shows the instantaneous bubble size spectrum $N_a(r)$ in the SFST with three resolutions of Δ_{256}, Δ_{384} and Δ_{512} at different times. The shape of $N_a(r)$ and its evolution trend with time are consistent using the three resolutions, suggesting that the statistics of bubble size

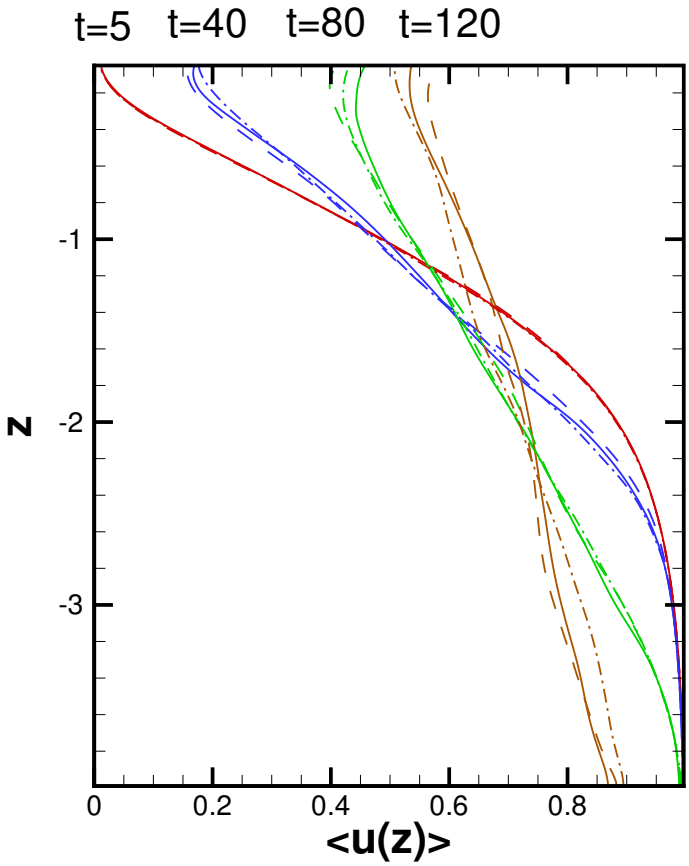

Figure 3-2: Mean velocity profile $\langle u(z) \rangle$ as a function of z at different times with $Fr^2 = 10$ and $We = \infty$. ——, Δ_{512}; - - -, Δ_{384}; — · —, Δ_{256}.

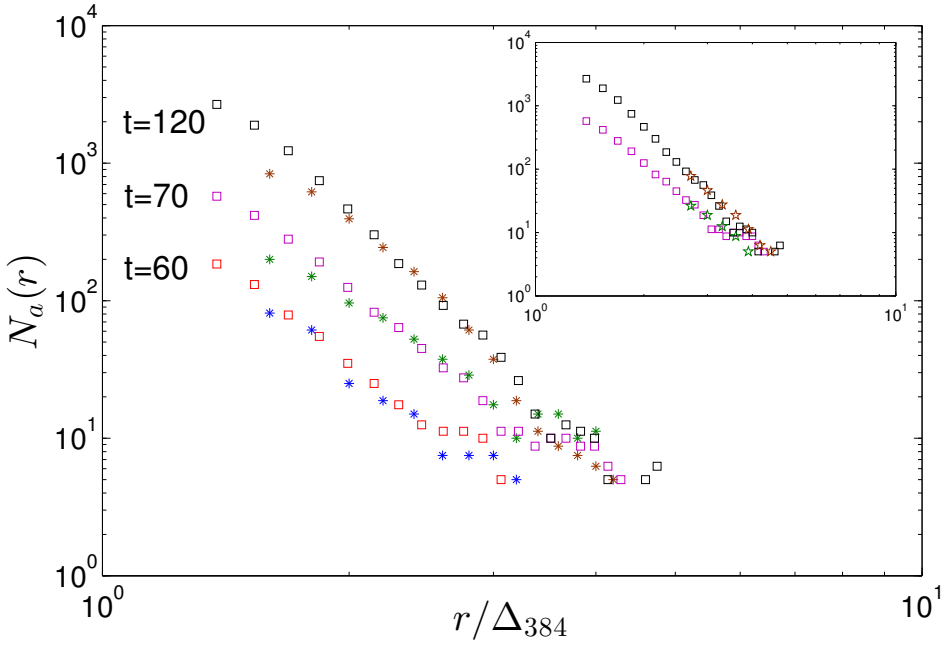

Figure 3-3: Bubble size spectrum $N_a(r)$ as a function of normalized bubble radius r/Δ_{384} at different times of $Fr^2 = 10$ and $We = \infty$. □, Δ_{512}; ∗, Δ_{384}

are converged in spite of the variation in grid size. For Δ_{256}, the resolved range is relatively limited, and the results are included in an inset in figure 3-3. The entrained volume is the integral under the spectra and show similar convergence. For all the later numerical results we present, we use $\Delta = \Delta_{384}$.

The size range of resolved bubbles depends on Δ, as expected from the cVOF method. The cVOF conserves bubble volume to machine accuracy but resolves bubble sizes only to Δ. Here, the smallest bubble being considered to be resolved is of radius of 1.5Δ. Bubbles smaller than this are not presented in our bubble size spectra. Δ is also defined as the numerical Hinze scale. The void fraction of bubbles smaller than this scale is $< 1\%$ of the total entrainment volume for all cases/time. Thus the entrainment rate results we report are not affected by the numerical Hinze scale.

Physically, these is a length scale $\ell_\sigma \sim O(1)mm$. Surface tension is important for bubbles of radius smaller than this scale and affects the bubble size spectrum accordingly (see e.g. the experimental measurements by Deane & Stokes (2002)). Because of computational limitations of DNS, the maximum grid resolution we use

is $L/\Delta \approx 50$ and we are not able to resolve ℓ_σ for the case of $We = \infty$. However, we point out that the presented bubble size spectra of this case are not affected by resolution of ℓ_σ. For a given ($L-$based) Fr, ℓ_σ/Δ decreases as We increases. When $We \to \infty$, $\ell_\sigma/\Delta \ll 1$. Bubbles of size below Δ are not resolved, and are always excluded in the DNS bubble size spectrum. The bubbles that are included in the size spectrum are of size $\gg \ell_\sigma$ in the case of $We = \infty$, indicating negligible surface tension effects on these bubbles.

In figure 3-3, r is scaled by Δ since, for $We = \infty$, physical scales associated with surface tension become $\ll \Delta$ and are not useful for normalization. Instead we choose Δ as a length scale to normalize r to show the resolution used to resolve the bubbles in $N_a(r)$.

For this SFST case, we perform an ensemble of simulations to obtain the statistical quantities of interest. Appendix A shows the validity of the obtained statistics through both an ensemble study and a statistical analysis. The maximum statistical error of the mean for all cases is less than 4%.

3.2 Characteristics of FST at large Fr and We

To understand quantitative differences in the turbulence characteristics between SFST and WFST, we consider a WFST case of $Fr^2 = 0.5$, $We = \infty$ (Shen *et al.*, 1999) and a SFST case of $Fr^2 = 10$, $We = \infty$. The DNS is robust for $We \to \infty$ as well as $We = \infty$. We use the latter to represent case(s) where surface tension effects are negligible compared to gravity and flow inertia.

3.2.1 Definition of the near surface region

To quantify near-surface turbulent quantities, we define the near surface region as a thin layer of thickness δ below the free surface. We further define a turbulence quantity $q(\mathbf{x}, t)$ near the free surface as a volume fraction weighted average $\langle q(t) \rangle_\delta$

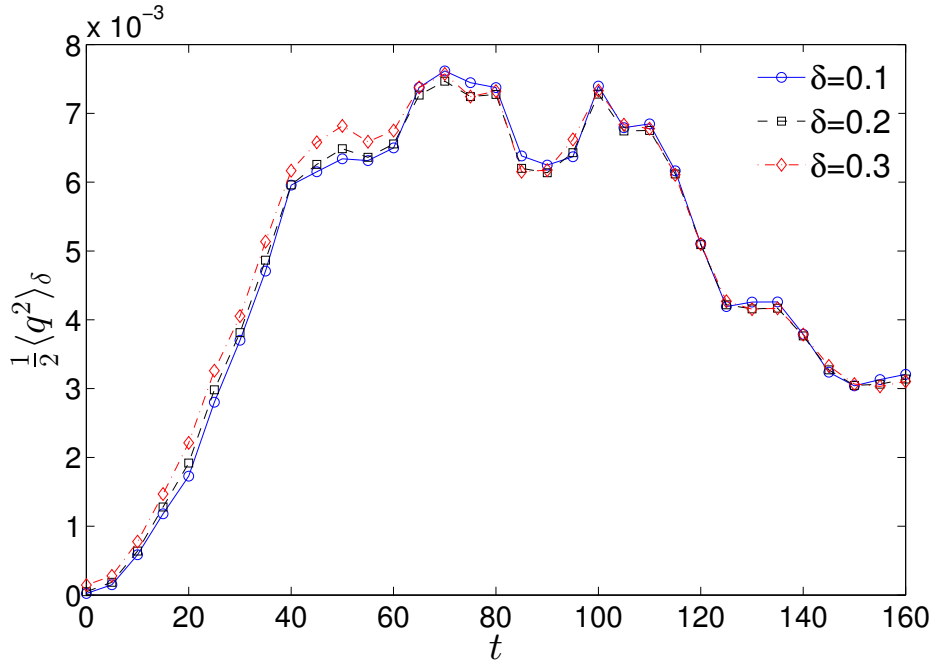

Figure 3-4: Time evolution of turbulent kinetic energy near the free surface $\frac{1}{2}\langle q^2\rangle_\delta$ using different values of δ of the flow $Fr^2 = 10$ and $We = \infty$. - -○- - δ=0.1; - -□- -δ=0.2; and - -◇- - δ=0.3.

over the whole layer:

$$\langle q(t)\rangle_\delta = \frac{\int_x \int_y \int_z f(\mathbf{x},t) q(\mathbf{x},t) d\mathbf{x}}{\int_x \int_y \int_z f(\mathbf{x},t) d\mathbf{x}} \text{ for } z \geq -\delta. \tag{3.2}$$

where f is the volume fraction. The choice of δ should be such to capture the effects of the free surface on the underlying turbulence. For WFST, the blockage layer thickness is $O(0.5)$ and the turbulence in this layer exhibits distinctly different characteristics than the bulk flow. Thus, $\delta \leq 0.5$ could be considered to be representative of "turbulence near the free surface". Figure 3-4 shows the insensitivity of the turbulent kinetic energy in the near surface region to different δ. Thus, we choose $\delta = 0.2$ to represent the thickness of the near free surface region and $\langle\cdot\rangle_\delta$ represents an volume fraction averaged quantity over the near free surface region unless otherwise stated.

3.2.2 Overview of SFST

Figure 3-5 shows the time evolution of turbulent kinetic energy near the free surface (TKE) $\frac{1}{2}\langle q^2\rangle_\delta$ of the two flows, where $q^2 = u'^2 + v'^2 + w'^2$ and $\langle\cdot\rangle_\delta$ is defined as the average over the "near free surface" region. u', v' and w' are velocity fluctuations in x, y and z direction. The detailed definition and sensitivity analysis to the parameter δ are in section 3.2.1. The evolution of TKE shows three somewhat distinct stages for both WFST and SFST. In the initial growth stage, TKE increases due to production by the mean shear flow. This is followed by a quasi-steady stage where production is approximately balanced by turbulent dissipation ϵ (Shen *et al.*, 1999). This same flow has been studied extensively for WFST (Shen *et al.*, 1999, 2000, 2001). In particular, Shen *et al.* (1999) showed the same TKE plateau, and provide term-by-term analyses of the turbulent kinetic energy budget. We have performed the same analysis for the present study, detailed results omitted for brevity. At later times, as the strength of the mean shear decreases (cf. figure 3-2), TKE decays with ϵ. The mechanism for the plateau in TKE during the quasi-steady period differs from that of homogeneous shear flow where the velocity profile is maintained and the TKE reaches a non-physical plateau limited by the domain (or box) size (Rogers & Moin, 1987). To confirm that the plateau in TKE is not due to domain size limitations, we estimate the longitudinal integral scale L_T in the quasi-steady stage of the SFST case using (Pope, 2001):

$$L_T = \int_0^\infty f(r,t)dr \tag{3.3}$$

where $f(r,t) = \langle u(\mathbf{x}+r\mathbf{e_x},t)u(\mathbf{x},t)\rangle/\langle u^2\rangle$ and $\mathbf{e_x}$ is the unit vector in x direction. At $t = 90$, $L_T \approx$2.5, which is a quarter of the horizontal computational box size.

The magnitude of TKE are similar in WFST and SFST (figure 5-4(a)). In WFST, the strong blockage effect of the near flat free surface constrains the vertical component of the velocity fluctuations. Meantime, due to the existence of the flat free surface, the inter-component transfer of turbulence energy among three components results in the enhancement the horizontal components Shen *et al.* (1999). Thus, the overall turbulent kinetic energy near the free surface in WFST is comparable to SFST

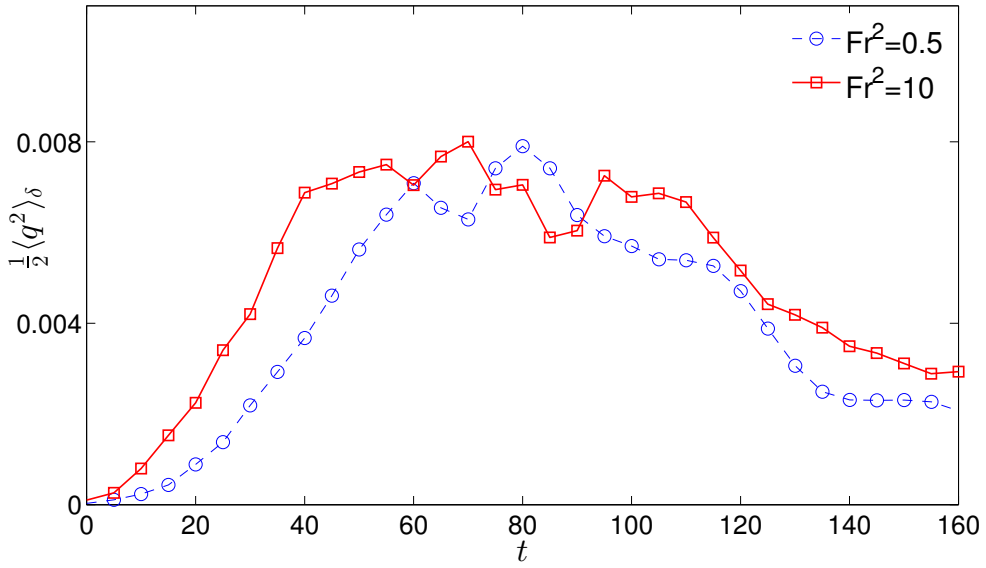

Figure 3-5: Time evolution of turbulent kinetic energy near the free surface $\frac{1}{2}\langle q^2\rangle_\delta$ of the flow for SFST $Fr^2 = 10$, $We = \infty$ (- -□- -) and WFST $Fr^2 = 0.5$, $We = \infty$ (- -o- -).

wherein the turbulence is almost isotropic (see figure 3-9 (b)). The consequence is that, despite the notable difference in the surface deformation and air entrainment, the qualitative effect of Fr on the available near-surface TKE is minimized (see 5-4(a)). A similar conclusion is drawn for We (see 5-8(a)). This is helpful in understanding the dependence of air entrainment on Fr and We, and is discussed in detail in §5.1 and 5.2.

Figure 3-6 shows a series of images of the free surface represented by the 0.5 volume fraction ($f = 0.5$) iso-surface of the case SFST. During the growth stage ($t = 20$), the free surface is slightly deformed and this continues as turbulence further develops ($t = 45$), inducing large surface elevations and small-scale surface deformations. Within the quasi-steady stage (e.g. $t = 60$ and $t = 85$), turbulence becomes strong enough that the surface cannot maintain its cohesion, resulting in substantial air entrainment. During the decay stage ($t = 125$ and $t = 150$), the free surface becomes coherent with less distortion. We note that even after near-surface turbulence has significantly decayed, it takes long time for the surface to become completely flat. Savelsberg &

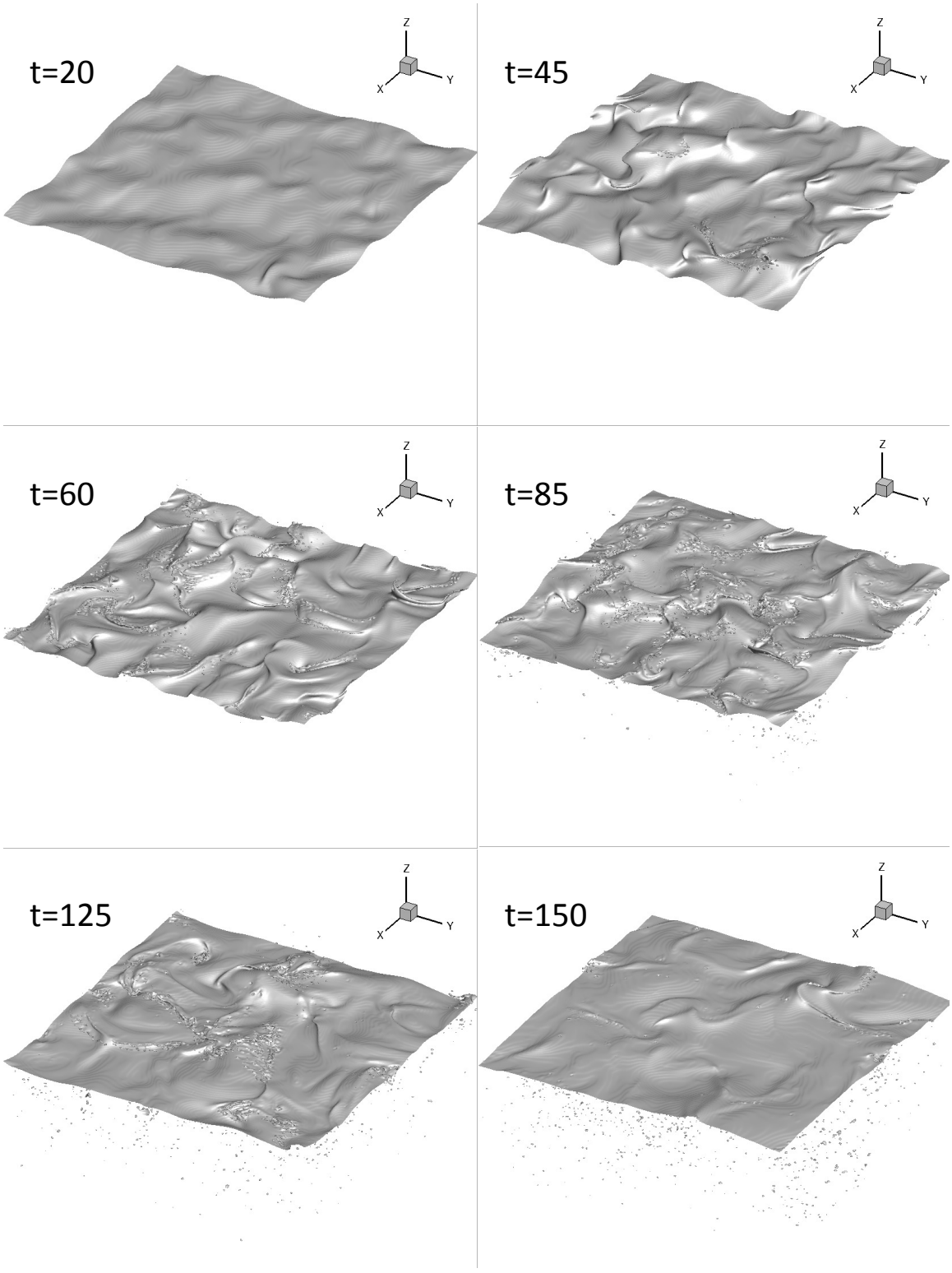

Figure 3-6: Evolution of the iso-surface of volume fraction $f = 0.5$ for SFST with $Fr^2 = 10$ and $We = \infty$.

van de Water (2008, 2009); Guo & Shen (2010) showed that the surface deformation caused by turbulence propagates in the form of surface wave, which persists for a long time. A further investigation of this is beyond the scope of this study.

Figures 6-8(a) and 6-37(c) show respectively the time evolution of averaged surface elevation $\langle \eta^2 \rangle^{1/2}$ and surface curvature $\langle \kappa^2 \rangle^{1/2}$. Together with the evolution of $\frac{1}{2}\langle q^2 \rangle_\delta$ shown in figure 3-5, we observe that large surface deformation accompanies strong turbulence near the free surface. It confirms the disrupting effect of turbulence on the free surface. $\langle \eta^2 \rangle^{1/2}$ and $\langle \kappa^2 \rangle^{1/2}$ for WFST are three orders of magnitude smaller than those shown in figure 3-7 and thus not shown. In the WFST case, the stabilizing effect of gravity on the free surface is much stronger than the disruptive effect of the turbulence and thus the surface remains nearly flat by comparison.

3.2.3 Isotropy of SFST

Figure 3-8 shows the vertical profiles of u'^{rms}, v'^{rms} and w'^{rms} in WFST flow. Consistent with Shen *et al.* (1999), an outer blockage layer of thickness $O(0.5)$ is observed. In the blockage layer, w'^{rms} decreases sharply approaching the free surface and becomes near zero at the free surface z=0. Figure 3-9 shows the profiles of u'^{rms}, v'^{rms} and w'^{rms}s of SFST at two time instances. In contrast to the WFST case, there is no sharp decrease of w'^{rms} approaching the free surface, suggesting that the surface blockage effect is significantly reduced and the blockage layer disappears. In the growth stage ($t = 20$), w'^{rms} is larger than u'^{rms}, v'^{rms} at $z = 0$ (see figure 3-9a). This is due to the horizontal velocity components being constrained by the inertia of the surrounding liquid (Brocchini & Peregrine, 2001*a*) in the early stage. In the quasi-steady stage ($t = 90$), all three components are of comparable magnitude at the free surface (see figure 3-9b). Note here that in this stage, u'^{rms} and v'^{rms} near the free surface in SFST are smaller than those in WFST. This is because these components are enhanced due to energy transfer in the blockage layer of WFST.

The vorticity fluctuations also show significant differences in SFST compared to WSFT as shown in figure 3-10. In particular, the presence of the surface layer in WFST is dramatically reduced in SFST. This is seen in the horizontal vorticity com-

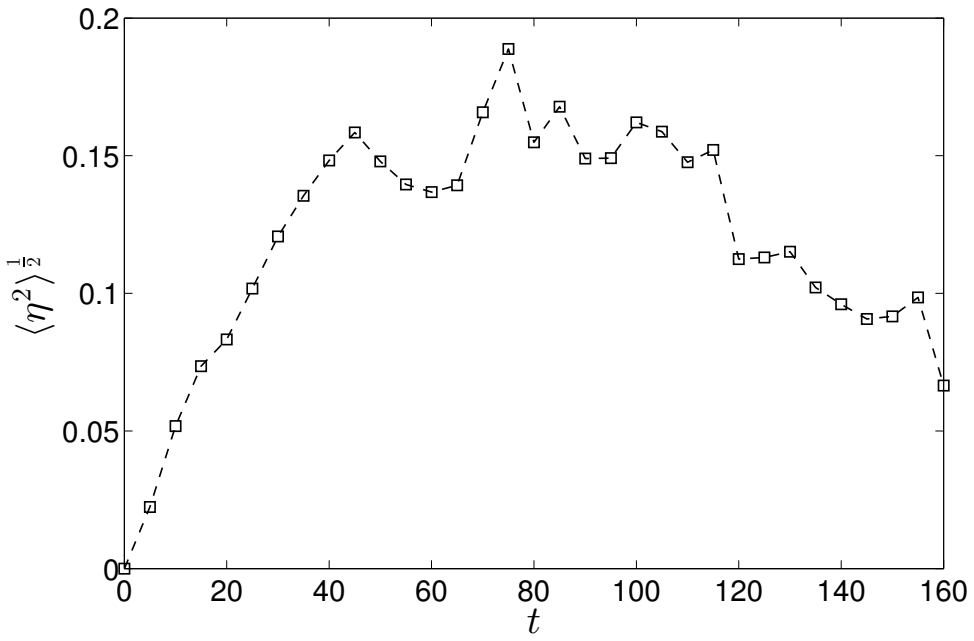

(a)

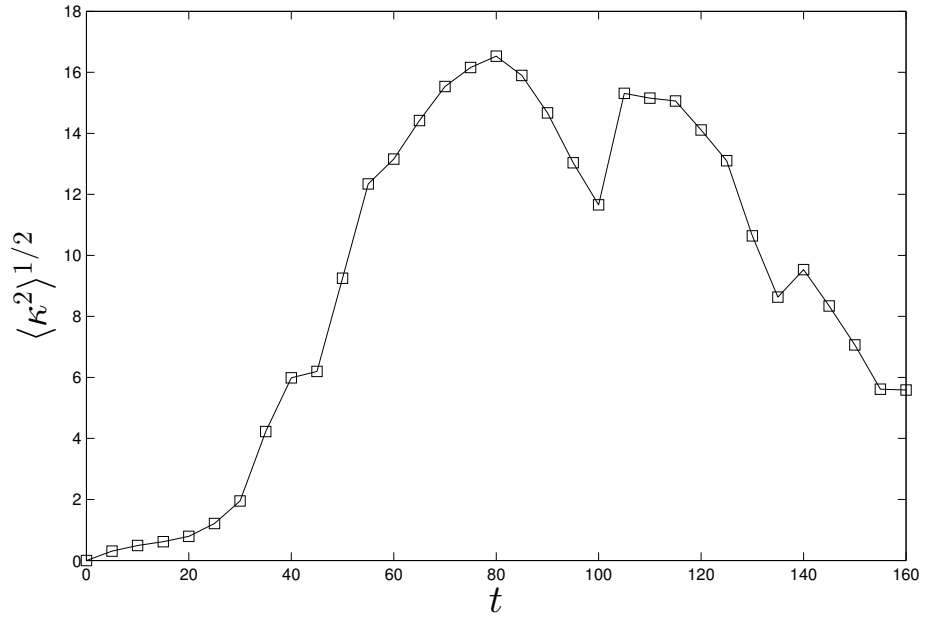

(b)

Figure 3-7: Time evolution of (a) averaged surface elevation $\langle \eta^2 \rangle^{\frac{1}{2}}$; (b) averaged surface curvature $\langle \kappa^2 \rangle^{\frac{1}{2}}$ for SFST of $Fr^2 = 10$ and $We = \infty$.

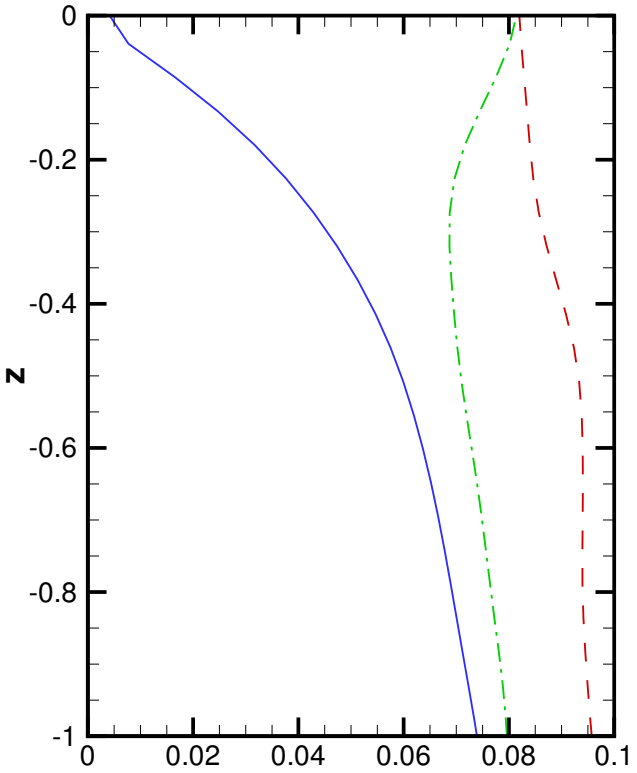

Figure 3-8: Velocity fluctuation components $u'^{rms}(z)$, $v'^{rms}(z)$ and $w'^{rms}(z)$ in WFST of $Fr^2 = 0.5$ and $We = \infty$. - - -, $u'^{rms}(z)$; — · —, $v'^{rms}(z)$; ——, $w'^{rms}(z)$. at t=90

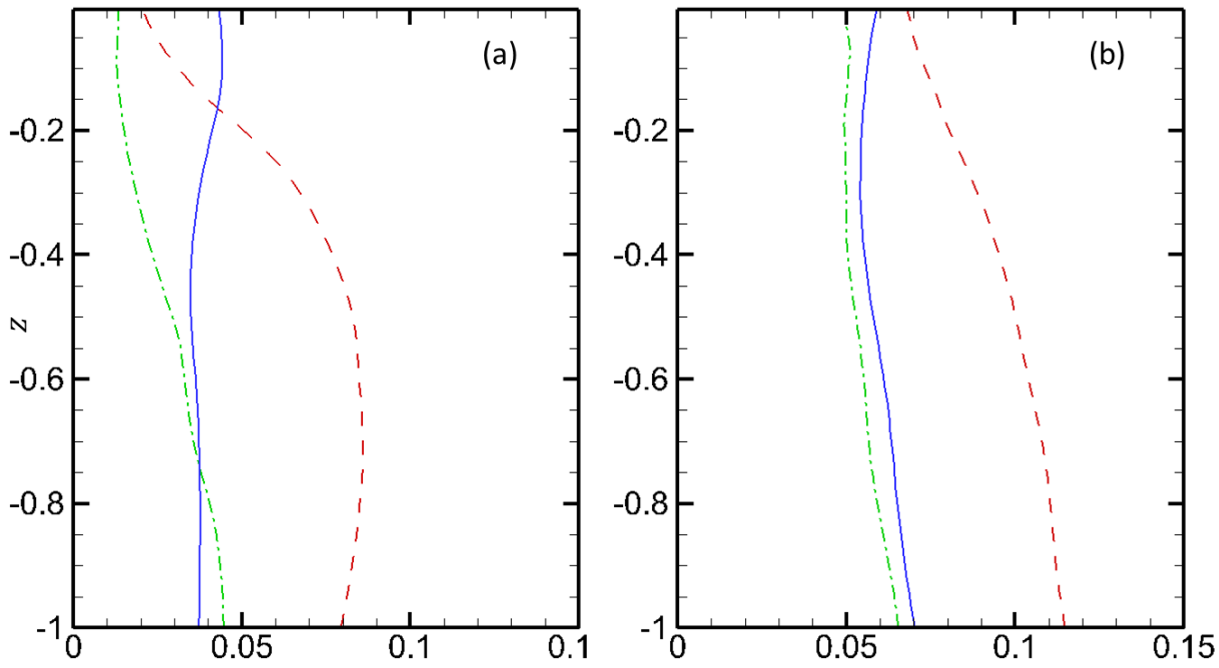

Figure 3-9: Velocity fluctuation components $u'^{rms}(z)$, $v'^{rms}(z)$ and $w'^{rms}(z)$ at (a) t=20 and (b) t=90 in SFST of $Fr^2 = 10$ and $We = \infty$. - - -, $u'^{rms}(z)$; — · —, $v'^{rms}(z)$; ——, $w'^{rms}(z)$.

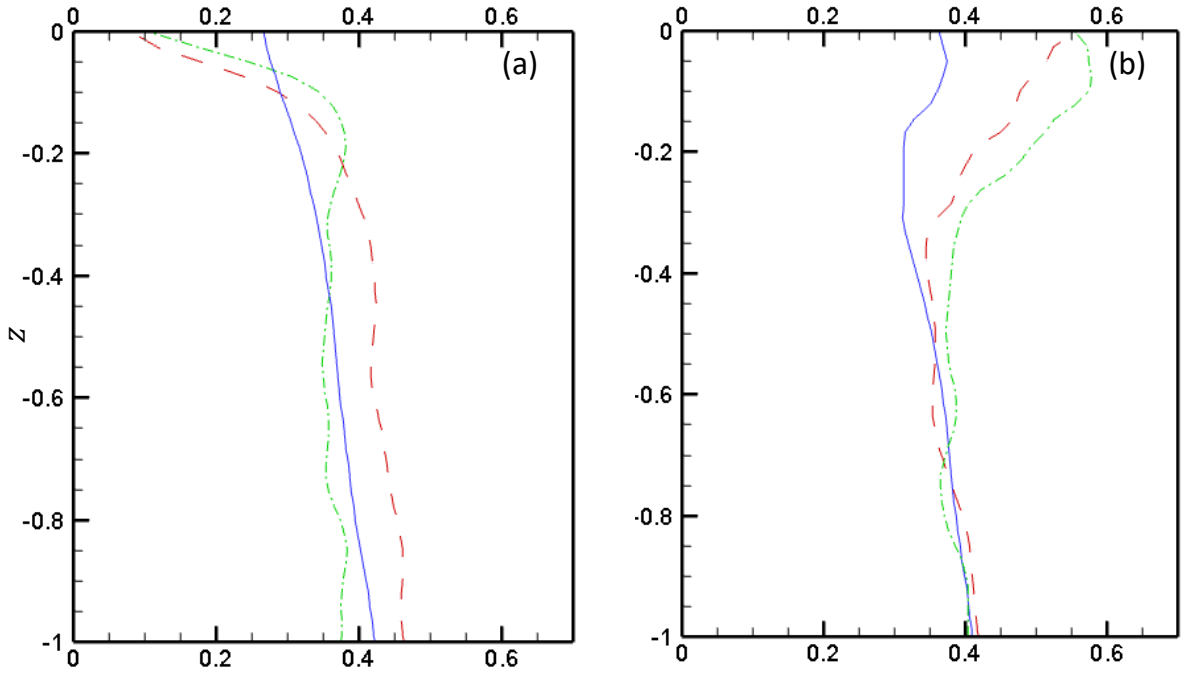

Figure 3-10: Vorticity fluctuation components $\omega_x'^{rms}(z)$ (- - -), $\omega_y'^{rms}(z)$ (— · —), and $\omega_z'^{rms}(z)$ (——) at time $t = 90$ in (a) flow WFST with $Fr^2 = 0.5$ and $We = \infty$; (b) flow SFST with $Fr^2 = 10$ and $We = \infty$.

ponents $\omega_x'^{rms}$ and $\omega_y'^{rms}$ in figure 3-10a and 3-10b for WFST and SFST, respectively. These fluctuations drop sharply over the surface layer of thickness $O(0.1)$ in WFST. In SFST, however, $\omega_x'^{rms}$ and $\omega_y'^{rms}$ are actually enhanced due to the strong surface deformations inducing horizontally-oriented coherent vortex structures. One visualization of such a vortex structure with a "tube" shape is shown in figure 3-11. Recent studies (Yu *et al.*, 2016; André & Bardet, 2017) indeed found that the horizontally-oriented vortical structure is the dominant coherent structure in FST. In addition, the main mechanism of air entrainment in FST is found to be related to the interactions of such vortex structures and the free surface. Figure 3-11 (b) shows the an entrainment event driven by such a vortex structure.

Due to the strong surface effect in WFST, near-surface turbulence exhibits clear anisotropic characteristics. In SFST, on the other hand, turbulence near the free surface becomes more isotropic due to the reduction of the surface effect. To further examine the characteristics of turbulence, we look at the normalized anisotropy tensor

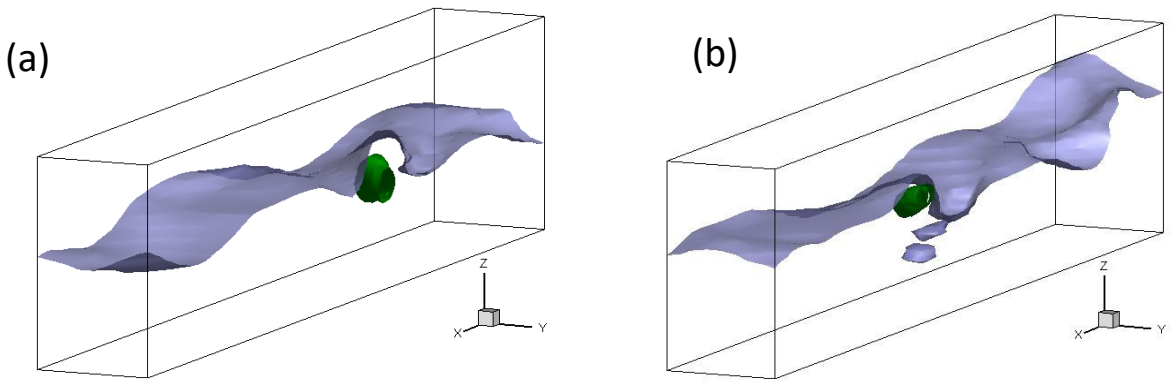

Figure 3-11: Demonstration of (a) a horizontally-oriented vortex structure with a "tube" shape under the free surface and (b) air entrainment driven by the vortex structure. Dark: vortex structure identified by $\lambda 2$ method; Light: free surface iso-surface of volume fraction $f = 0.5$.

b_{ij} defined by:

$$b_{ij} = \frac{\langle u_i' u_j' \rangle}{\langle u_k' u_k' \rangle} - \frac{1}{3}\delta_{ij} \tag{3.4}$$

This tensor has zero trace ($b_{ii} = 0$) and consequently it has two independent invariants ξ and η defined by: $6\eta^2 = b_{ij}b_{ij}$ and $6\xi^3 = b_{ij}b_{jk}b_{ki}$. Figure 3-12 shows the Lumley triangle (Pope, 2001) using (ξ, η) calculated on the plane for $z \in [-1, 0]$ in the quasi-steady stage. Both WFST and SFST follow the ISO-1C boundary of one-component dominance (stream-wise) at depth. The stream-wise component extracts energy directly from the shear flow and then transfers it to the other two components to return to isotropy (Handler *et al.*, 1993; Shen *et al.*, 1999). Nearer to the free surface, WFST moves toward the 2C point. The constraining effect of the free surface on the vertical component leads to the dominance of the two horizontal components. By contrast, SFST moves towards the ISO point indicating nearly isotropic turbulence near the free surface. Notice that instead of a physical difference, the difference of the position of (ξ, η) at $z = -1$ between WFST and SFST flows is mainly due to the turbulence randomness in the bulk flow.

Figure 3-13(a) presents the turbulent isotropy parameter J as a function of z. J

is defined by:

$$J = 1 - 9(\frac{1}{2}b_{ij}b_{ij} - b_{ij}b_{jk}b_{ki}) \tag{3.5}$$

J is bounded $J \in [0, 1]$, where $J = 1$ is fully isotopic. In the WFST case, the value of J drops sharply as z approaches 0, indicating turbulence near the free surface is highly anisotropic. For SFST, however, J approaches a value of 0.92 at the free surface suggesting nearly isotropic turbulence.

Finally, we confirm this anisotropic behavior using the three one-dimensional energy spectra (calculated from velocity fluctuations) at $z = 0$ as shown in figure 3-14. In WFST, the suppression of the vertical component is evident by the two orders of magnitude difference in the energy compared to the two horizontal components. In SFST, all three components have comparable magnitudes and follow the Kolmogorov spectra $k^{-5/3}$ of isotropic turbulence. Because of the isotropy of turbulence in the flow with anisotropic mean strain rate, turbulent closure models of the Boussinesq-type, which approximates the Reynolds stress using the mean strain rate, are likely not appropriate for sheared SFST.

3.3 Air entrainment and bubble size distribution in SFST

Brocchini & Peregrine (2001*a*) proposed a conceptual map in the (l, q)-plane for FST flows. In the SFST case of $Fr^2 = 10$ and $We = \infty$, for physical length and velocity scales of $L = 1m$ and $U = 1m/s$, say, the turbulent velocity q would be around 0.12m/s and the length scale of cavities l would be in the range between 0.01m and 0.1m. The current SFST would thus be located in the strong turbulence regime (or region 2 of Brocchini & Peregrine (2001*a*)) of the (l, q)-plane. In this regime, turbulence is sufficiently strong that neither gravity nor surface tension can maintain surface cohesion, and air entrainment is expected to happen. In this section, the total amount of air entrainment and the bubble size distribution in the SFST flow are focused and investigated.

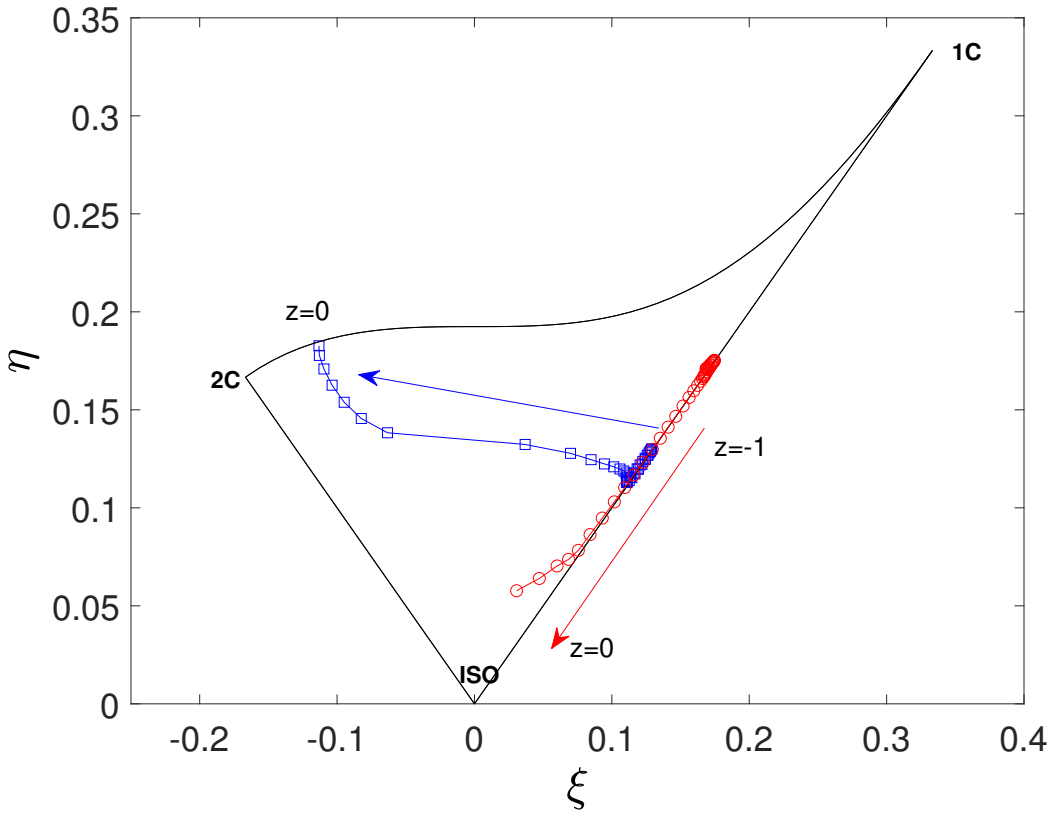

Figure 3-12: The Lumley triangle on the plane of the invariants ξ and η of the anisotropy tensor from the bulk flow $z = -1$ to the free surface $z = 0$ at $t = 90$. ○, SFST; □, WFST.

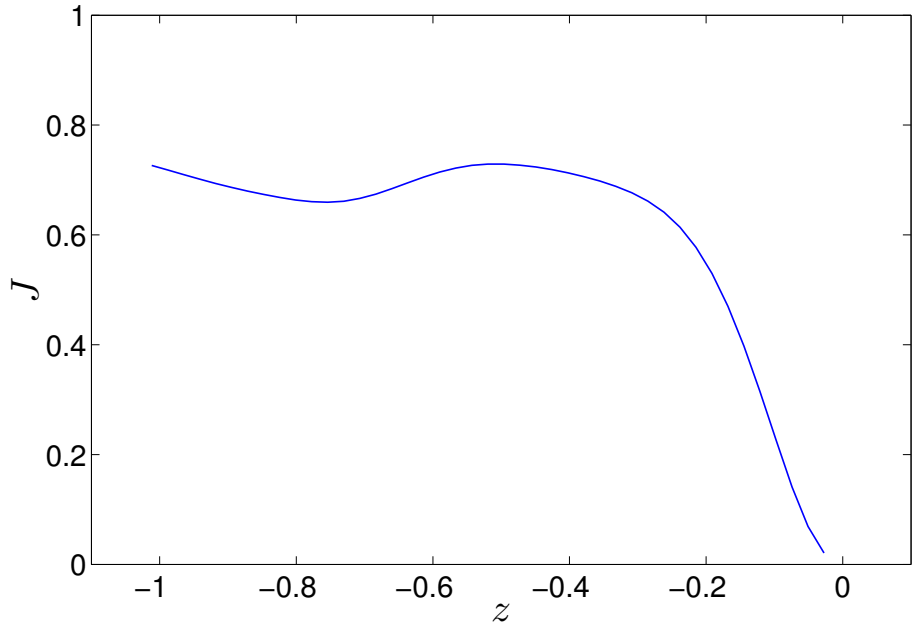

(a)

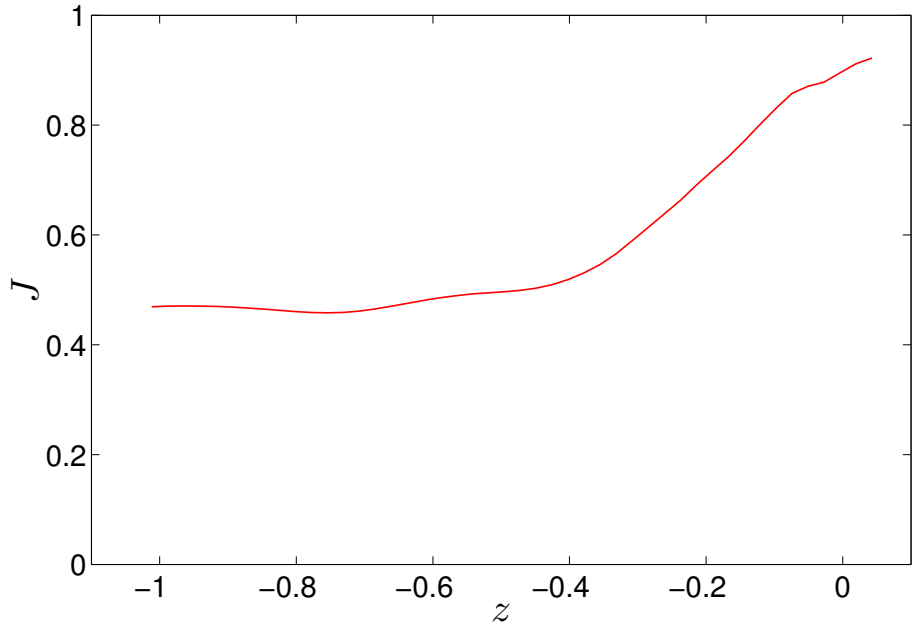

(b)

Figure 3-13: Turbulent isotropy parameter J as a function of z (a) WFST; (b) SFST.

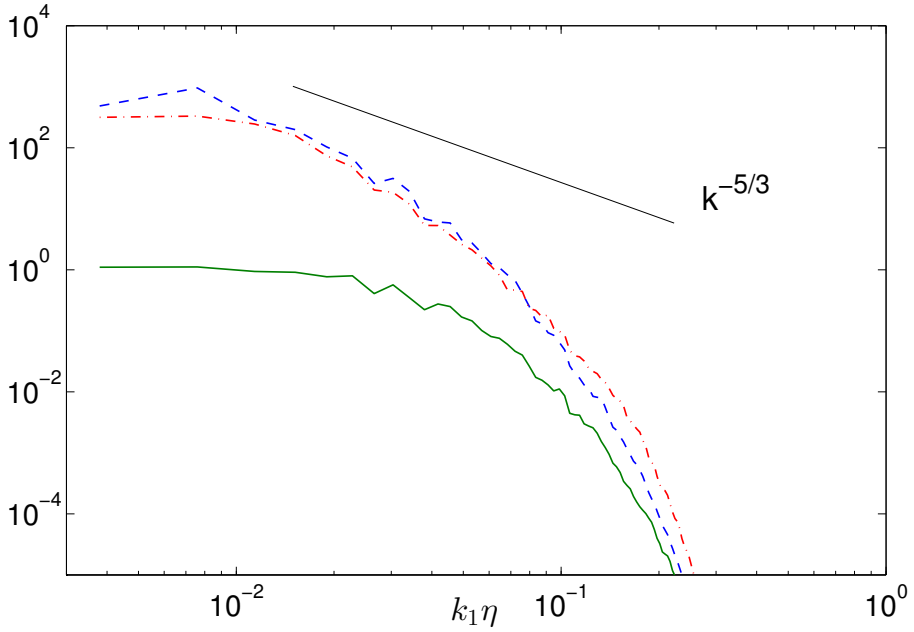

(a)

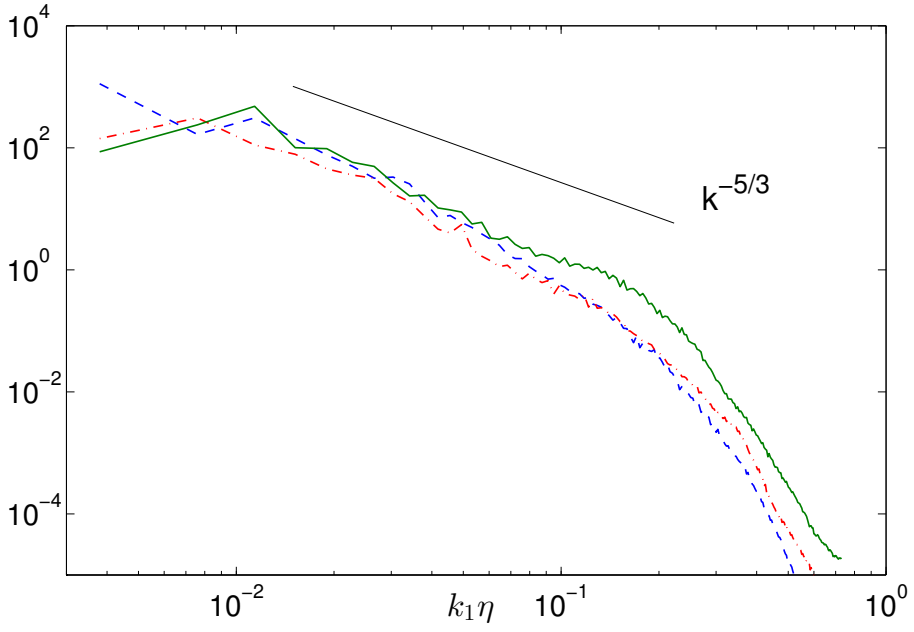

(b)

Figure 3-14: One-dimensional energy spectrum $E_{11}(k_1)$ (- - -), $E_{22}(k_1)$ (— · —), $E_{33}(k_1)$ (——) near the free surface at $t = 90$ in (a) WFST with $Fr^2 = 0.5$ and $We = \infty$; (b) SFST with $Fr^2 = 10$ and $We = \infty$.

3.3.1 Time evolution of total entrainment volume

We define $V(t)$ as the total volume of air entrainment in the computational domain. Figure 3-15 presents the evolution of $V(t)$ for the SFST case with (large) Fr^2=10 and We=∞. Air entrainment occurs after t_s≈55 and $V(t)$ continues to increase until t_e≈125, beyond which air entrainment ceases and $V(t)$ begins to decrease due to degassing. Strictly speaking, $V(t)$ is affected by concurrent air degassing throughout the entrainment period $t_s \leq t \leq t_e$ (with duration T_a), although for this problem, the degassing rate is small compared to air entrainment (will be confirmed later). For specificity and later use, we define the air entrainment rate $Q = \dot{V}(t)$, and quantify an average air entrainment rate (or average air flux) $\overline{Q}_{\mathcal{E}} = \frac{1}{T_a} V(t_e)$ as the average of Q over the entrainment period, which approximately overlaps with the quasi-steady duration of TKE, see figure 3-5. From figure 3-15, we estimate $\overline{Q}_{\mathcal{E}} \approx 0.006$ for the current SFST case.

$t \geq 125$ marks the beginning of the post entrainment period. During this period (between 125 and 160), near-surface turbulence intensity continues to decay (cf. Figure 3-5), leading to the stop of the entrainment process. The decrease in $V(t)$ in Figure 3-15 is a result of degassing (recall that cVOF conserves volume to machine accuracy). Analogous to the average entrainment rate $\overline{Q}_{\mathcal{E}}$, we estimate the average degassing rate over the post entrainment period $\overline{Q}_d = \frac{V(t=125)-V(t=160)}{160-125} \approx 0.0006$. We see that $\overline{Q}_d$ is an order of magnitude smaller than $\overline{Q}_{\mathcal{E}}$ (which is ≈ 0.006). This supports our earlier assumption that degassing is relatively not important during the entrainment period.

3.3.2 Time evolution of bubble size distribution

In the DNS using cVOF, we are able to obtain the bubble spectral $N_a(r)$ in the bulk. Figure 3-16 shows $N_a(r)$ obtained from DNS at different instances of time within the quasi-steady entrainment period ($55 \lesssim t \lesssim 125$), for the SFST case with $Fr^2 = 10$ and $We = \infty$. At a relatively early instant of the entrainment period, $t = 60$, $N_a(r)$

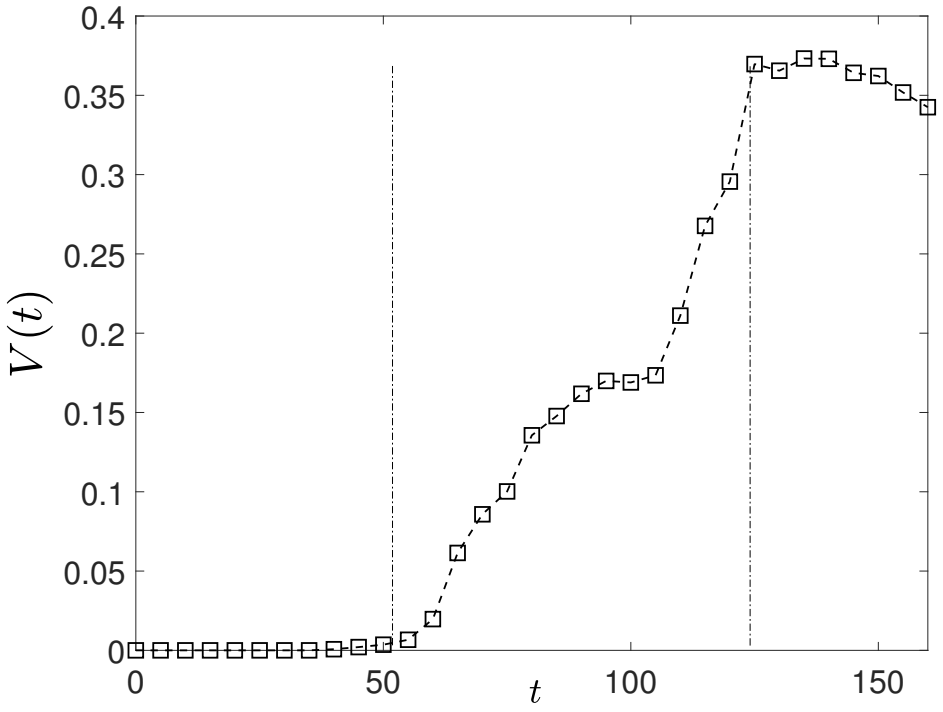

Figure 3-15: Evolution of total volume of air entrainment $V(t)$ for SFST of $Fr^2 = 10$ and $We = \infty$.

follows closely the following power-law.

$$N_a(r) \propto r^{-10/3} \tag{3.6}$$

As t increases, the overall magnitude of $N_a(r)$ increases as new air is entrained into the water volume. However, $N_a(r)$ is seen to deviate from the initial $-10/3$ power-law, with the value of $N_a(r)$ at small r increasing faster than that at large r.

In the initial phase of SFST air entrainment, $t \gtrsim t_a$, before significant bubble fragmentation has occurred, we argue that $N_a(r)$ should approximately follow the power-law in (3.6). We notice this power-law is consistent with the model by Garrett *et al.* (2000). Here we remark that despite the same power-law, the mechanism of SFST entrainment is different than the fragmentation scenario considered in Garrett *et al.* (2000). In the model of Garrett *et al.* (2000), a constant source of air is entrained at a given (large) scale which cascades and creates small bubbles, through bubble fragmentation, into a quasi-steady distribution following a $-10/3$ power-law. On the other hand, the entrainment in the SFST flow is driven by near-surface turbulence and is expected to occur over a broad range of scales. In particular, the power-law of (3.6) is a result of near-surface isotropic SFST turbulence spectra, and the power-law would be modified accordingly if a different near-surface energy spectrum obtains. A physical/mechanisic model for SFST entrainment by connecting the energy of near-surface turbulence and the energy for bubble entrainment will be provided in Chapter 4.

As the (quasi-steady) SFST air entrainment continues, the evolution of $N_a(r)$ depends on two ongoing processes: (a) the surface entrainment over a scale given by (3.6); and (b) the subsequent fragmentation cascade of all the entrained bubbles up to this point. The combined process is complex and it is not clear whether a power-law distribution would obtain (or if so, what the slope might be). To provide some qualitative insight into this evolution, we suggest a heuristic model which combines the two main mechanisms of ongoing SFST entrainment and subsequent fragmentation cascades of these bubbles. For the ongoing entrainment process, bubbles are considered

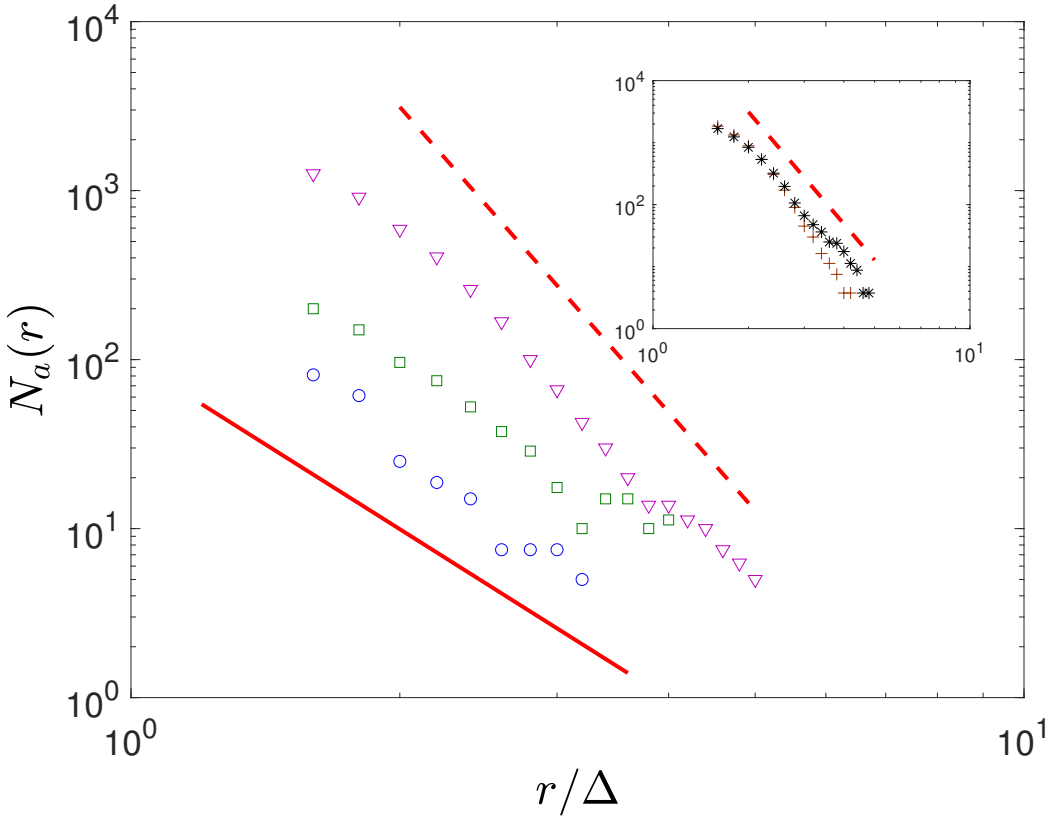

Figure 3-16: Bubble size spectrum $N_a(r)$ as a function of r for SFST of $Fr^2 = 10$ and $We = \infty$ in the entrainment period: $t = 60$ ($\circ$), $t = 70$ ($\square$), and $t = 120$ ($\triangledown$). — $r^{-10/3}$ and - - -: r^{-6}. Inset:$N_a(r)$ in the post-entrainment period: $t = 135$ ($*$) and $t = 160$ ($+$). $t_a = 60$

to be entrained instantaneously over a broad range of scales given by (3.6). For the bubble fragmentation process, we consider a canonical problem of the fragmentation of an initial population of bubbles following a size spectrum of (3.6) in turbulence (see appendix B). For the underlying turbulence field, we use isotropic homogeneous turbulence (IHT) field to approximate the isotropic near-surface turbulence in the SFST. For simplicity, the evolving size spectrum is approximated by a power law with time-dependent slope given by:

$$N_0(r,\tau) = r^{-(a\tau+\beta_0)} V_0^{-1} \tag{3.7}$$

where τ is the evolution time, β_0=$-10/3$ is prescribed, and V_0 is a normalization factor so that integrated volume of (3.7) is 1 . From appendix B, we find a ≈0.24. Finally, we assume that $N_a(r,t)$ in SFST is a convolution of (3.7):

$$N_a(r,t) = \int_{t_s}^{t} dt_0 Q(t_0) N_0(r, t-t_0) \ , \quad t > t_s \ , \tag{3.8}$$

where $Q(t_0)$ is the volume entrainment rate at $t = t_0$.

The usefulness of the heuristic model must be checked against DNS prediction. Figure 3-17 shows the comparison of 3.8 using the $Q(t)$ from DNS. Despite the simplicity of (3.8) and the substantial approximations involved, especially (3.7), the qualitative correspondence between (3.8) and DNS data suggests that the underlying processes represented in (3.8) are likely responsible for the evolution of $N_a(r)$ in figure 3-16.

Further evidence of the degassing process in the post-entrainment period is seen in figure 3-16(inset) where the number of large bubbles decreases faster than the number of small bubbles for $N_a(r)$ at $t = 135$ and $t = 160$. This indicates that larger bubbles are escaping the water volume faster due to buoyancy effects. Further elucidation of the general degassing processes would benefit from Lagrangian tracking which is difficult in the context of VOF (in the presence of ongoing turbulent entrainment, fragmentation, coalescence and advection), and is beyond the scope of the present work.

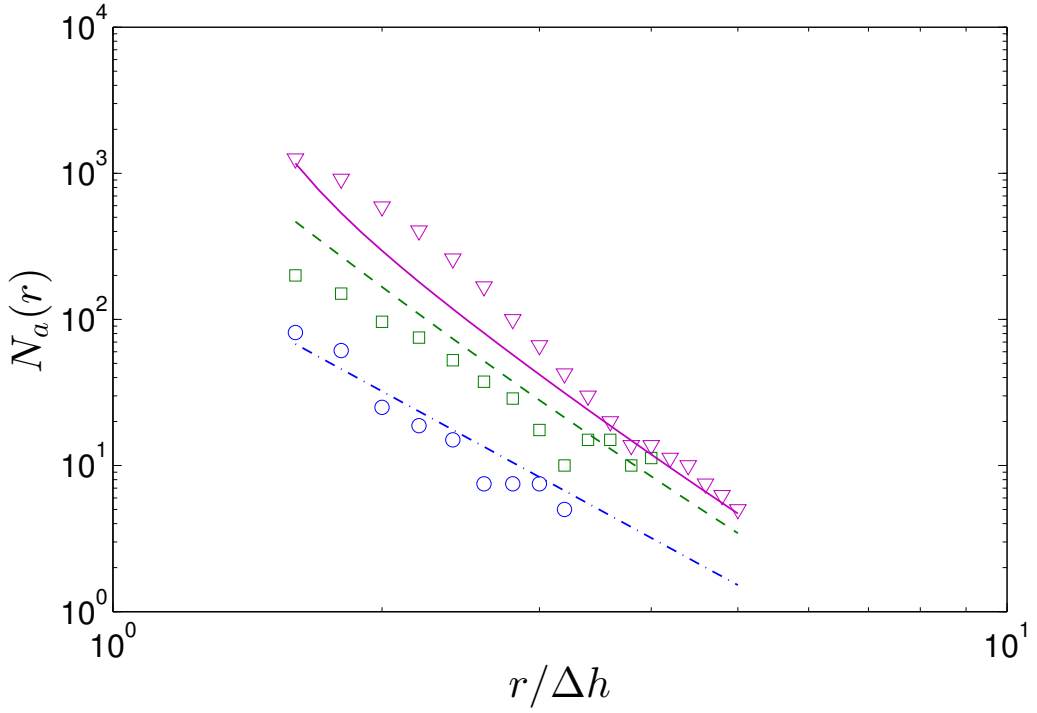

Figure 3-17: Comparison of $N_a(r)$ at different time instances between equation (3.8) and DNS results of SFST with $Fr^2 = 10$ and $We = \infty$. DNS (○) and model prediction (— - —) at t=60; DNS (□) and model prediction (- - -) at t=70; and DNS (▽) and model predictions — at t=120.

Analogous to $\overline{Q}_{\mathcal{E}}$ for the average entrainment rate, we define for later reference the average rate of increase of bubble spectrum $\overline{Q}_{\mathcal{N}}(r) = \frac{1}{T_a} N_a(r, t = t_e)$ (averaged over the same entrainment period as $\overline{Q}_{\mathcal{E}}$).

3.4 Summary

In this section, we perform DNS of a canonical three-dimensional two-phase (air and water) viscous turbulent flow with turbulent kinetic energy supplied by a sheared underlying water bulk flow. We investigate the characteristics of strong free-surface turbulence (SFST) and air entrainment associated with large Fr and We. We elucidate the qualitatively distinct characteristics of strong versus weak free-surface turbulence. For WFST, the near-surface flow is characterized by the presence of the inner surface and outer blockage layers, resulting in strong anisotropy of the FST. Furthermore, free surface displacements/disturbances are small and no air entrainment is observed. In contrast, for SFST, the free surface is strongly distorted by turbulence with significant displacements, distortions and, ultimately, break-up of the interface. In the underlying flow, the surface and blockage layers weaken and disappear, and the FST becomes almost isotropic. We document the latter by quantifying the anisotropy tensor b_{ij} and an isotropic parameter J of the SFST. We also find that the corresponding turbulence energy spectrum follows approximately the $k^{-5/3}$ Kolmogorov spectra of isotropic turbulence.

We use a cavity identification algorithm to quantify the air entrainment volume as well as the bubble size spectrum $N_a(r)$ of the entrained air in the bulk flow. With negligible surface tension, $N_a(r)$ is observed to follow a $r^{-10/3}$ power law at the early stage of the entrainment period, reflecting the size distribution of the surface entrainment. As the entrainment process continues accompanied by ongoing turbulent fragmentation of already entrained air, the power-law behavior of $N_a(r)$ is lost. Using the given scaling of the entrainment size distribution, and incorporating the evolution of the size spectrum of an initial population of bubbles in IHT, we provide a heuristic model that qualitatively matches and explains the salient evolution behavior of $N_a(r)$

obtained from DNS.

Chapter 4

Theoretical model of bubble size distribution of SFST entrainment

Turbulence near an interface is the driving factor to cause surface breakups (eg. entrainment and fragmentation) and controls the resulted bubble size distribution. In this thesis, we specifically focus on air entrainment across a free surface induced by SFST and study the corresponding bubble size distribution. To quantify the entrainment bubble size distribution, we define $\mathcal{N}_a^E(r)$ as the bubble size spectrum per unit area of the initial flat free surface. Here we use $\mathcal{N}_a^E(r)$ to represent the specific bubble size spectrum resulted by SFST driven entrainment only. The actual bubble size spectrum in the bulk $N_a(r)$ is also influenced by other physical processes such as fragmentation and degassing. We develop a new parameterization model for $\mathcal{N}_a^E(r)$ based on both an energy argument and a dimensional argument. The new model predicts that there are two regimes of $\mathcal{N}_a^E(r)$, separated by the capillary length scale r_c. In each regime, $\mathcal{N}_a^E(r)$ shows an unique scale dependence. In reality, $\mathcal{N}_a^E(r)$ is difficult to be directly measured. To obtain $\mathcal{N}_a^E(r)$, the bubble size spectrum in the bulk, $N_a(r)$, needs to be measured first before significant bubble fragmentation and degassing happen. Then $\mathcal{N}_a^E(r)$ can be obtained by normalizing $N_a(r)$ using the area of the initial flat free surface. The new models help to answer the following three key questions regarding the mechanisms of bubble entrainment in SFST. First, why there exist two bubble size regimes and what is the mechanism of the formation of

each one? Second, why the bubble size spectrum shows a power-law in each of the regimes and what is the exact value of the power in each regime? Third, what is the transition scale separating the two regimes? The new models are partially supported by experimental and numerical results in the literature.

Inspired by the diagram of (L,q)-plane in Brocchini & Peregrine (2001*a*), we derive a lower r_l and upper bound r_u of the entrainment bubble size by considering the stabilizing effects of gravity and surface tension against the free-surface disturbance due to turbulence,. We plot r_l and r_u in a diagram of (r, ϵ)-plane analogous to the diagram of (L,q)-plane by Brocchini & Peregrine (2001*a*). r_l and r_u cross at (r_c, ϵ_c), where ϵ_c is a critical turbulence dissipation rate for bubble entrainment. For $\epsilon > \epsilon_c$, the disrupting effects of free-surface turbulence (FST) on the interface are strong relative to the stabilizing effects of g and σ/ρ. This is the regime of SFST with substantial air entrainment. For $\epsilon < \epsilon_c$, air entrainment is significantly suppressed by either g or σ/ρ, resulting in a regime of weak FST (WFST). The regime of WFST can be further divided into three different regimes that correspond to dominant g, σ/ρ, and both.

4.1 Model of entrainment bubble size distribution in turbulence

4.1.1 Dimensional argument

In this section, we derive a new model to parameterize the bubble size distribution of SFST entrainment by performing a dimensional analysis. In Garrett *et al.* (2000) and Deane & Stokes (2002), they used $N(r)$ (of dimension L^{-4}), the entrainment bubble size spectrum per unit volume for the dimensional analysis. For entrainment across the free surface, we use $\mathcal{N}_a^E(r)$ (of dimension L^{-3}), the bubble size spectrum per unit area of the initial flat free surface, as a more appropriate variable for the dimensional argument. The generation of entrained bubbles is essentially the separation process of the free surface. Therefore, only the initial free surface area is relevant, while the

dimension of depth is not. In fact, the different normalization in the definition of $\mathcal{N}_a^E(r)$ and $N(r)$ do not change the scale dependence of interest, but only influences the magnitude.

We consider the stabilizing effects of gravity g (of dimension LT^{-2}) and surface tension σ/ρ (of dimension $L^{-2}T^{-2}$) against the interface separation caused by turbulence. For large bubbles, the gravity effect is dominant so that $n(r)$ is assumed to linearly depend on g^{-1}. On the other hand, $n(r)$ is linearly dependent on $(\sigma/\rho)^{-1}$ for small bubbles. These two assumptions are confirmed by the DNS results in Chapter 5. Also, turbulent dissipation rate ϵ (of dimension L^2T^{-3}) is considered to be a relevant variable as it reflects the intensity of turbulence. Through dimension matching, we obtain:

$$n(r) \propto g^{-1}\epsilon^{2/3}r^{-10/3} \tag{4.1}$$

for large bubbles and

$$n(r) \propto (\sigma/\rho)^{-1}\epsilon^{2/3}r^{-4/3} \tag{4.2}$$

for small bubbles. As a consequence, $N(r)$ should follow the above two equations. Equation (4.1) and (4.2) suggest two distinct regimes of bubble size distribution depending on bubble radius. $n(r)$ scales as $r^{-10/3}$ for large r, while $r^{-4/3}$ for small r. These two power-laws are comparable to those in equation (1.1) and (1.2) (Garrett *et al.*, 2000; Deane & Stokes, 2002). In addition, the new analysis suggests that the two regimes are formed due to the dominance of the stabilizing effect of either gravity or surface tension on the interface separation. By that consideration, the critical radius r_c separating the two regimes is the capillary length scale at which the gravity and surface tension effects are comparable or Bond number ($Bo = \frac{\rho g(2r_c)^2}{\sigma}$) is of order 1. Then r_c is estimated to be:

$$r_c \approx 0.5\sqrt{\sigma/\rho g} \tag{4.3}$$

Equation (4.3) suggests r_c is not the Hinze scale r_H. More detailed discussions on r_c will be addressed in the section 4.1.3. It is also noted that $n(r)$ or $N(r)$ is positively correlated with ϵ, suggesting that more air bubbles are generated by stronger turbulence. Strong turbulence is more likely to overcome the stabilizing effect of gravity or

surface tension, and breaks the initial interface to form new bubbles.

4.1.2 Model derivation based on energy argument

In this section, we provide a direct physical/mechanistic derivation of equation (4.1) and (4.2) through an energy argument. Two basic assumptions are involved in the derivation. First, the energy of bubble generation is assumed to be supplied by surrounding turbulence. Brocchini & Peregrine (2001*a*) used the same assumption when they derived the upper bound of the transition zone of weak and strong free surface turbulence. The results in §3.2.2 also showed that air entrainment is highly correlated with turbulence kinetic energy. Second, the void fraction of bubbles is assumed to be small and does not affect the dynamics of turbulence in the water (Garrett *et al.*, 2000).

Considering the entrainment/formation process of a spherical air bubble of radius r, it is separated from the free surface to a depth αr when it has lost its overall motion. α is a constant of order 1. The energy of entraining such a bubble is

$$E_b(r) = g\frac{4}{3}\pi r^3 \alpha r + \frac{\sigma}{\rho} 4\pi r^2 \tag{4.4}$$

We point out that α not only indicates the depth of the entrained bubble, also includes the correction due to the spherical bubble assumption. Recall that $n(r)$ is defined as the bubble size spectrum per interface area. The total number of bubbles of radius r in the whole domain can be written as $n(r)A_h dr$, where A_h is the area of the initial free surface. Considering a particular r, the total energy required for the bubble generation $E_t(r)$ is further written as:

$$E_t(r) = n(r)A_h dr E_b(r) = n(r)A_h dr(g\frac{4}{3}\pi r^3 \alpha r + \frac{\sigma}{\rho} 4\pi r^2) \tag{4.5}$$

According to the first assumption, $E_t(r)$ is proportional to turbulence energy and this amount of energy is supplied by near-surface turbulence over a region of length scale r (surrounding the entrained bubbles) argued by Brocchini & Peregrine (2001*a*).

Define $E(k)$ as the turbulence energy spectrum. The energy of turbulence at length scale $1/k$ can be written as $|E(k)dk|$. As the entrained air bubbles vary in size over a large range, we consider turbulence energy at the length scale of $r \sim 1/k$. We further obtain:

$$|E(k)dk| \propto |E(r^{-1})dr^{-1}| = E(r^{-1})r^{-2}dr \tag{4.6}$$

Connecting equation (4.5) and (4.6)gives:

$$n(r)A_h dr(g\frac{4}{3}\pi r^3\alpha r + \frac{\sigma}{\rho}4\pi r^2) \propto |E(r^{-1})dr^{-1}|A_h r \tag{4.7}$$

Notice that the energy for the entrainment of bubbles of radius r is considered to come from turbulence over a volume $A_h r$ near the free surface. Equation (4.7) can be further simplified as:

$$n(r)(g\frac{1}{3}\alpha r + \frac{\sigma}{\rho}\frac{1}{r}) \propto E(r^{-1})/r^4 \tag{4.8}$$

According to the results in §3.2.3, turbulence near the free surface shows great isotropy in SFST flows, characterized by large Fr and We. In addition, the turbulence energy spectrum can be described by the Kolmogorov's energy spectrum $E(r^{-1}) \propto \epsilon^{2/3}r^{5/3}$ in the inertial subrange. Then Equation (4.8) turns to be:

$$n(r)(g\frac{1}{3}\alpha r + \frac{\sigma}{\rho}\frac{1}{r}) \propto \epsilon^{2/3}r^{-7/3} \tag{4.9}$$

Consider the term $f(r) = g\frac{1}{3}\alpha r + \frac{\sigma}{\rho}\frac{1}{r}$ in the left-hand side of equation (4.9). At large r, $f(r)$ is dominated by the term $g\frac{1}{3}\alpha r$. Equation (4.9) becomes $n(r) \propto g^{-1}\epsilon^{2/3}r^{-10/3}$. On the other hand, when the term $\frac{\sigma}{\rho}\frac{1}{r}$ in $f(r)$ becomes more important at small r, equation (4.9) becomes $n(r) \propto (\sigma/\rho)^{-1}\epsilon^{2/3}r^{-4/3}$. The separating scale of the two regimes happens when the term $g\frac{1}{3}\alpha r$ and $\frac{\sigma}{\rho}\frac{1}{r}$ become comparable. Thus, we obtain the expression of the critical radius separating the two bubble size regimes $r_a = \sqrt{3\sigma/\alpha\rho g}$. r_a in fact is the capillary length scale at which $Bo \approx 1$. The above conclusions based on (4.9) are consistent with those obtained by the dimensional argument.

Several remarks are in order. First, the scaling $N(r) \propto r^{-10/3}$ for $r > r_c$ in the current model is the same with the one obtained by Garrett *et al.* (2000). However, the underlying physical processes considered in these two models are different. In the model of Garrett *et al.* (2000), a constant source of air is entrained at a given (large) scale which cascades and creates small bubbles, through bubble fragmentation, into a quasi-steady distribution following a $-10/3$ power-law. Our model considers the entrainment process driven by near-surface turbulence. In particular, the two power-laws are a result of near-surface isotropic SFST turbulence spectra, and the power-law slopes would be modified accordingly if a different near-surface energy spectrum obtains. Second, the surface entrainment model considers the process of SFST entrainment only, but not the subsequent bubble fragmentation and degassing. As shown in §3.3.2, bubble fragmentation in turbulence causes an evolution of the bubble size spectrum in the bulk. Finally, for the evolution of the aggregate spectrum, bubble degassing should be incorporated especially over longer time. In the current SFST, we show in §3.3.2 that the degassing is negligible by comparing the degassing rate to the entrainment rate.

Figure 4-1 shows the comparison of $\mathcal{N}_a^E(r)$ in (4.9) (with $\alpha = 5$) and the measured bubble size spectrum inside breaking waves from literature. We use the notation $N_a(r)$ for the bulk bubble size spectrum measured by identifying the sizing bubbles in the bulk directly from experiments and DNS. For the interest of scale dependence of the bubble size spectrum, all the data and (4.9) are normalized by their own values at $r = 2mm$. Interestingly, even though (4.9) is derived from a scenario of SFST entrainment, it shows quantitative agreement with $N_a(r)$ measured in breaking waves. The reason for this consistency is discussed later in §4.1.4. We observe that all the bubble size spectra show two regimes. The transition of the two regimes r_a happens at $1 \sim 2mm$. Considering real water and air, (4.3) suggests $r_c \approx 1.5mm$, which is consistent with transition scale shown by the existing data and indicates that the transition scale is the capillary length scale r_c. For bubbles of size larger than r_a, the new model agrees well with the existing data, which all suggests a power-law of $r^{-10/3}$. For $r < r_a$, our model predicts a power-law of $r^{-4/3}$, which is very close to

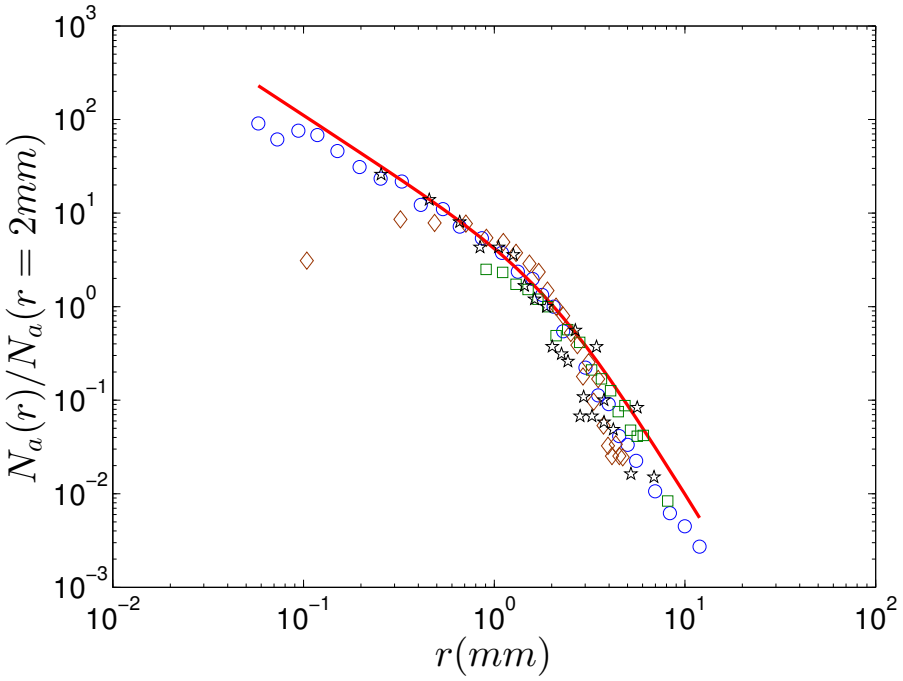

Figure 4-1: Comparison of $\mathcal{N}_a^E(r)$ in (4.9) (with $\alpha = 5$) and the measured bubble size spectrum $N_a(r)$ inside breaking waves from literature. All the data and (4.9) are normalized by their own values at $r = 2mm$. ——, equation (4.9); ∘, Deane & Stokes (2002); □, Rojas & Loewen (2007); ♢, Loewen *et al.* (1996); ⋆, Wang *et al.* (2016).

the data of Deane & Stokes (2002), Rojas & Loewen (2007), and Wang *et al.* (2016). However, the data from Loewen *et al.* (1996) does not follow the predicted power-law.

4.1.3 $(r - \epsilon)$ regime map for air entrainment in FST flow

We have pointed out that the separating scale of the two regimes observed in figure is the capillary length scale r_c instead of the Hinze scale r_H. r_H happens when (turbulence) Weber number $We_t = \rho\overline{v^2}(2r_H)/\sigma$ is equal to a critical value We_c. Experimental measurements suggest that We_c is in a range between 3 and 4.7 (MARTÍNEZ-BAZÁN *et al.*, 1999; Lewis, 1982). $\overline{v^2}$ is the turbulence fluctuation over a distance d. For isotropic homogenous turbulence, $\overline{v^2} \approx 2.0(\epsilon d)^{2/3}$. For bubbles of radius $r < r_H$, the restoring force of surface tension prevents further bubble fragmentation by turbulence. According to Hinze (1955); Deane & Stokes (2002), r_H has the following

expression:

$$r_H = 2^{-8/5}(\sigma/\rho We_c)^{3/5}\epsilon^{-2/5} \tag{4.10}$$

To be noticed, r_H defines a critical length scale for bubble fragmentation in turbulence, but not a lower bound of the size of entrained bubbles. Bubbles of radius smaller than r_H can still be generated by bubble entrainment across the free surface (or fragmentation of large bubbles, which will discussed in later section). For a bubble of radius $r < r_H$ or curvature $\kappa > 1/r_H$, the surface tension force $\sigma\kappa$ stabilizes the spherical bubble surface and prevents significant interfacial deformation. Instead, in the entrainment process, the free surface of $\kappa \gg 1/r_H$, turbulence fluctuations can induce significant interfacial deformation of length scale smaller than r_H on the flat free surface and further entrainment of bubbles of radius smaller than r_H. We should expect a lower bound of the size of entrained bubbles r_l when $We_t = \rho\overline{v^2}(2r_l)/\sigma = We_l \ll 1$. In this case, surface tension forces are much stronger than turbulence fluctuations and any interfacial deformation of scale smaller than r_l is restored by surface tension. Then r_l is expressed as:

$$r_l = 2^{-8/5}(\sigma/\rho We_l)^{3/5}\epsilon^{-2/5} \tag{4.11}$$

Analogous to r_l , a critical length scale r_u is defined when the Froude number $Fr_t^2 = \overline{v^2}/g(2r_u) = Fr_u^2 \ll 1$. When $r > r_u$, the the stabilization force of gravity on the interface significantly exceeds the turbulence fluctuations. Therefore, entrainment of bubbles of size larger than r_u is suppressed by gravity and r_u provides a upper bound of the bubble size. Similar to the derivation of (4.11), we provide the following expression for r_g:

$$r_G = 4(Fr_u^2 g)^{-3}\epsilon^2 \tag{4.12}$$

As pointed out early, r_l and r_u determine the general range of size of entrained bubbles. In addition, the existences of r_l and r_u suggest a critical value of ϵ when r_l becomes equal to r_u.

$$\epsilon_c = C_\epsilon g^{5/4}(\sigma/\rho)^{1/4} \tag{4.13}$$

where C_ϵ is a constant. When $\epsilon > \epsilon_c$, air entrainment can happen. Otherwise, no entrainment can happen. Considering air-water interface and earth gravity, ϵ_c is expected to be an universal constant.

Considering $We_l = 0.1$ and $Fr_u^2 = 0.1$, we plot a conceptual diagram of $(r - \epsilon)$ for bubble entrainment across air-water free surface in free surface turbulent flows. This plot is similar to the $(L - q)$ plot in Brocchini & Peregrine (2001*a*). Corresponding to the four regimes in Brocchini, we can also identify four regimes from figure 4-2. $\epsilon_c \approx 0.02 Wkg^{-1}$ separates the diagram into two parts. The corresponding length scale at ϵ_c is the capillary length scale r_c, which is around $1.5mm$ as shown in the figure. The regime 2 on the top part of is the strong turbulence regime where neither gravity nor surface tension can maintain the cohesion of the free surface and air entrainment happens. The plots of r_l and r_u define the boundaries of regime 2, and determine the range of bubble size as well. As ϵ increases, the size range of the entrained bubbles becomes wider. This is mainly because of the widening of the inertial range in strong turbulence. As r_u and r_l define the upper and lower bound of the size of entrained bubbles, the shaded areas are unreachable. In the lower part of the diagram, surface tension or gravity becomes sufficiently strong to stabilize the free surface and prevent air entrainment. To be specific, in regime 1, the length scale is smaller than r_l (and smaller than r_G), suggesting that surface tension forces mainly stabilize the free surface (with unimportant gravity forces). On the other hand, in regime 3, the length scale is larger than r_u (and larger than r_l), which indicates that gravity forces mainly stabilize the free surface (with unimportant surface tension forces). In regime 0, both gravity and surface tension forces become important and greatly stabilize the free surface.

4.1.4 Bubble fragmentation in turbulence

Notice that the derivation in §4.1.2 considers a scenario of bubble entrainment across the free surface, but ignores the further bubble fragmentation process in turbulence. In fact, once the bubbles are entrained, they experience fragmentation in turbulence. This fragmentation process is expected to cause a deviation of the bubble size

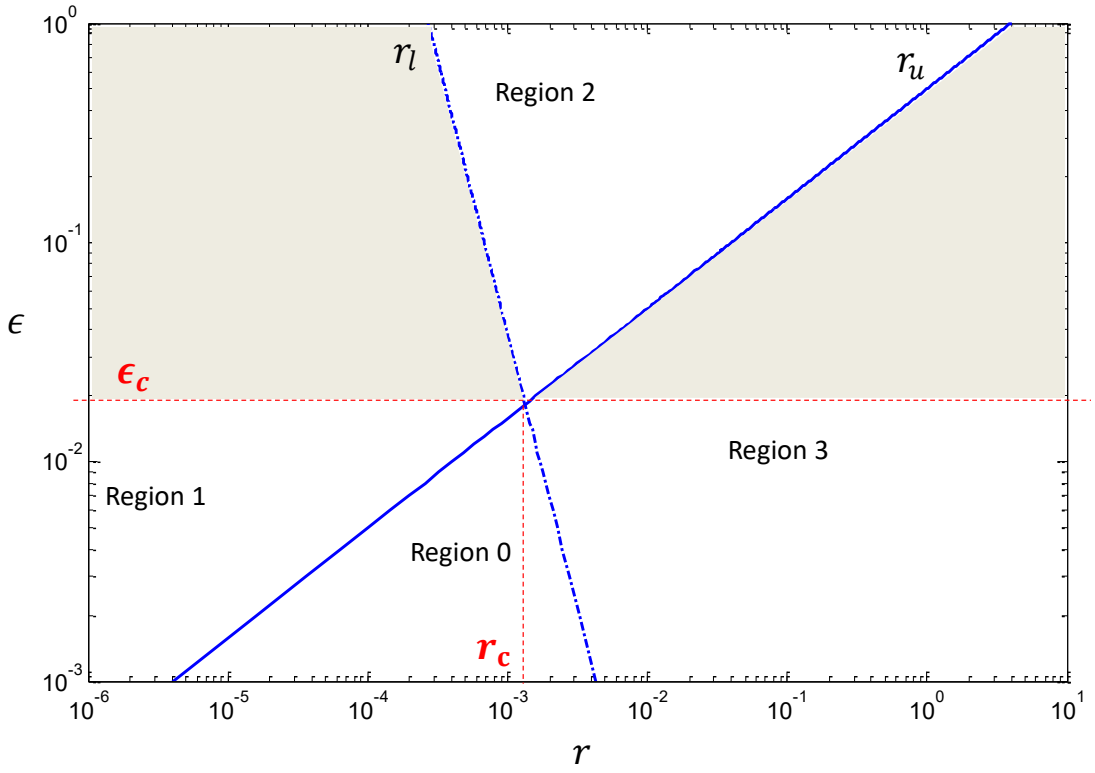

Figure 4-2: Conceptual diagram of the (ϵ, r)-plane for turbulence driven bubble entrainment near air-water interface. — · —, the lower bound of bubble size r_l; ——, the upper bound of bubble size r_u. The shaded areas are unreachable. The critical value of turbulence dissipation rate for entrainment is $\epsilon_c \approx 0.02 W/kg$. The capillary length scale is $r_c \approx 1.5 mm$.

spectrum (Deane & Stokes, 2002; Deike *et al.*, 2016). The detailed effects of the fragmentation process on the evolution of bubble size spectrum still remain unclear. In this section, we would like to discuss the physical processes of bubble fragmentation in turbulence and its connection to the entrainment process, depending on the size of the bubble under fragmentation.

For a bubble of size much larger than the turbulence inertial range(l_{DI}, l_{EI}), its fragmentation process is analogous to an entrainment process. The surface of the bubble can be considered as an initial free surface. The energy argument used in the section 4.1.2 can be extended to this case. For an initial bubble of radius $l > l_{EI}$ in turbulence. Small bubbles of size can be separated by turbulence structures of length scale comparable to r, resulting the bubble plume. The new generated bubbles are expect range in size comparable to the turbulence inertial range. Say a bubble of radius $r \ll l$ is separated from the bubble. The minimum work done by turbulence to trigger such a separation process can be written as $\Delta p \frac{4}{3}\pi r^3 \alpha r + \frac{\sigma}{\rho} 4\pi r^2$, where Δp is the pressure gradient in turbulence and α is a constant as we defined in the section 4.1.2. In this case, the difference of the potential energy before and after the separation is limited. By connecting the work done for bubble fragmentation and turbulence energy, we obtain

$$\mathcal{N}_a^E(r) A_h dr (\Delta p \frac{4}{3}\pi r^3 \alpha r + \frac{\sigma}{\rho} 4\pi r^2) \propto |E(r^{-1}) dr^{-1}| A_h r \tag{4.14}$$

where $A_h = 4\pi l^2$ is the area of the initial bubble of radius l. Assume isotropic turbulence and Kolmogorov spectrum, equation (4.14) leads to the same two bubble size spectra described in equation (4.1) and (4.2). The diffidence is that g in equation (4.1) becomes Δp.

For a bubble of size l falling in the turbulence inertia range, but larger than the Hinze scale r_H, the fragmentation process is more complex. The bubble can be broken by turbulence structure of length scale $\sim l$, resulting in comparable sized daughter bubbles. Furthermore, during the fragmentation process, each daughter bubble also experience the similar fragmentation process, which could lead to complicated and

non-universal overall bubble size spectrum. At the same time, the separation of very small bubbles of size $r \ll l$ becomes the entrainment process again. r_H also plays a role in the fragmentation process by defining the smallest bubble size for fragmentation. For bubbles of size smaller than r_H, the fragmentation process is significantly suppressed.

4.2 Summary

In this section, we consider air entrainment in FST flows and propose a new model for entrainment bubble size spectrum $\mathcal{N}_a^E(r)$. The model is obtained by both a physical energy argument and a simple dimensional argument. In the energy argument, the energy for air entrainment is supplied by the energy of near-surface turbulence. The model predicts two regimes of $\mathcal{N}_a^E(r)$ depending on the bubble radius r. The two regimes are separated by the capillary length scale r_c. For water-air interface with earth gravity, r_c is a constant of $1.5mm$. For $r > r_c$, $\mathcal{N}_a^E(r)$ has a scaling of $\mathcal{N}_a^E(r) \propto g^{-1}\epsilon 2/3 r^{-10/3}$. For $r < r_c$, $\mathcal{N}_a^E(r)$ has a scaling of $\mathcal{N}_a^E(r) \propto (\sigma/\rho)^{-1}\epsilon 2/3 r^{-4/3}$. This model is compared with the measurements of bubble size spectrum inside breaking waves in the literature. The two power-laws of $\mathcal{N}_a^E(r)$ and the transition scale predicted by the new model agree well the the existing data. The physics of bubble fragmentation and its potential influences on the bubble size distribution are further discussed.

Inspired by the diagram of (L,q)-plane in Brocchini & Peregrine (2001*a*), we derive a lower r_l and upper bound r_u of the entrainment bubble size by considering the stabilizing effects of gravity and surface tension against the free-surface disturbance due to turbulence,. We plot r_l and r_u in a diagram of (r, ϵ)-plane analogous to the diagram of (L,q)-plane by Brocchini & Peregrine (2001*a*). r_l and r_u cross at (r_c, ϵ_c), where ϵ_c is a critical turbulence dissipation rate for bubble entrainment. For $\epsilon > \epsilon_c$, the disrupting effects of free-surface turbulence (FST) on the interface are strong relative to the stabilizing effects of g and σ/ρ. This is the regime of SFST with substantial air entrainment. For $\epsilon < \epsilon_c$, air entrainment is significantly suppressed by

either g or σ/ρ, resulting in a regime of weak FST (WFST). The regime of WFST can be further divided into three different regimes that correspond to dominant g, σ/ρ, and both. .

Chapter 5

DNS of air entrainment in SFST

In Chapter 4, a new model for bubble size spectrum $\mathcal{N}_a^E(r)$ of FST entrainment is developed. $\mathcal{N}_a^E(r)$ represents the specific bubble size spectrum resulted by SFST driven entrainment only. The actual bubble size spectrum in the bulk, $N_a(r)$, is also influenced by other physical processes such as fragmentation and degassing. The model predicts two regimes of $\mathcal{N}_a^E(r)$ depending on the bubble radius r. The scale separating the two regimes is the capillary length scale r_c. For $r > r_c$, bubble entrainment in SFST is under strong gravity effect and $\mathcal{N}_a^E(r)$ shows a scaling law $\mathcal{N}_a^E(r) \propto g^{-1}\epsilon^{2/3}r^{-10/3}$. For $r < r_c$, surface tension becomes more important in bubble entrainment and $\mathcal{N}_a^E(r)$ shows another scaling law $\mathcal{N}_a^E(r) \propto (\sigma/\rho)^{-1}\epsilon^{2/3}r^{-4/3}$. In this Chapter, we perform DNS of the canonical FST flow in Chapter 3 ,and provide DNS evidences and supports to our new theoretical model. In fact, $\mathcal{N}_a^E(r)$ is difficult to be directly measured. To obtain $\mathcal{N}_a^E(r)$, $N_a(r)$ needs to be measured before significant bubble fragmentation and degassing happen, to be precise. Then $\mathcal{N}_a^E(r)$ can be obtained by normalizing $N_a(r)$ using the area of the initial flat free surface. In fact, entrainment in SFST always accompanies with significant bubble fragmentation. Even though, the measured $N_a(r)$ is still helpful to imply $\mathcal{N}_a^E(r)$ and to understand its behaviors.

In this section, we first study the dependence of SFST entrainment on g by varying Fr for some sufficiently large We where surface tension effects are small. Both the averaged entrainment rate $\overline{Q}_{\mathcal{E}}$ and the magnitude of averaged increase rate of $N_a(r)$,

$\overline{Q}_{\mathcal{N}}(r)$, show a linear dependence on Fr^2 or g^{-1}. We then investigate the dependence of entrainment on σ by varying We for a (relatively large) fixed value of Fr where gravity effects become small. $\overline{Q}_{\mathcal{E}}$ and $\overline{Q}_{\mathcal{N}}(r)$, show a linear dependence on We or $(\sigma/\rho)^{-1}$. We next study the influence of near-surface dissipation ϵ, which measures the turbulence disrupting effect on the free surface, on SFST entrainment. The DNS results show that both the entrainment rate and the magnitude of increase rate of $N_a(r)$ scale as $\epsilon^{2/3}$. Next, we perform a very high-resolution DNS to verify our model predictions on the two-power laws of $\mathcal{N}_a^E(r)$ and the separating scale. The numerical results confirms the new model mainly on three aspects: 1) the power-law for large r regime is $\mathcal{N}_a^E(r) \propto r^{-10/3}$; 2) the power-law for small r regime is $\mathcal{N}_a^E(r) \propto r^{-4/3}$; 3) the separating scale is the capillary length scale instead of the Hinze scale.

In the final part of this section, the results of several DNS cases are analyzed and the corresponding data points are marked on the diagram of (r, ϵ)-plane. All the cases with/without air entrainment correctly fall in the regime of strong/weak free-surface turbulence regime.

5.1 Dependence of air entrainment on Fr

In FST flows, air entrainment is a consequence of two competing effects on the free surface. One is the disturbance effect of near-surface turbulence, which deforms the free surface and entrains air. The other is the stabilization effect due to gravity and surface tension, both of which stabilize the free surface and prevent air entrainment. Therefore, the two main parameters controlling air entrainment in FST are Fr and We. Notice that the stabilization effect of gravity and surface tension on the free surface are effective at different length scales (see detailed analysis in appendix C. In general, the air entrainment volume is affected by both Fr and We. To elucidate the underlying physics, we focus on the dependence of air entrainment on each of the two parameters independently by varying Fr for some sufficiently large We where surface tension effects are small; and varying We for a (relatively large) fixed value of Fr where gravity effects become small. For quantitative practical interest, it would be

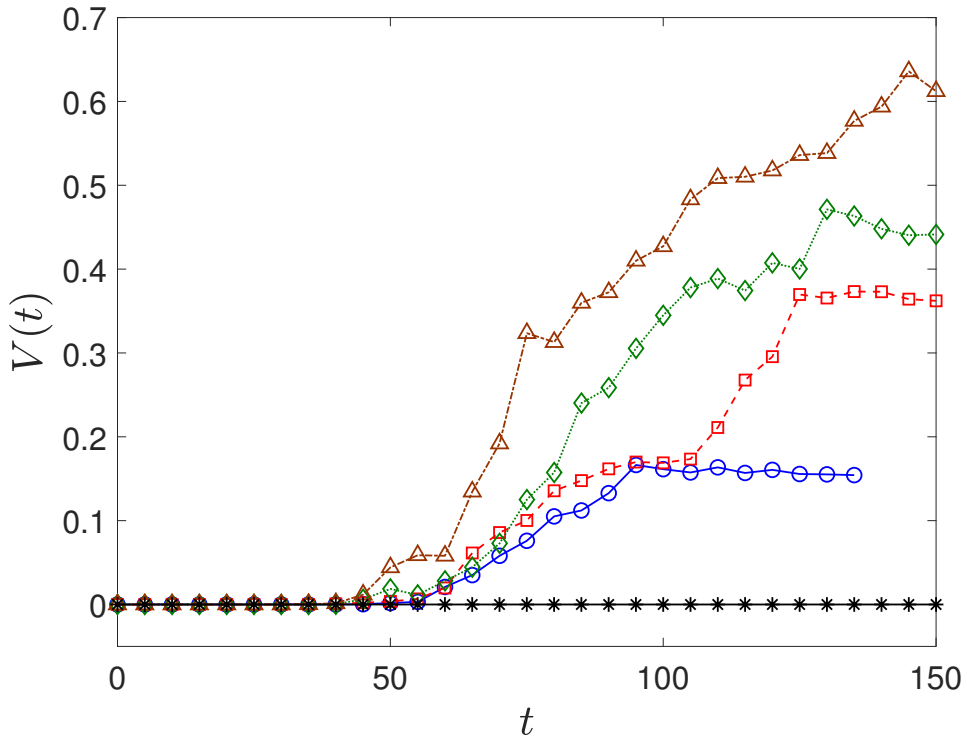

Figure 5-1: Time evolution of total entrainment volume $V(t)$ at different Fr with $We = \infty$ ($*$, $Fr^2 = 3$; $\circ$, $Fr^2 = 8$; $\square$, $Fr^2 = 10$; $\Diamond$, $Fr^2 = 12$; $\triangle$, $Fr^2 = 14$).

necessary to cover a more significant portion of the Fr-We parameter space. This is beyond the scope of this work.

To investigate the effect of Fr on air entrainment, we vary Fr ($Fr^2 = 3, 8, 10, 12,$ and 14) while maintaining negligible surface tension by choosing $We = \infty$. Figure 5-1 shows the time evolution of the total entrainment volume $V(t)$ for a range of Fr. From these results, we find a critical Fr_{cr} below which no air is entrained. For this particular flow with $We = \infty$, $Fr_{cr}^2 \approx 5$. The existence of Fr_{cr} confirms the stabilization effect of gravity. For $Fr < Fr_{cr}$, gravity stabilizes the free surface and prevents air entrainment.

Figure 5-1 shows a clear relationship between $V(t)$ and Fr for $Fr > Fr_{cr}$. Figure 5-2 shows the average entrainment rate $\overline{Q}_{\mathcal{E}}$ as a function of Fr^2 (with $We = \infty$), establishing a linear dependence of $\overline{Q}_{\mathcal{E}}$ on Fr^2 (or g^{-1}). Figure 5-3 shows the bubble size spectrum $N_a(r)$ for the varying Fr cases at the end of the entrainment period.

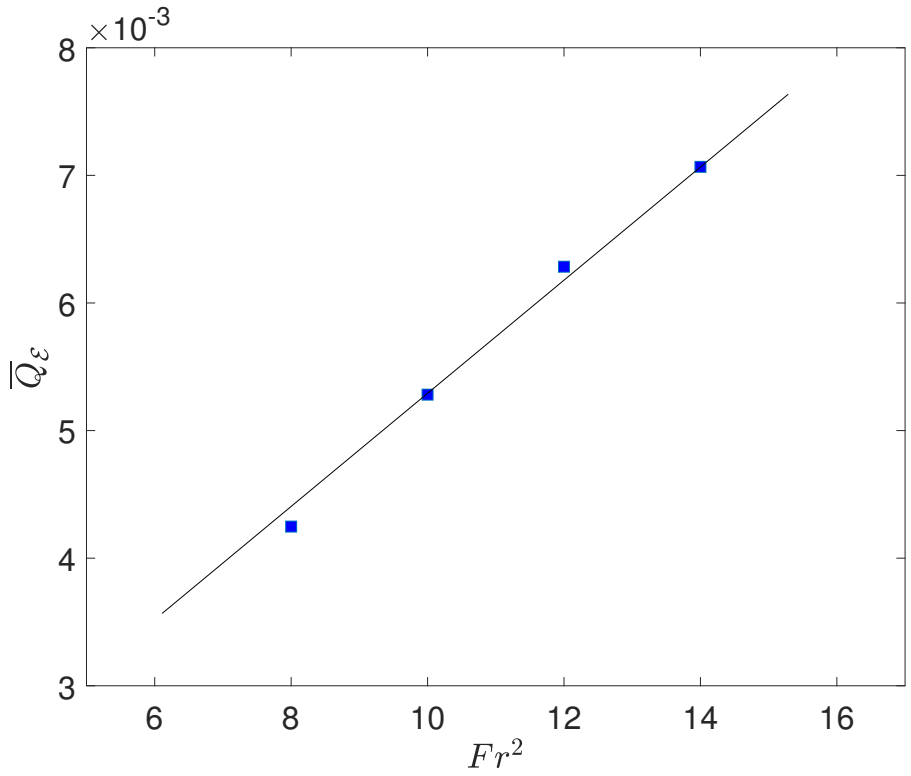

Figure 5-2: Average entrainment rate $\overline{Q}_{\mathcal{E}}$ as a function of Fr^2 with $We = \infty$. —— linear fit.

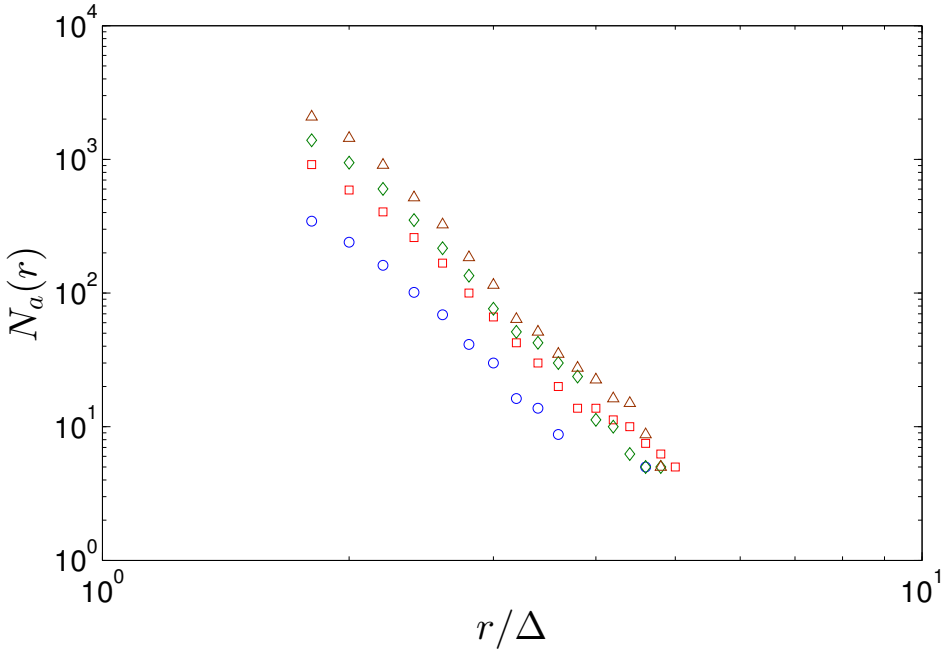

(a)

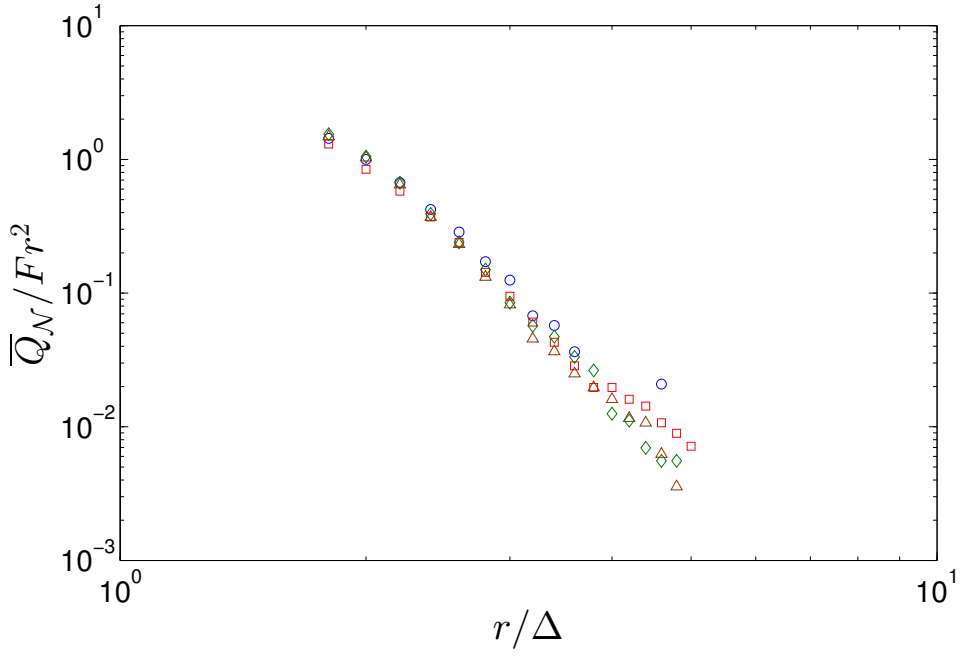

(b)

Figure 5-3: (a) Bubble size spectrum $N_a(r)$ at the end of the entrainment period $t = 125$ and (b) average rate of increase of bubble spectrum $\overline{Q}_{\mathcal{N}}(r)$ of different Fr with $We = \infty$ (○, $Fr^2 = 8$; □, $Fr^2 = 10$; ◇, $Fr^2 = 12$; △, $Fr^2 = 14$).

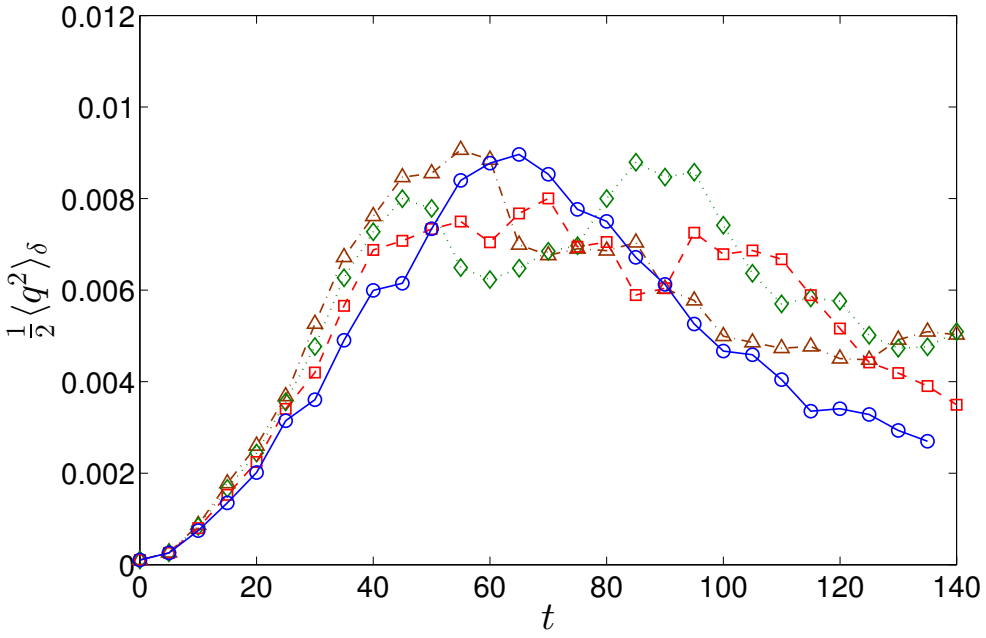

(a)

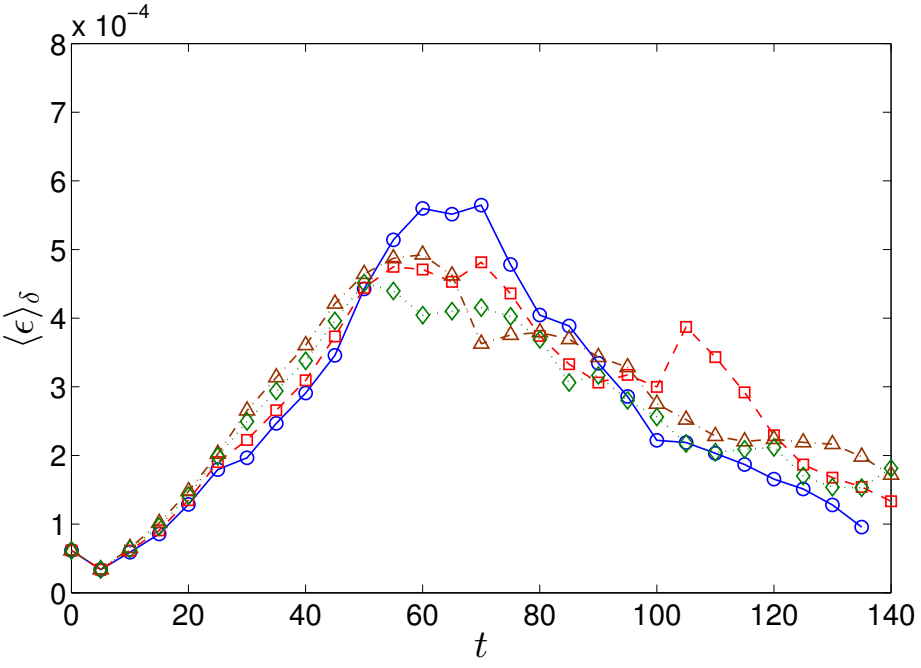

(b)

Figure 5-4: Time evolution of (a) turbulent kinetic energy near the free surface $\frac{1}{2}\langle q^2\rangle_\delta$ and (b) turbulent dissipation near the free surface $\langle\epsilon\rangle_\delta$ at different Fr with $We = \infty$. ($\circ$, $Fr^2 = 8$; $\square$, $Fr^2 = 10$; $\Diamond$, $Fr^2 = 12$; $\triangle$, $Fr^2 = 14$).

The results in figure 5-3(a) suggest an increase in the overall number of entrained bubbles with increasing Fr. Figure 5-3(b) shows the average rate of increase of bubble spectrum scaled by Fr^2, $\overline{Q}_{\mathcal{N}}(r)/Fr^2$, resulting in a collapse of the data. This further confirms the linear dependence of air entrainment rate on Fr^2.

The four Fr considered in figure 5-1 fall within the strong turbulence regime and their basic features are the same as discussed in §3.2. Figure 5-4 shows the evolution of the near-surface turbulent kinetic energy $\frac{1}{2}\langle q^2\rangle_\delta$ (figure 5-4(a)) and turbulent dissipation rate $\langle\epsilon\rangle_\delta$ (figure 5-4(b)). $\langle\epsilon\rangle_\delta$ is defined as $\frac{1}{Re}\langle\frac{\partial u_i}{\partial x_k}\frac{\partial u_i}{\partial x_k}\rangle_\delta$. Despite the sizeable variation of Fr, the effect of Fr on the available near-surface turbulence energy is limited. Thus the observed dependence of $\overline{Q}_{\mathcal{E}}$ on Fr^2 is primarily a result of the change of the gravity effects on the air-water interface (through the stabilization on the free surface).

5.2 Dependence of air entrainment on We

To investigate the effect of We on air entrainment, we vary We (We=100, 1000, 4000, 10000, 15000 and 50000) while maintaining $Fr^2 = 10$. Our interest here is for FST with sufficiently large Fr ($Fr^2 = O(10)$) where SFST and air entrainment occur. Figure 5-5 shows the time evolution of the total entrainment volume $V(t)$ for a range of We. From these results, we also find a critical We_{cr}, below which air entrainment is suppressed. For this particular flow with Fr^2=10, We_{cr} is found to be of $O(100)$. Figure 5-5 shows a clear relationship between $V(t)$ and We for $We > We_{cr}$. Figure 5-6 shows the average entrainment rate $\overline{Q}_{\mathcal{E}}$ as a function of We with given $Fr^2 = 10$. In figure 5-6, the dependence of $\overline{Q}_{\mathcal{E}}$ on We shows two regimes. For $We \gtrsim O(W_{e1})$, $\overline{Q}_{\mathcal{E}}$ converges to the value of the case with $We = \infty$. For $We \lesssim O(W_{e1}) = O(3\times10^4)$, $\overline{Q}_{\mathcal{E}}$ is observed to be linearly dependent on We. We argue that the two regimes correspond to important or unimportant surface tension relative to gravity, delineated by $Bo_r = \rho g l_c^2/\sigma \approx 1$ with the capillary length scale l_c being a characteristic length scale of bubble size of order Δ. For $We \gtrsim O(W_{e1})$, l_c is $\lesssim \Delta$ and the effects of surface tension on scales we resolve in DNS are negligible

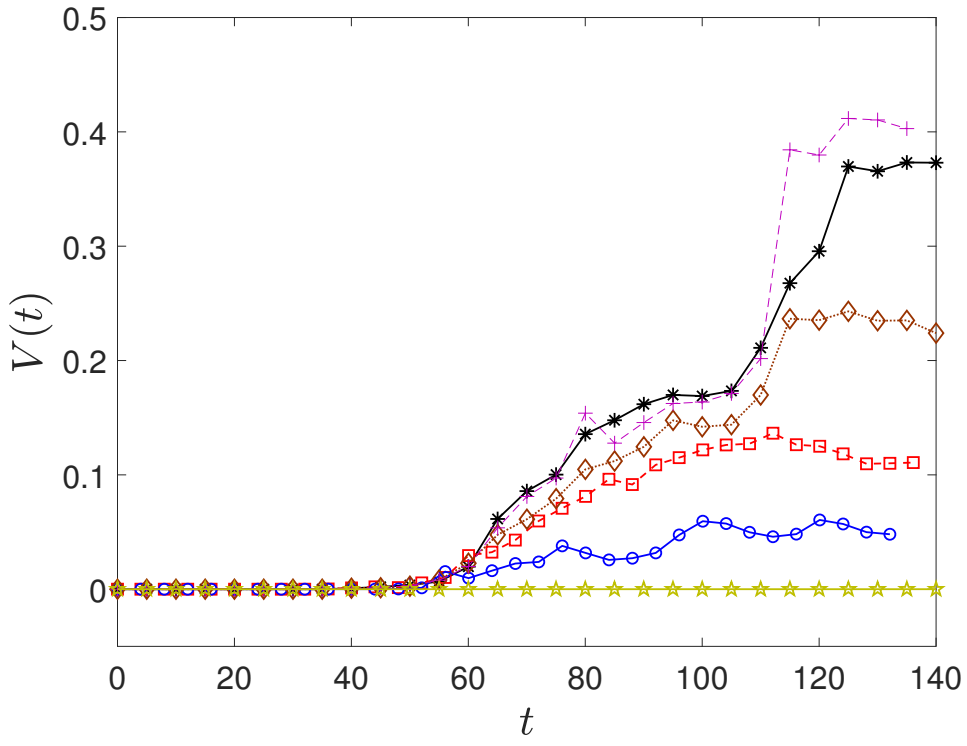

Figure 5-5: Time evolution of total entrainment volume $V(t)$ at different We with $Fr^2 = 10$ ($\triangle$, $We = 100$; $\circ$, $We = 1000$; $\square$, $We = 4000$; $\Diamond$, $We = 10000$; $+$, $We = 50000$; $*$, $We = \infty$.)

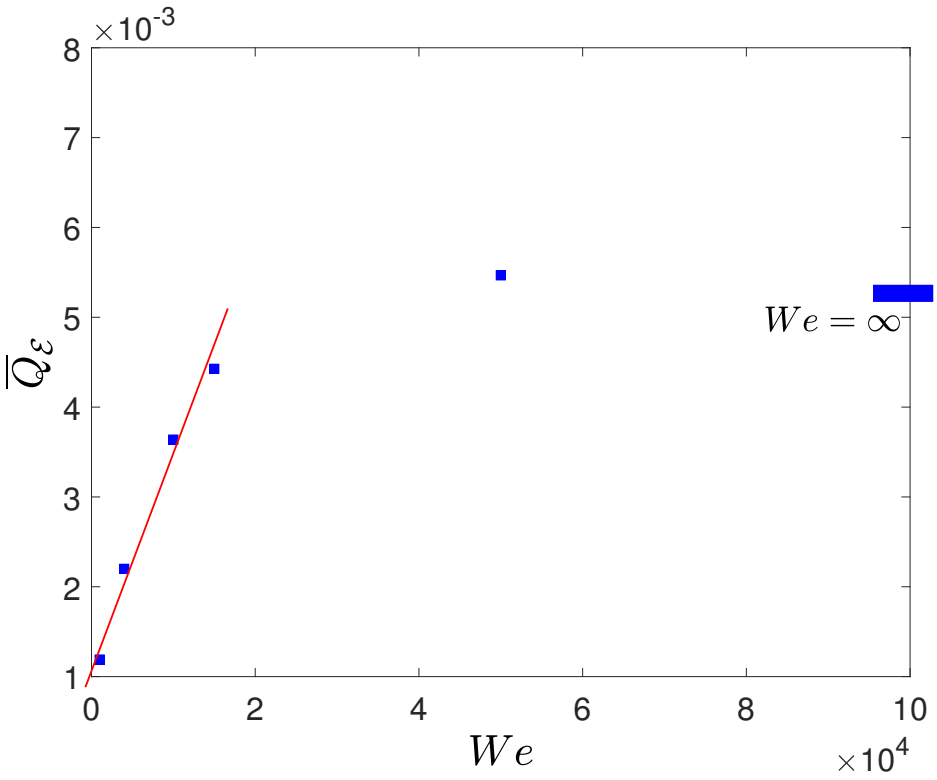

Figure 5-6: Average entrainment rate $\overline{Q}_{\mathcal{E}}$ as a function of We with $Fr^2 = 10$. — linear fit.

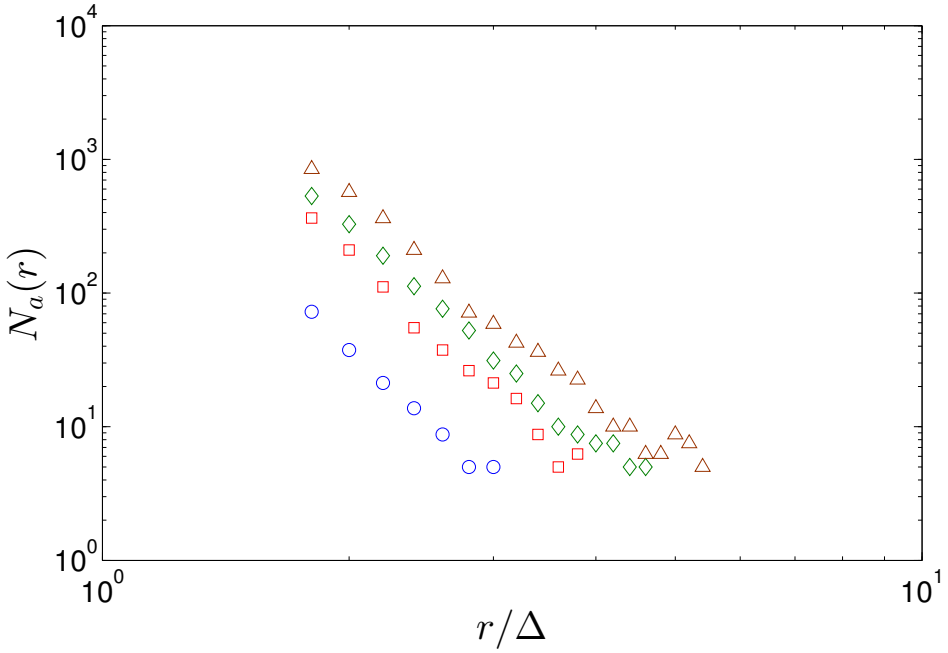

(a)

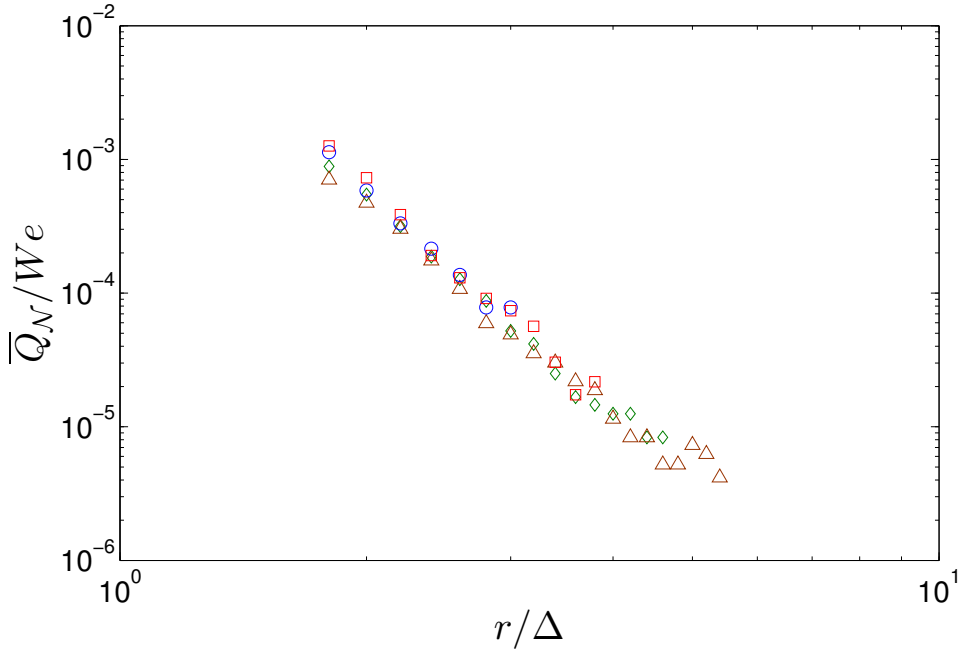

(b)

Figure 5-7: (a) Bubble size spectrum $N_a(r)$ at the end of the entrainment period $t = 125$ (b) average rate of increase of bubble spectrum $\overline{Q}_{\mathcal{N}}(r)$ of different We with $Fr^2 = 10$ (○, $We = 1000$; □, $We = 4000$; ◇, $We = 10000$; △, $We = 15000$)

relative to gravity. In figure 5-6, $\overline{Q}_{\mathcal{E}}$ at $We = 5 \times 10^4$ is observed to be close to the value at $We = \infty$. Therefore, rather than fixing some $We > O(W_{e1})$, we can use $We = \infty$ to approximate the cases where surface tension effects are negligible (and Fr is the controlling parameter for bubble entrainment). For $We \lesssim O(W_{e1})$, l_c is comparable to entrainment scales we resolve and surface tension becomes important on air entrainment. For the four cases with $We = 1000, 4000, 10000, 15000$ in figure 5-6, l_c is resolved by at least one grid. For the case of $We = 1000$ with strongest surface tension of all the cases, l_c is resolved by four grids. The corresponding $\overline{Q}_{\mathcal{E}}$ is observed to be linearly dependent on We (or $(\sigma/\rho)^{-1}$).

Another relevant parameter for bubble entrainment is $We_T = \rho\langle q^2\rangle_\delta \ell_t/\sigma$, where $\langle q^2\rangle_\delta$ represents the turbulent kinetic energy near the free surface (see figure 5-8 (a)). The length scale, $\ell_t = (\langle q^2\rangle_\delta We)^{-1}$ for $We_T = 1$, represents the scale of capillary surface deformation introduced by turbulence. To simulate the entrainment under strong surface tension, we need to have ℓ_t being resolved or $\ell_t \gtrsim O(\Delta)$. Equivalently, we need $We \lesssim O(10^4)$. For the four cases with $We = 1000, 4000, 10000, 15000$, the surface tension effects on the entrainment process are important and being properly resolved.

We point out that the transition of the two regimes observed in figure 5-6 corresponds to $Bo_r \sim 1$ instead of $We_T \sim 1$. As pointed out early, air entrainment in FST is a consequence of the competition of the disturbance effect of near-surface turbulence and the stabilization effect from gravity and surface tension. Bo_r represents the gravity effect compared to surface tension. $Bo_r \sim 1$, thus, suggests the transition of dominance of surface tension or gravity. At $Bo_r \sim 1$, the main stabilization force on the free surface is shifted from surface tension to gravity, which suggests a mechanism change of the stabilization force competing with turbulence disturbance. Since gravity does not change with fixed Fr, the convergence of $\overline{Q}_{\mathcal{E}}$ after the transition in figure 5-6 is because of the unchanged gravity effects with negligible surface tension. On the other hand, We_T represents the disrupting effect of near-surface turbulence compared to the stabilizing effect of surface tension. $We_T \sim 1$ does not suggest significant changes in the underlying mechanism.

For the $We \lesssim O(W_{e1})$ cases of interest, figure 5-7 shows the bubble size spectrum $N_a(r)$ at the end of the entrainment period. Figure 5-7(a) suggests the number of entrained bubbles increases as We increases. Figure 5-7(b) shows $\overline{Q}_{\mathcal{N}}(r)/We$ for the varying We cases. The collapse of $\overline{Q}_{\mathcal{N}}(r)/We$ supports the linear dependence of the entrainment rate on We.

For these four cases, $\overline{Q}_{\mathcal{E}}$ is believed to be accurate as l_c and ℓ_t are resolved in our DNS. For $N_a(r)$, however, the resolution of bubble shape (and surface tension forces) requires $r/\Delta \gtrsim 4$. Thus the predictive range of DNS in figure 5-7 is very limited by the DNS resolution, although figure 5-7(b) does show meaningful collapse of the results with the proposed We^{-1} scaling. Extension of figure 5-7 over a broader size range can in theory be achieved by increasing the DNS resolution, but the computational effort rapidly becomes prohibitive.

The four flows are in the strong turbulence regime (SFST). Figure 5-8 shows the evolution of the turbulent kinetic energy $\frac{1}{2}\langle q^2 \rangle_\delta$ and turbulent dissipation rate $\langle \epsilon \rangle_\delta$ in the near surface region. Despite the sizeable variation of We, the available energy of near-surface turbulence remains unaffected. Thus the observed dependence of $\overline{Q}_{\mathcal{E}}/\overline{Q}_{\mathcal{N}}(r)$ on We is primarily a result of the variation of surface tension on the air-water interface (through the stabilization on the free surface).

5.3 Dependence of air entrainment on turbulence dissipation

To obtain FST flows with near-surface turbulence of different dissipation, we vary the magnitude of the initial velocity profile of the shear flow in (3.1).

$$u(z, t = 0) = U_a(1 - 0.9988 sech^2(0.88137z)) \tag{5.1}$$

Here we we consider four values of $U_a = 0.9, 1.0, 1, 1$ and 1.2 (call flow 1, flow 2, flow 3, and flow 4, respectively) to generate turbulence of different dissipation rate.

Figure 5-9 shows the evolution of turbulence dissipation near the free surface $\langle \epsilon \rangle_\delta$

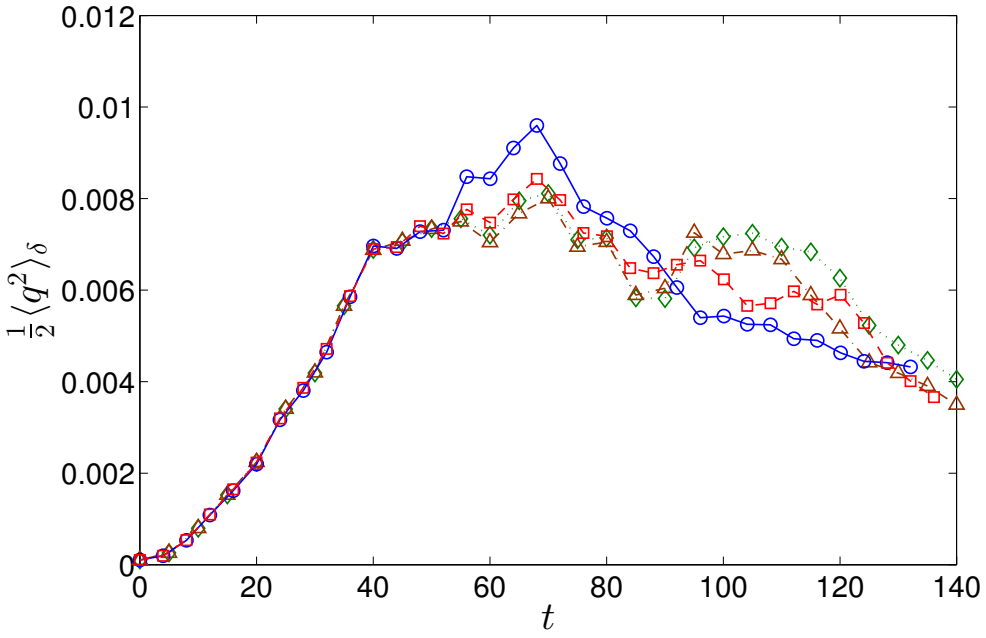

(a)

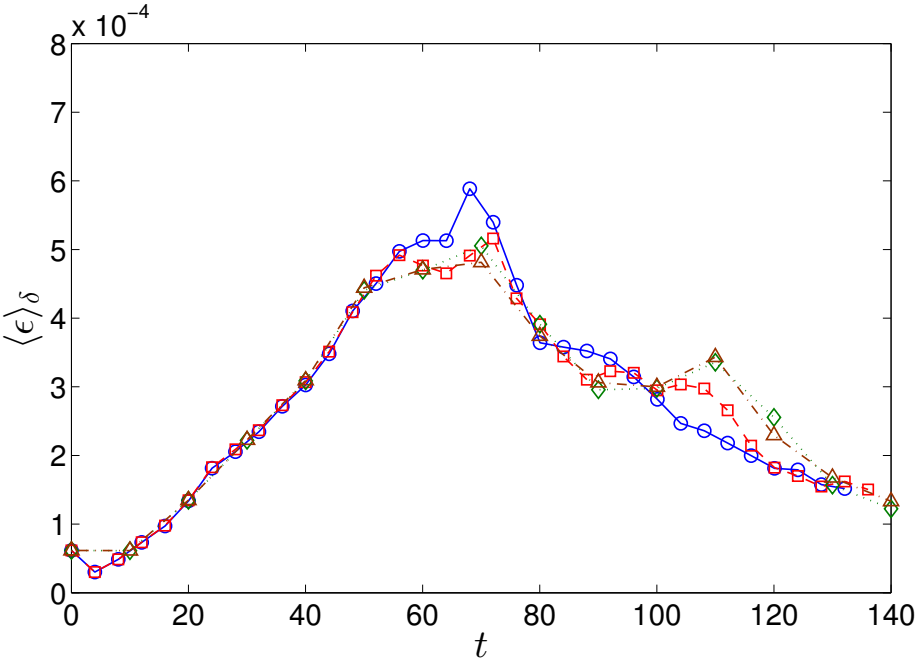

(b)

Figure 5-8: Time evolution of (a) turbulent kinetic energy near the free surface $\frac{1}{2}\langle q^2\rangle_\delta$ and (b) turbulent dissipation near the free surface $\langle\epsilon\rangle_\delta$ at different We with $Fr^2 = 10$. ($\circ$, $We = 1000$; $\square$, $We = 4000$; $\Diamond$, $We = 10000$; $\triangle$, $We = \infty$)

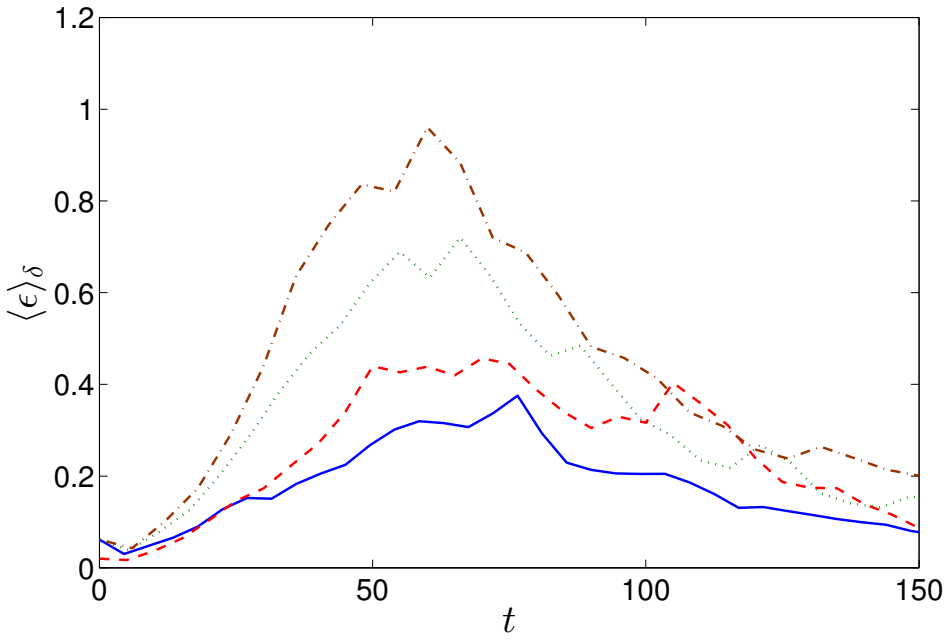

Figure 5-9: Time evolution of turbulent dissipation near the free surface $\langle\epsilon\rangle_\delta$ at $Fr^2 = 10$ and $We = \infty$. ——, flow 1 with $U_a = 0.9$; - - -, flow 2 with $U_a = 1.0$; · · ·, flow 3 with $U_a = 1.1$; — · —, flow 4 with $U_a = 1.2$.

in the four flows. Turbulence dissipation reflects the strength of turbulence. We notice that the evolutions of turbulence in the four flows show similar trend. Initially, turbulence near the free surface grows as the beneath shear flow supplies energy. Later on, the shear flow profile flattens due to diffusion (Tsai, 1998; Shen *et al.*, 1999), resulting in the decrease of turbulent production. At late time, turbulence production significantly reduces so that no enough energy is supplied to turbulence. Turbulence, thus, is observed to decay. In addition, it is noticed that turbulence in these four flows shows different levels of dissipation rate. Flow 4 with the largest U_a has strongest turbulence dissipation, while flow 1 with smallest U_a has least. Larger U_a results in larger turbulence production in the bulk flow as shown in figure 5-10, which leads to stronger turbulence.

Figure 5-11 plots the evolutions of the total entrainment volume $V(t)$ in the four flows. It clearly shows that flow 4 with strongest turbulence leads to largest V. The results suggest a positive correlation of entrainment and turbulence dissipation. We define $T_a = t_e - t_a$ as the entrainment duration as usual, where t_a and t_e are the start

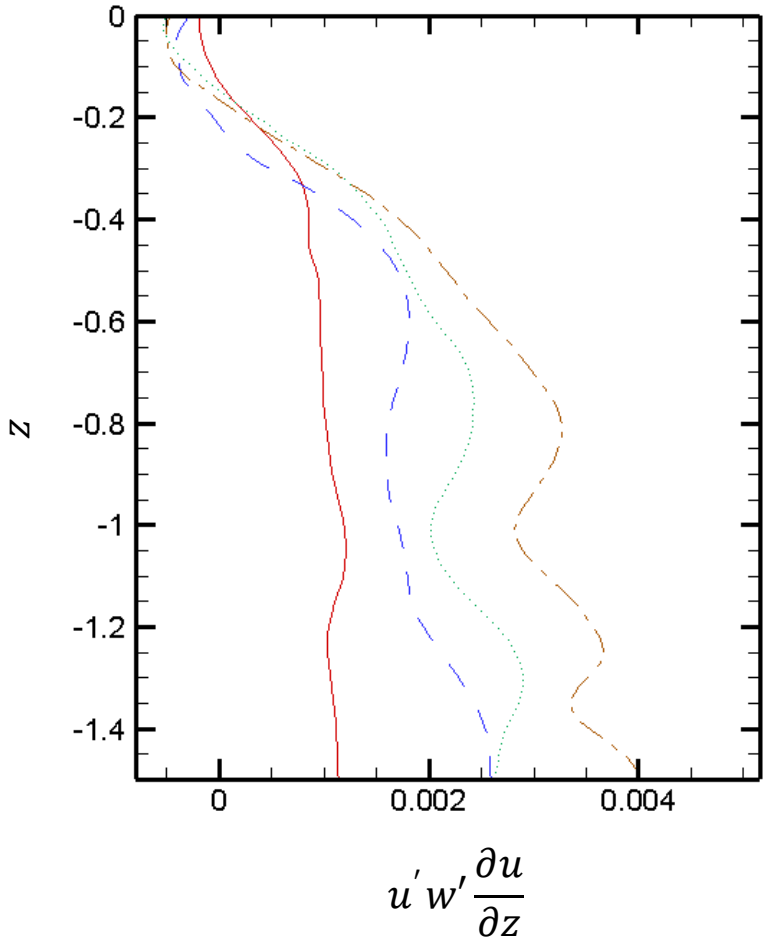

Figure 5-10: Vertical profile of turbulence production term $u'w'\frac{\partial \bar{u}}{\partial z}$ at $Fr^2 = 10$ and $We = \infty$. ——, flow 1 with $U_a = 0.9$; - - -, flow 2 with $U_a = 1.0$; · · ·, flow 3 with $U_a = 1.1$; — · —, flow 4 with $U_a = 1.2$.

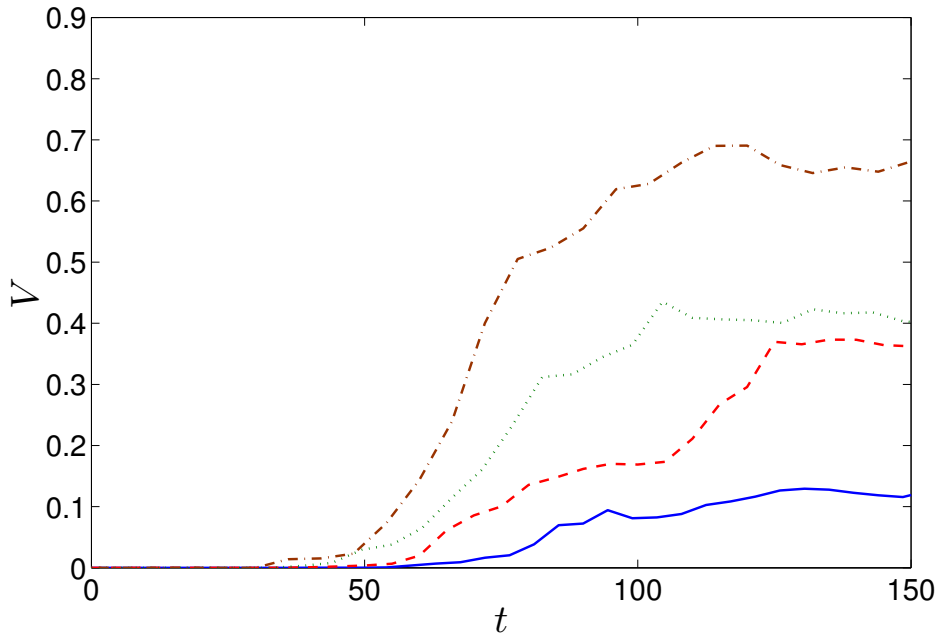

Figure 5-11: Time evolution of entrainment volume $V(t)$ at $Fr^2 = 10$ and $We = \infty$. ——, flow 1 with $U_a = 0.9$; - - -, flow 2 with $U_a = 1.0$; · · ·, flow 3 with $U_a = 1.1$; — · —, flow 4 with $U_a = 1.2$.

and end of the entrainment process. During the entrainment period from t_a to t_e, the average rate of air entrainment remains mostly positive and the entrainment process is assumed to be dominant over degassing. During the entrainment process, turbulence intensity (or turbulence dissipation $\langle\epsilon\rangle_\delta$) is observed to remain in a high level. After the period, the entrainment process ends and the degassing process becomes dominant due to the significant decay of turbulence. The entrained air bubbles start to escape from the water under the buoyancy effect.

According to our model, we have $\mathcal{N}_a^E(r) \propto \epsilon(t)^{2/3}$, which further implies that:

$$\frac{1}{T}\int_{t_a}^{t}\int_{r}\mathcal{N}_a^E(r)(r,\tau)drd\tau \propto \frac{1}{T}\int_{t_a}^{t}\epsilon(\tau)^{2/3}d\tau \tag{5.2}$$

where $T = t - t_a$. We notice that the integral $\int_{t_a}^{t}\int_{r} N(r,\tau)drd\tau$ in the left-hand side of equation (5.2) is the total entrainment volume $V(t)$ at time t. The right-hand side is the time average of $\epsilon(t)^{2/3}$. We consider different t in each of the four flows and plot $V(t)/T$ (left-hand side of equation (5.2)) as a function of $\frac{1}{T}\int_{t_a}^{t_e}\epsilon(\tau)^{2/3}d\tau$ (right-hand

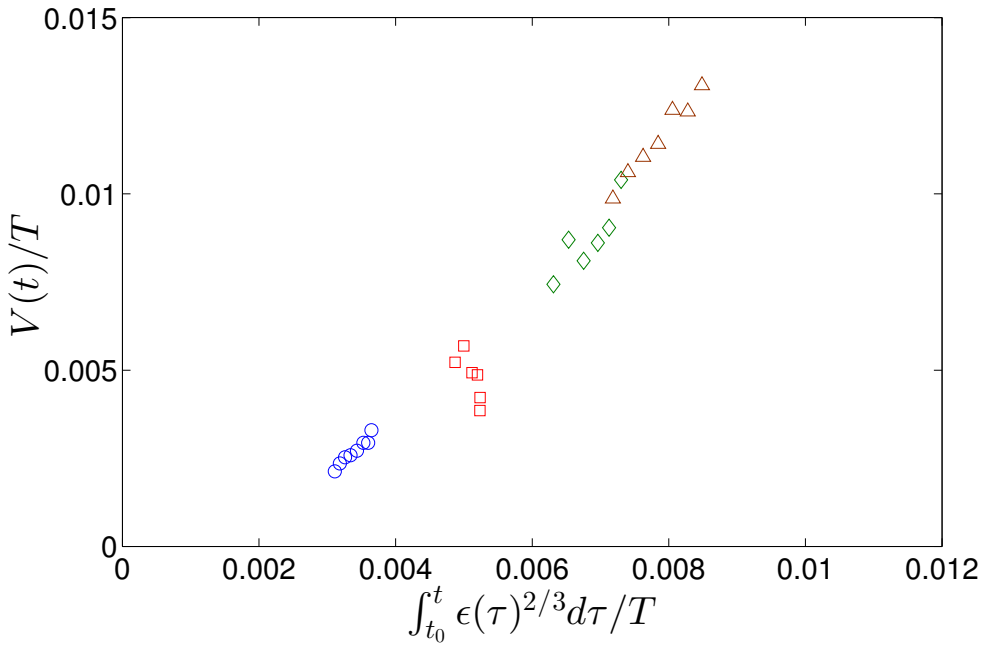

Figure 5-12: $V(t)/T$, where $T = t - t_a$, as a function of $\frac{1}{T}\int_{t_a}^{t} \epsilon(\tau)^{2/3} d\tau$ at $Fr^2 = 10$ and $We = \infty$. ○, flow 1 with $U_a = 0.9$; □, flow 2 with $U_a = 1.0$; ◇, flow 3 with $U_a = 1.1$; △, flow 4 with $U_a = 1.2$.

side of equation (5.2)) in figure 5-12. All the data is observed to lie around a straight line, which suggests a linear relationship of the two plotted quantities and confirms the description of equation (5.2).

We then consider the bubble size spectrum in the bulk flow $N_a(r,t)$ at time t. Figure 5-13(a) shows $N_a(r)$ at $t = t_e$ for the four flows. We notice that the flow with stronger turbulence has more bubbles entrained. As $N_a(r)$ is scaled by $\int_{t_a}^{t_e} \epsilon(\tau)^{2/3} d\tau$ which measures the averaged turbulence dissipation during the entrainment period, all the plots overlap with each other as shown in figure 5-13(b), suggesting the scaling $N_a(r) \propto \epsilon^{2/3}$. Different than $\mathcal{N}_a^E(r)$, $N_a(r)$ is a result of multiple physical processes including entrainment, bubble fragmentation and degassing. As a consequence, the exact power-law slopes of the two spectra might not be same. However, the relative amplitudes and relevant scale dependence obtained from $N_a(r)$ is expected to apply to $\mathcal{N}_a^E(r)$ as well.

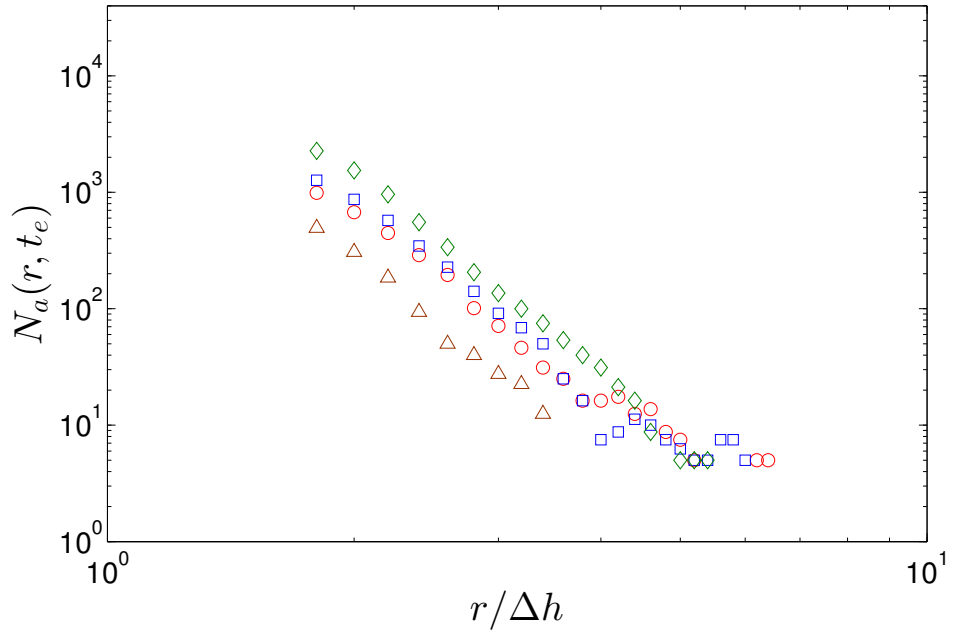

(a)

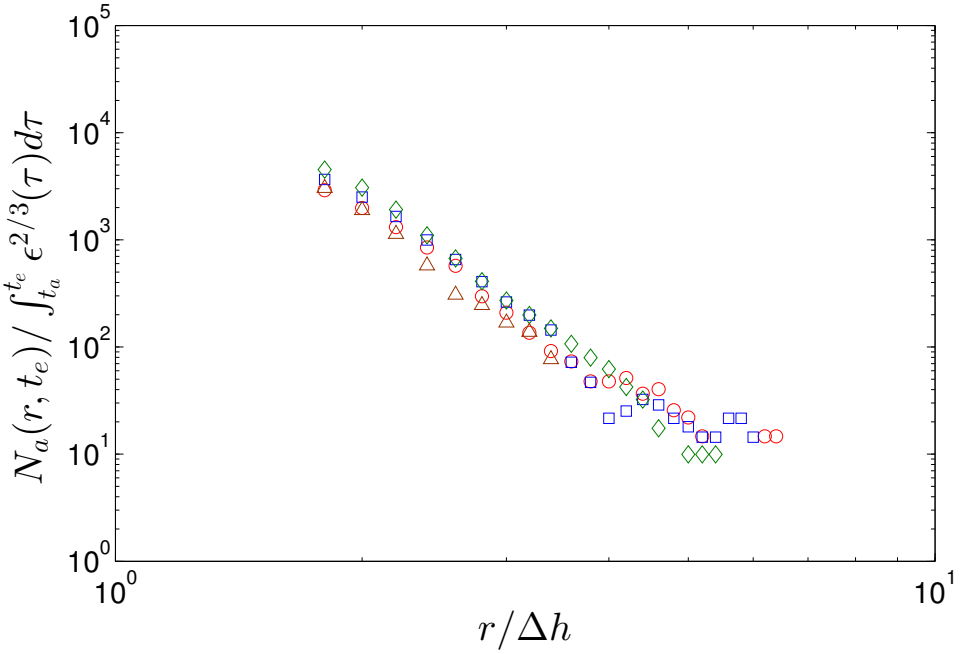

(b)

Figure 5-13: (a) Size spectrum of entrained bubbles $N_a(r,t_e)$ at time t_e (b) Size spectrum of entrained bubbles $N_a(r,t_e)$ at time t_e scaled by $\int_{t_a}^{t_e}\epsilon(\tau)^{2/3}d\tau$ at $Fr^2=10$, $We=\infty$ and $Re=1000$. $\circ$, flow 1 with $U_a=0.9$; $\square$, flow 2 with $U_a=1.0$; $\diamond$, flow 3 with $U_a=1.1$; $\triangle$, flow 4 with $U_a=1.2$.

5.4 Power-law regimes of bubble size spectrum

In this section, we perform DNS of a similar canonical problem in Chapter 3 but with a smaller domain and higher resolution. The domain size is 6^3. The horizontal dimension is approximately half of the original case where the domain size is 10.472. The magnitude of the initial mean velocity profile of the shear flow is 1.2 times larger than the original one to speed up the growth of turbulence near the free surface. In this DNS, we apply a higher resolution with 512^3 grids (three times more than the one used in Chapter 3) to better resolve the surface tension forces on the interface. The smallest bubble considered being properly resolved is of size resolved by 4 grids. In the current simulation, the Froude number square $Fr^2 = U^2/gL$ is 21 and the Weber number $We = \rho U^2 L/\sigma$ is 2100. The Reynolds number is 1,000. The information and the verification of the numerical solver is presented in previous chapter.

Figure 5-14 (a) shows the time evolution of turbulent dissipation near the free surface $\langle\epsilon\rangle_\delta$ of the flow, where $\langle\cdot\rangle_\delta$ is defined as the average over the "near free surface" region.The detailed definition and sensitivity analysis to the parameter δ are in Chapter 3. Figure 5-14 (b) shows the time evolution of the total entrainment volume V in the computational domain. An active entrainment period between $t_s = 45$ and $t_e = 56$ is observed. During this time period, the entrainment rate $Q(t) = \dot{V}(t)$ remains positive. The turbulence intensity or $\langle\epsilon\rangle_\delta$ remains large. Figure 5-15 shows the three one-dimensional energy spectra (calculated from velocity fluctuations at the free surface) at t=54 in the entrainment period. We observe all the three components have comparable magnitudes and follow the Kolmogorov spectra $k^{-5/3}$ of isotropic turbulence. This result verifies the assumption in the derivation of (4.9) that the energy spectrum of near-surface turbulence can be described using the Kolmogorov spectra. After $t = 56$, we observe a post entrainment period, where the entrainment volume starts to decrease and turbulence starts to decay. In this period, the entrainment process stops and the degassing process becomes the dominant process.

Figure 5-16 shows the bubble size spectrum $N_a(r)$ at different time instances during then entrainment period. The bubble radius r is normalized by the capillary

length scale r_c. Given $Fr^2 = 21$ and $We = 2100$, r_c at which $Bo = We/Fr^2(2r_c)^2 = 1$ is around 0.05. $N_a(r)$ in figure shows two clear regimes, separating by r_c. In the regime of $r > r_c$, $N_a(r)$ shows a power-law of $N_a(r) \propto r^{-10/3}$. In the regime of $r < r_c$, $N_a(r)$ shows a power-law close to $N_a(r) \propto r^{-4/3}$. In addition, turbulence dissipation in the current flow is of order $1e-3$ (see figure 5-14(a)). (4.10) suggests that the Hinze scale is r_H is around 0.13 with We_c being 4.7 (Deane & Stokes, 2002; Wang *et al.*, 2016). r_H is marked in the figure. In the current simulation, the critical scale separating the two bubble size regimes happens around r_c, but far away from r_H. These numerical results are consistent with our theory predictions in the previous section. Also most of the entrained bubbles in the current simulation are smaller than r_H, suggesting negligible bubble fragmentation. Thus, the two power-law of $N_a(r)$ during the entrainment period maintains. In addition, the averaged rate of bubble degassing is one order smaller than the averaged entrainment rate, indicating negligible degassing. Therefore, $N_a(r)$ in this case is equivalent to $\mathcal{N}_a^E(r)$. In the post-entrainment period, $N_a(r)$ at $t = 70$ is shown in the in the inset figure (a) of figure 5-16. During this time period, the entrainment process stops due to the decay of turbulence and bubble degassing becomes the dominant process. Under the effect of buoyancy, large bubbles escape from the water faster and the slope of $N_a(r)$ becomes steeper.

To further confirm that the transition scale of the two regimes of $N_a(r)$ does not change with turbulence dissipation, we perform a DNS of the same FST flow with a larger magnitude of the initial mean velocity profile of the shear flow. The corresponding governing parameters are $Fr^2 = 24.65$, $We = 2465$, and $Re = 1300$. The capillary length scale r_c remains the same with that in the previous DNS. The magnitude of near-surface turbulence dissipation $\langle\epsilon\rangle_\delta$ becomes 1.5 times larger. We show averaged $N_a(r)$ during the entrainment period in inset figure (b) of figure 5-16. It is observed that the magnitude of $N_a(r)$ increases as $\langle\epsilon\rangle_\delta$ increases. In addition, the transition of the two regimes of $N_a(r)$ still happens at r_c. This result provides an extra support that the transition scale of the two bubble size regimes is r_c instead of r_H which is a function of turbulence dissipation rate.

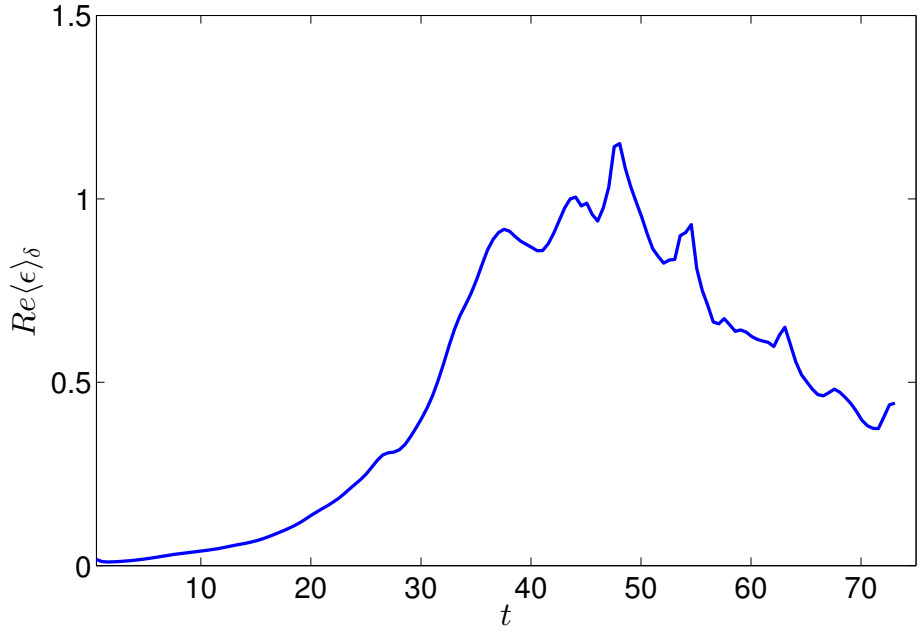

(a)

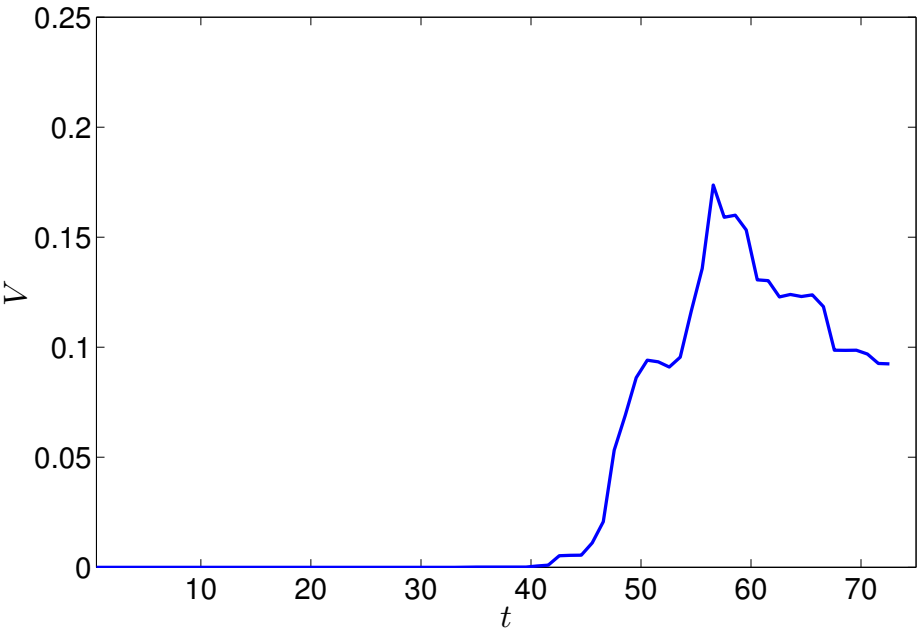

(b)

Figure 5-14: Time evolution of (a) turbulent dissipation near the free surface $\langle\epsilon\rangle_\delta$ and (b) total entrainment volume in the computational domain.

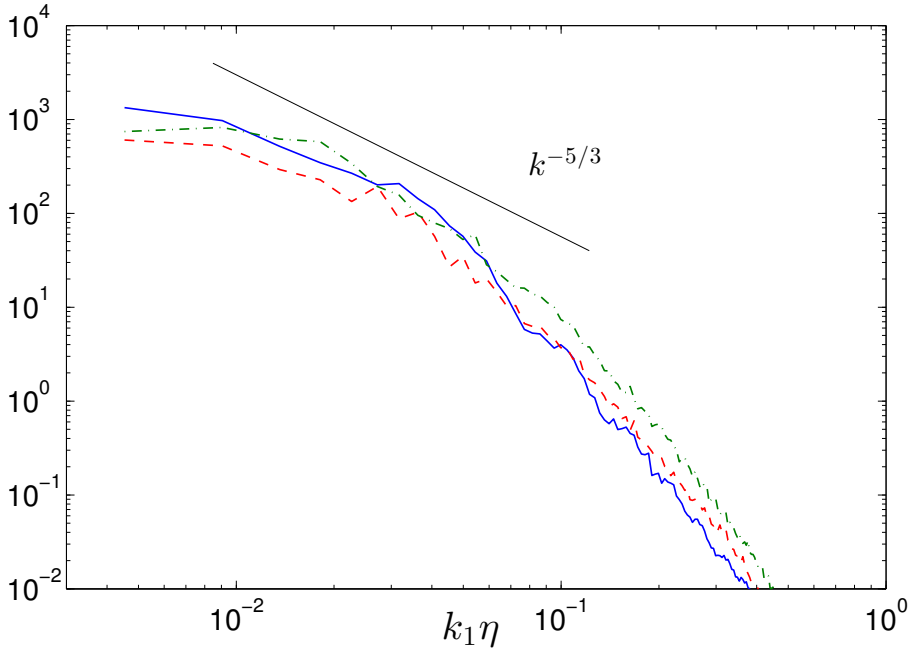

Figure 5-15: One-dimensional energy spectrum $E_{11}(k_1)$ (——), $E_{22}(k_1)$ (- - -), $E_{33}(k_1)$ (— · —) near the free surface at $t = 56$ in the DNS with $Fr^2 = 21$, $We = 2100$, and $Re = 1200$.

5.5 DNS data points on diagram of (r, ϵ)-plane

We mark the corresponding data point of the high-fidelity DNS case in §5.4 on the diagram of the (r, ϵ)-plane in figure 4-2. Given the earth gravity $g = 9.8m/s^2$ and the air-water surface tension $\sigma/\rho = 7.2 \times 10^{-5}m^3/s^2$, the flow characteristic length scale L, velocity scale U, and the effective ν of physical units in the DNS can be estimated based on the given values of Fr^2, We, and Re. Next, the range of entrainment bubble size and near-surface turbulence dissipation rate with physical units are determined. This DNS case is presented in the (r, ϵ)-plane using a solid line showing the size range of entrained bubbles. Notice that r_l and r_u in (4.11) and (4.12) are derived under the assumption of unbounded turbulence inertial range. In figure 5-17, the presented range of the entrainment bubble size is also lower bounded by Δ and upper bounded by L. This range of (Δ, L) is represented by the dash line. In the DNS, the smallest bubble considered being resolved is at least of radius larger than 3Δ. The largest bubble observed in the flow is always smaller than L. We observe that the current

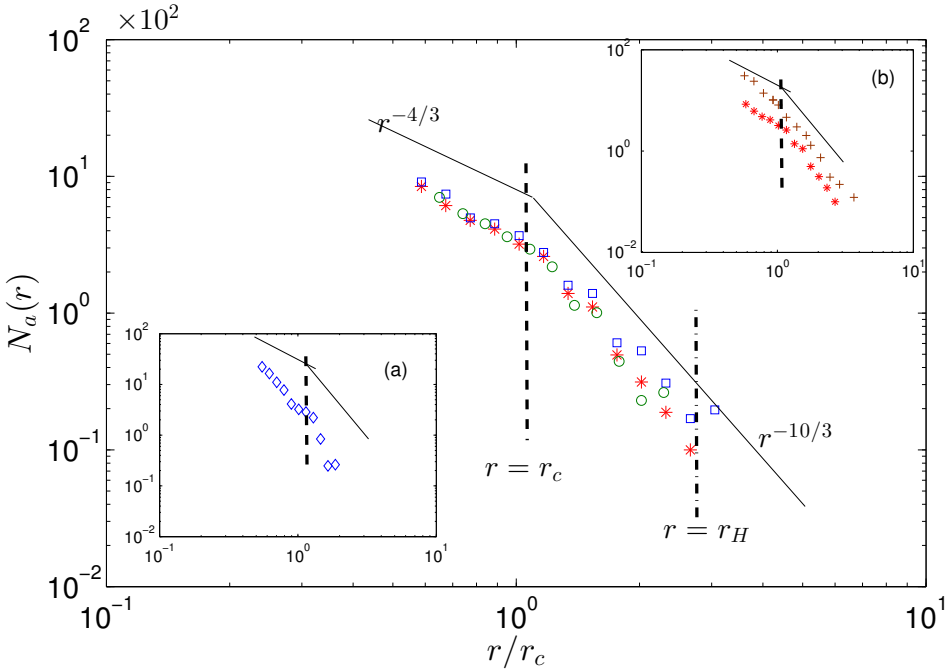

Figure 5-16: Bubble size spectrum $N_a(r)$ at different time instances during the active entrainment period of DNS with parameters $Fr^2 = 21$, $We = 2100$, and $Re = 1200$. ○, t=52; □, t=t_e=56 (end of the entrainment period), *, average between t=52 and t=56. r_c is the capillary length scale in (4.3). $r - H$ is the Hinze scale in (4.10). The two theoretical power-laws of $r^{-4/3}$ and $r^{-10/3}$ are represented by ——. Inset (a): $N_a(r)$ at t=70 in the post-entrainment period. Inset (b): averaged $N_a(r)$ during the entrainment period for the two DNS. *: DNS with parameters $Fr^2 = 21$, $We = 2100$, and $Re = 1200$; +: DNS with parameters $Fr^2 = 24.65$, $We = 2465$, and $Re = 1300$.

Table 5.1: Information of DNS of the canonical FST flow.

Fr^2	We	Re	$L(m)$	$U(m/s)$	$\nu(m^2/s)$	$\Delta(m)$	$\epsilon(m^2/s^3)$	data resource
21	2100	1200	0.027	2.4	5.3e-5	3.2e-4	0.4	§5.4
10	5e4	1000	0.19	4.3	8.3e-4	5.2e-3	0.21	§5.1
10	1000	1000	0.027	1.6	4.4e-5	7.4e-4	0.08	§5.2
0.5	5e4	1000	0.86	2.05	1.8e-3	0.023	0.005	§5.1

DNS is located in the region 2, where FST is strong (relative to g and σ) and air entrainment happens. With the same procedure, we add more data points from DNS in §5.1 and §5.2 to the (r, ϵ)-plane. Table 5.1 lists the detailed information of the DNS. The two cases with air entrainment are correctly fall in the region 2 as expected. The case of $Fr^2 = 0.5$, $We = 1e6$, and $Re = 1000$ with no air entrainment is in the region 3. For the length scale considered in this DNS, the free surface is mainly stabilized under the effects of gravity.

5.6 Summary

In section, we perform DNS of the canonical FST flow in Chapter 3 to confirm the predictions of the new model of bubble size spectrum for FST entrainment $\mathcal{N}_a^E(r)$. We measure the bulk bubble size spectrum $N_a(r)$ from the DNS results to understand the characteristics and behaviors of $\mathcal{N}_a^E(r)$. Our new model predicts that the amplitude of $\mathcal{N}_a^E(r)$ scales as g^{-1} when gravity g is more important than surface tension in FST entrainment. On the other hand, the amplitude of $\mathcal{N}_a^E(r)$ scales as $(\sigma/\rho)^{-1}$ when surface tension σ is more important. In the first part, we perform DNS over a broad range of Fr and We to investigate the dependence of air entrainment on g and σ. We define an average entrainment volume rate $\overline{Q}_{\mathcal{E}}$ (over a period when the air-entraining SFST is quasi-static). We obtain the dependence of $\overline{Q}_{\mathcal{E}}$ on Fr and We. When either Fr^2 or We is below some respective critical values Fr_{cr}^2 and We_{cr}, $\overline{Q}_{\mathcal{E}}$ is negligible. These observations indicate that no air entrainment can happen when the stabilization effect by gravity or surface tension exceeds the disrupting effect of near-surface turbulence. For sufficiently large $We > We_{cr}$ and $Bo_r > O(1)$, $\overline{Q}_{\mathcal{E}}$ scales

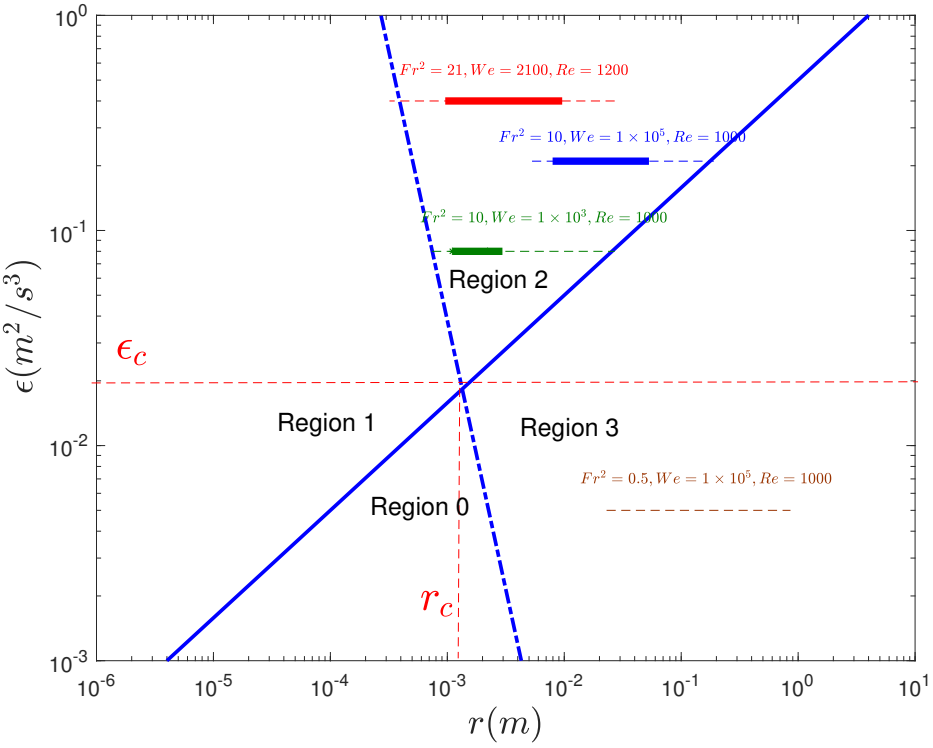

Figure 5-17: Conceptual diagram of the (r, ϵ)-plane for FST driven bubble entrainment near air-water interface. — · —, the lower bound of bubble size r_l; ——, the upper bound of bubble size r_u. The critical value of turbulence dissipation rate for entrainment is $\epsilon_c \approx 0.02 W/kg$. The capillary length scale is $r_c \approx 1.5mm$. The information of the corresponding DNS case of each data point shown in the diagram is listed in table5.1. ——shows the size range of entrained bubbles. - - -shows the range from grid size Δ to the flow characteristic length L in the DNS.

as Fr^2 for $Fr^2 > Fr_{cr}^2$. On the other hand, for sufficiently large $Fr^2 > Fr_{cr}^2$ and $Bo_r < O(1)$, $\overline{Q}_{\mathcal{E}}$ scales as We for $We > We_{cr}$. These dependencies of $\overline{Q}_{\mathcal{E}}$ on Fr^2 and We are also supported by considering the magnitude of average increase rate of bubble spectrum $\overline{Q}_{\mathcal{N}}(r)$.

We further study the dependence of $\mathcal{N}_a^E(r)$ on ϵ. We consider four flows with different initial velocity profiles to generate turbulence with different levels of dissipation rate. We find that both the entrainment rate and the magnitude of increase rate of bubble size spectrum are found to be scaled by a quantity $\int_{t_a}^{t_e} \epsilon(\tau)^{2/3} d\tau$, which measures the integrated (averaged) turbulence dissipation during the entrainment period. The results indicate that $N_a(r) \propto \epsilon^{2/3}$.

To further validate the two power-law regimes of $\mathcal{N}_a^E(r)$ predicted by the new model, a high-resolution DNS of the canonical FST flow is performed. The numerical results confirms the new model mainly on three aspects: 1) the power-law for large r regime is $\mathcal{N}_a^E(r) \propto r^{-10/3}$; 2) the power-law for small r regime is $\mathcal{N}_a^E(r) \propto r^{-4/3}$; 3) the separating scale is the capillary length scale instead of the Hinze scale.

In addition, the corresponding data points of several DNS cases are marked on the diagram of (r, ϵ)-plane. All the cases with/without air entrainment correctly fall in the regime of strong/weak free-surface turbulence regime.

Chapter 6

Interactions between vortex structures and free surface

In the previous chapters, the mechanisms of air entrainment in strong free-surface turbulence (SFST) and the resulted bubble size distribution are greatly discussed. A new parameterization model is proposed to describe the bubble size spectrum. DNS results of a canonical FST flow further provide evidences and supports to the new model. These results greatly improve our understanding of the physics of bubble entrainment in FST flows. However, individual entrainment events and the detailed entrainment processes still remain unclear.

In this chapter, we consider two different vortical structures and perform numerical simulations to investigate their interactions with the free surface. The focus of the study here is air entrainment induced by the vortex-surface interactions. We also study the dependence of air entrainment on relevant physical parameters (gravity g, surface tension σ/ρ, and viscosity ν) and vortex-structure-specific parameters. In particular, the dependencies of the entrainment volume on g and σ/ρ obtained in the single vortex induced entrainment event are consistent with those obtained in the SFST flow where numerous entrainment events happen. We also find a general linear dependence of the entrainment volume on a quantity of averaged vorticity flux which can be used in sub-grid models of air entrainment to achieve closures.

6.1 Pair of vortex tubes parallel to the free surface

6.1.1 Problem definition

We consider a simple canonical problem of the head-on collision of a pair of counter-rotating vortex tubes with the free surface as shown in figure 6-1. Each of the vortex tubes has an initial radius of a. The two tubes are assigned of a distance of L and in an angle of θ relative to the initial flat free surface. The vorticity field inside the tube follows a Gaussian core distribution, which satisfies the N-S equations for viscous flow.

$$\omega_y = \omega_c e^{-\frac{(\boldsymbol{x}-\boldsymbol{x_0})\cdot(\boldsymbol{x}-\boldsymbol{x_0})}{a^2}} \tag{6.1}$$

where ω_c is the initial maximum core vorticity and $\boldsymbol{x_0}$ is the centre of the tube. Because of the upward induced velocity, the vortex pair propagates to the free surface. Our focus in this study is the amount of air entrained (V) due to the collision of the vortex pair and the free surface. The parameters controlling V involve some basic physical parameters including gravity g, surface tension σ and water viscosity ν, as well as some case-specific parameters such as the initial maximum core vorticity ω_c, the distance of the two vortex L, the radius of the vortex tube a and the alignment angle θ. We write V as a function of all these parameters:

$$V = f(g, \sigma, \nu, \omega_c, a/L, \theta) \tag{6.2}$$

For this particular problem, we choose L as the length scale, ω_c^{-1} as the time scale. Then we normalize equation (6.2) and re-write it as:

$$A_e = F(Fr^2, We, Re, a/L, \theta) \tag{6.3}$$

where $A_e = V/3L^2$, $Fr^2 = \omega_c^2 L/g$, $We = \omega_c^2 L^3/(\sigma/\rho)$, and $Re = \omega_c L^2/\nu$. Hereafter in this section, all the variables are normalized by ω_c and L unless otherwise stated. It is noted that the initial depth of the vortex pair to the free surface is not considered as a parameter, but as a fixed one equal to L. The initial depth mainly affects vor-

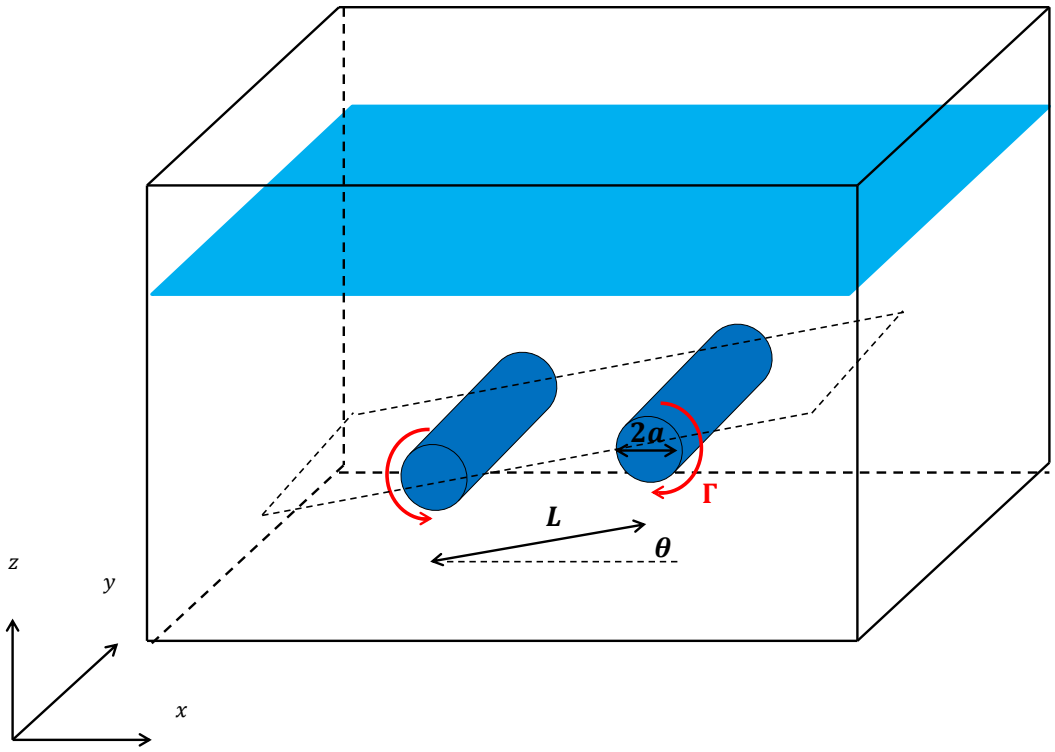

Figure 6-1: Definition sketch showing a free surface present at $z = 0$ with a pair of counter-rotating vortex tubes, each of which has a circulation of Γ. The distance of the two tubes is L and the radius of each tube is a. The two vortex tubes are aligned with an angle of θ compared to the initial flat free surface.

ticity diffusion/dissipation during the vortex pair propagation in the bulk water flow. However, for sufficiently large Re, this effect is small and assumed to be neglected.

For the cases of $\theta = 0$, the domain size is $6 \times 3 \times 6$ in the x, y and z direction, respectively. The initial flat free surface is at $z = 0$. The water domain is $z \in [-4, 0]$ and the air domain is $z \in [0, 2]$. The boundary condition in x direction is symmetric to simulate the pair of vortex. In y direction, the front and back boundaries are periodic, which allows us to consider this problem as two-dimensional. And the top and bottom boundaries in z direction are free-slip boundaries. For the cases of non-zero θ, the domain size in x dimension is doubled and both the two vortex tubes are placed in the domain.

To set-up the initial velocity field, we specify the initial vorticity field $\boldsymbol{\omega} = (0, \omega_y, 0)$

Table 6.1: Convergence study of the case ($Fr^2 = 12$, $We = \infty$, $Re = 1000$, $a/L = 0.2$, $\theta = 0$)

N_x	64	128	256
$\triangle$	0.094	0.047	0.023
A_e	0.051	0.063	0.061
$r_e/\triangle$	1.36	3.01	6.06

of the vortex tube following Zhang *et al.* (1999), where ω_y is given in (6.4). Given $\boldsymbol{\omega}$, the initial velocity field $\boldsymbol{u}$ can be obtained in terms of the vector stream function $\boldsymbol{\psi}$, defined by $\boldsymbol{u} = \nabla \times \boldsymbol{\psi}$. With $\boldsymbol{\omega} = \nabla \times \boldsymbol{u}$, ψ is computed by solving a Poisson equation governing ψ:

$$\nabla^2 \boldsymbol{\psi} = -\boldsymbol{\omega} \tag{6.4}$$

To establish that our numerical resolutions is sufficient, we perform numerical simulation of a case of zero θ on three different grids of number $N_x = 64$, 128 and 256 in x direction. The corresponding grid sizes of the three resolutions are $\Delta = 0.094$, 0.047 and 0.023. The detailed information of the case and the simulation results are summarized in table 6.1. Figure 6-2 shows the contour of volume fraction f of a x-z plane at $y = 1$ at an instantaneous time when air entrainment happens using the moderate resolution. A two-dimensional circular bubble of area A_e is observed. It is noticed that the value A_e obtained by using the two finest resolutions is consistent, while the value by using the coarsest resolution shows a clear difference. We further define an effective radius r_e as $r_e = (A_e/\pi)^{1/2}$. For the three resolutions, r_e is resolved by 1.36, 3.01 and 6.06 grids, respectively. For general VOF methods, two grids are required to fully resolve the shape of a two-dimensional circle. Therefore, the moderate resolution of grid number $N_x = 128$ and grid size $\Delta = 0.047$ is sufficient for the simulation of this vortex pair problem. All the numerical results presented in this chapter are obtained using this resolution unless otherwise state.

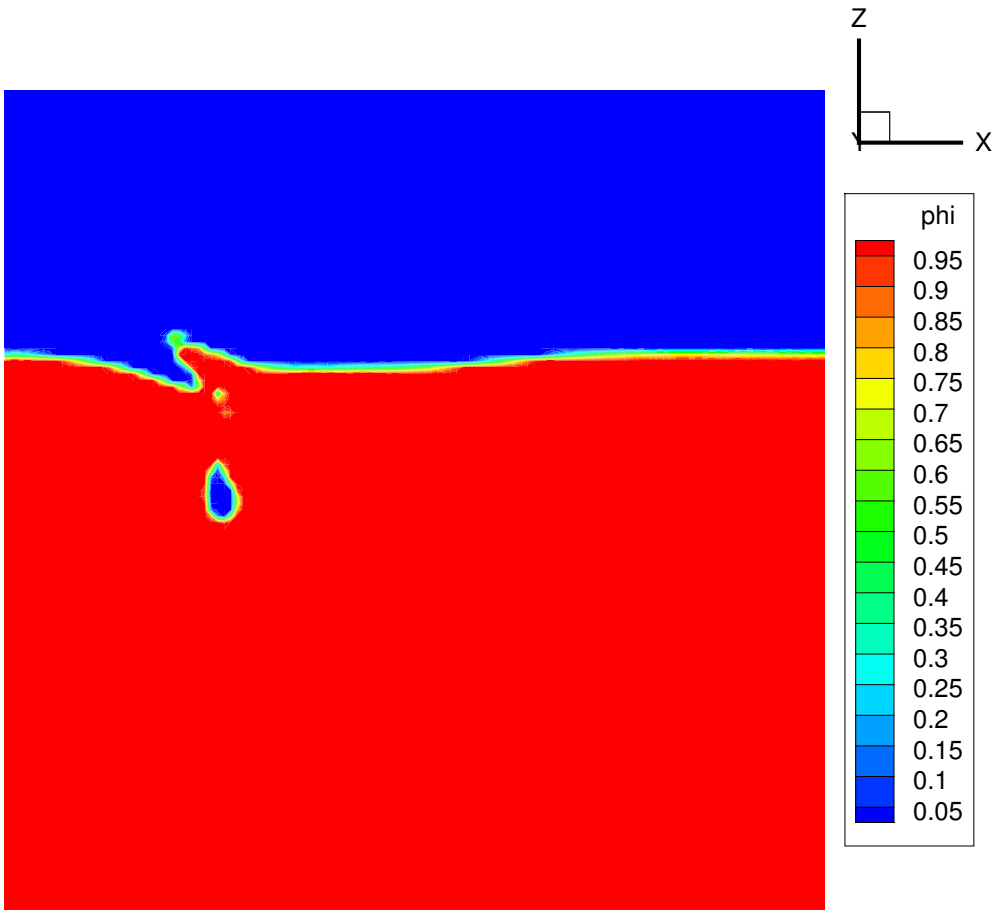

Figure 6-2: Contour of volume fraction f of a x-z plane of $y = 1$ at $t = 24$ when air entrainment happens. The parameters of the case are $Fr^2 = 12$, $We = \infty$, $Re = 1000$, $a/L = 0.2$, $\theta = 0$.

6.1.2 Process of entrainment induced by vortex pair

Figure 6-3 shows the evolution of one of the vortex tubes by plotting ω_y on a x-z plane at $y = 1$. The free surface is represented by the isogram of $f = 0.5$. The vortex tube moves approaching the free surface due to the upward induced velocity. The free surface, at the same time, deforms and forms a local trough due to the velocity moving downwards, which corresponds to an anti-splat event as shown in figure 6-4. At the same time, the deformed surface creates a vorticity field in the air domain. Vorticity in the air domain is further enhanced as the the surface trough develops. Later on when the free surface reconnects as shown in figure 6-5, an air pocket is enclosed in the water, creating air entrainment.

Due to the presence of the free surface, the upwards propagation of the vortex is constrained, so it moves outwards and then downwards. Figure 6-6 shows the evolution of the vortex core position for two cases of different Fr^2. Consistent with that in Yu & Tryggvason (1990), the vortex moves wider to the side for smaller Fr. Note that we will not pay much attention to the dynamics of vorticity during the vortex-surface interaction in this vortex pair case. Since this case is equivalently a two-dimensional problem, interesting physics of vorticity such as stretching and rotating do not exist here. Instead, we will study the vorticity dynamics in the three-dimensional vortex ring case later.

For a case with larger Fr^2, the vortex pair induces larger surface deformation, which further causes strong vorticity in the air domain. The induced vortices in the air domain can cause a secondary turnover of the free surface and result in a secondary entrainment event. Here we show one example by looking at a similar case but with $Fr^2 = 18$ in figure 6-7. Here we focus on the first entrainment event as it is directly related to the vortical structures.

For a case of $\theta \neq 0$, the entrainment process is similar than that described above. Figure 6-8 shows the detailed process of the entrainment event by a vortex pair with $\theta = \pi/9$. Due to asymmetric alignment of the vortex pair, the entrainment event induced by each vortex tube happens at different time. For the right-side vortex,

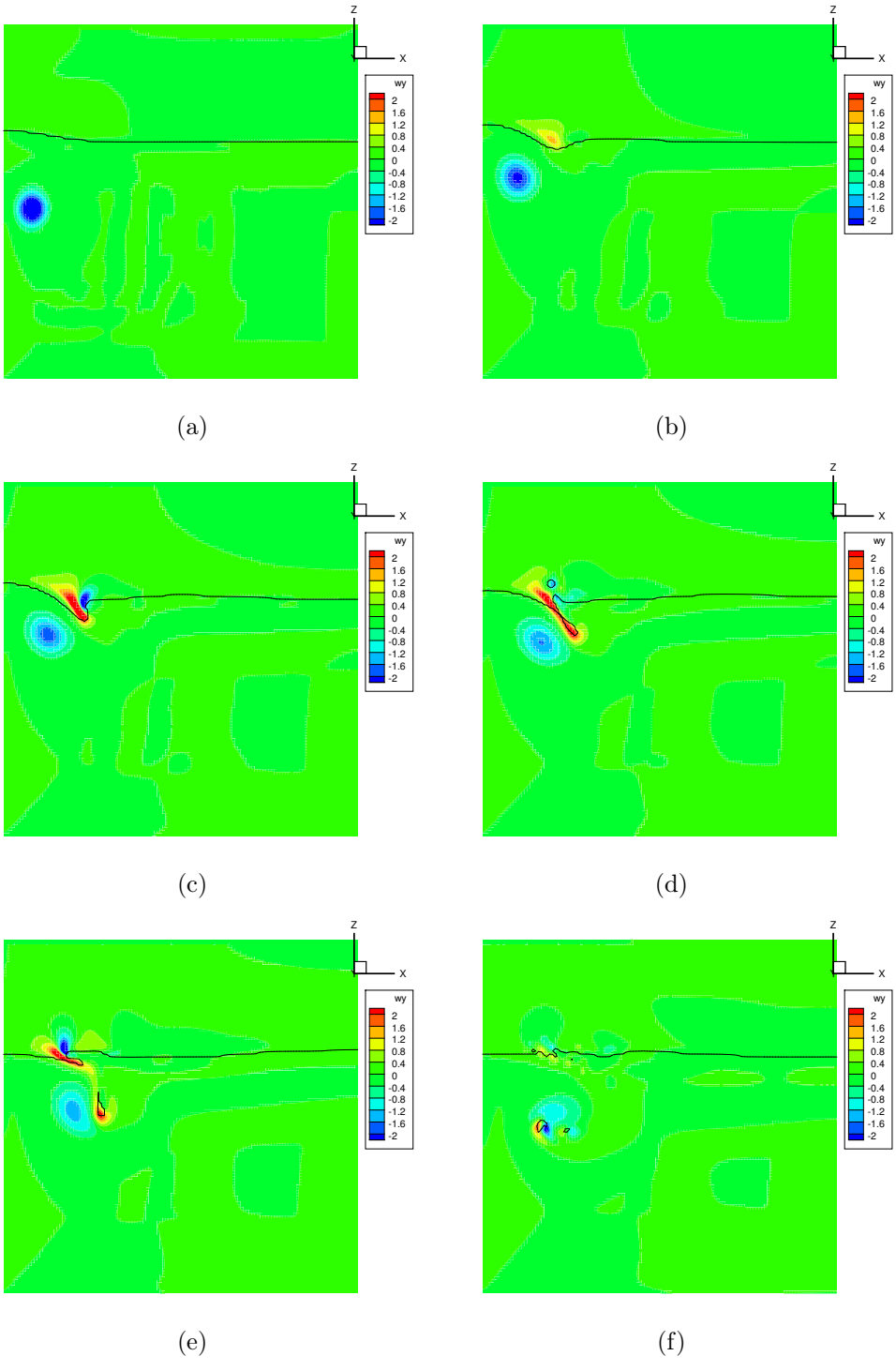

(a) (b)

(c) (d)

(e) (f)

Figure 6-3: Process of the entrainment event induced by one of the vortex pair. Contour plot is the vorticity component in y direction, ω_y, of a x-z plane of $y = 1$. The free surface is represented by the solid isogram of $f = 0.5$. The parameters of the case are $Fr^2 = 10$, $We = \infty$, $Re = 1000$, $a/L = 0.2$, $\theta = 0$. (a) t=4; (b) t=12; (c) t=16; (d) t=20; (e) t=24; (f) t=32.

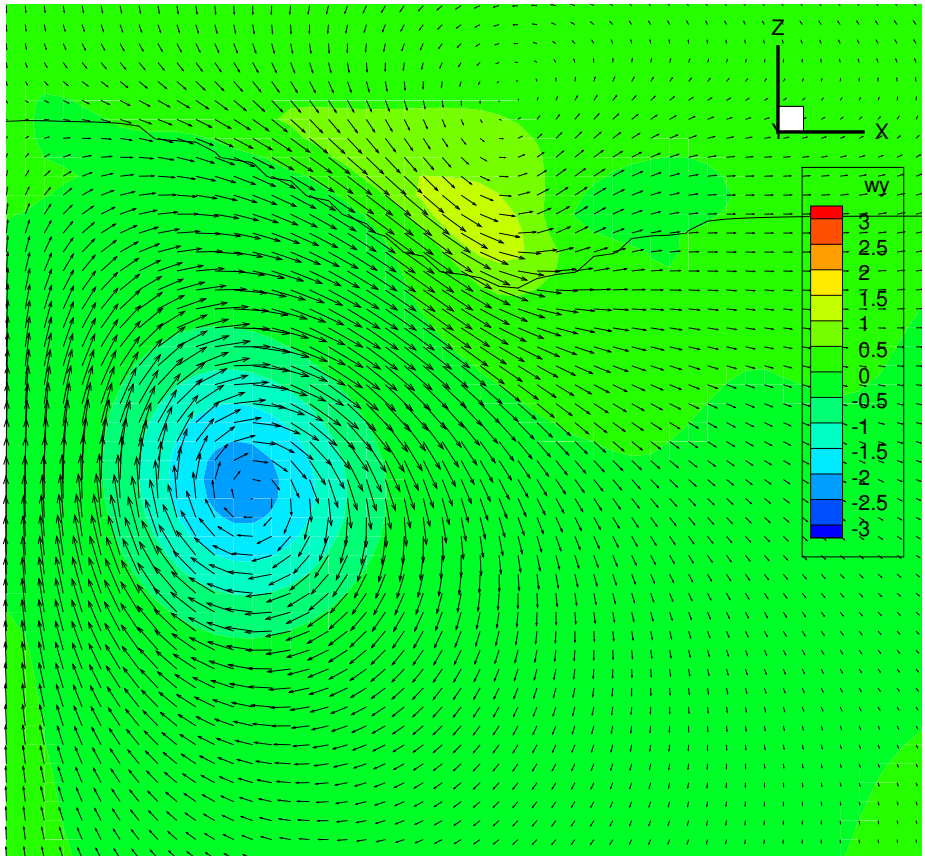

Figure 6-4: Contour of vorticity component in y direction, ω_y, of a x-z plane of $y = 1$ at $t = 12$ before air entrainment happens. The velocity field is shown using arrows. The free surface is represented by the solid isogram of $f = 0.5$. The parameters of the case are $Fr^2 = 10$, $We = \infty$, $Re = 1000$, $a/L = 0.2$, $\theta = 0$.

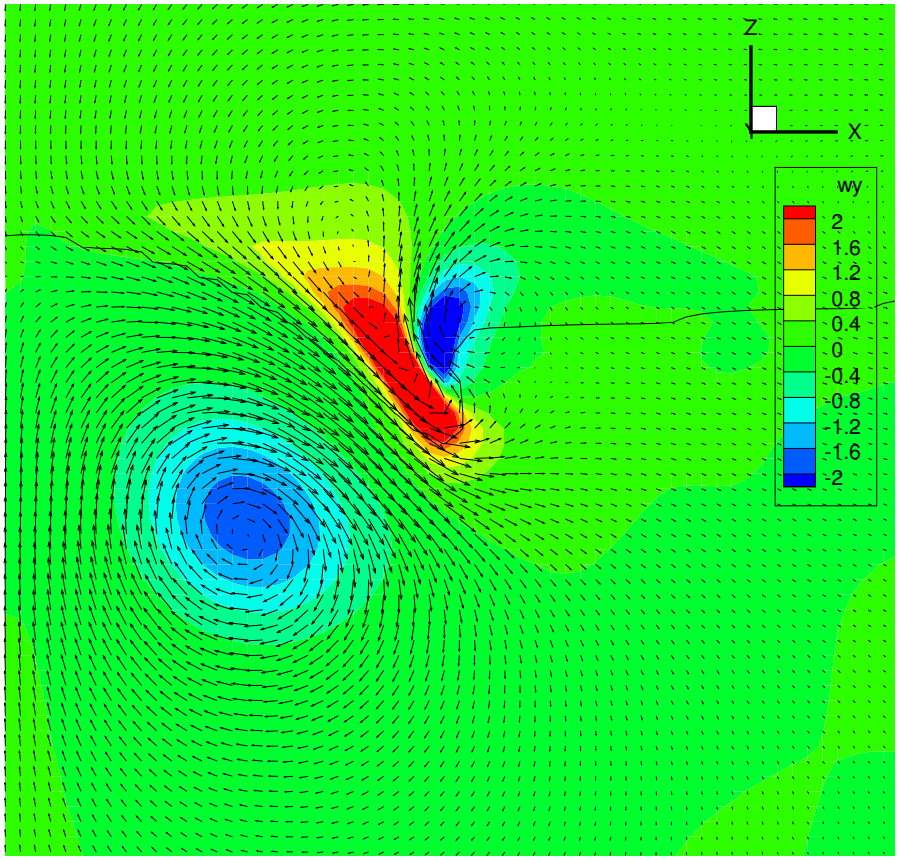

Figure 6-5: Contour of vorticity component in y direction, ω_y, of a x-z plane of $y = 1$ at $t = 16$ when the free surface reconnects. The velocity field is shown using arrows. The free surface is represented by the solid isogram of $f = 0.5$. The parameters of the case are $Fr^2 = 10$, $We = \infty$, $Re = 1000$, $a/L = 0.2$, $\theta = 0$.

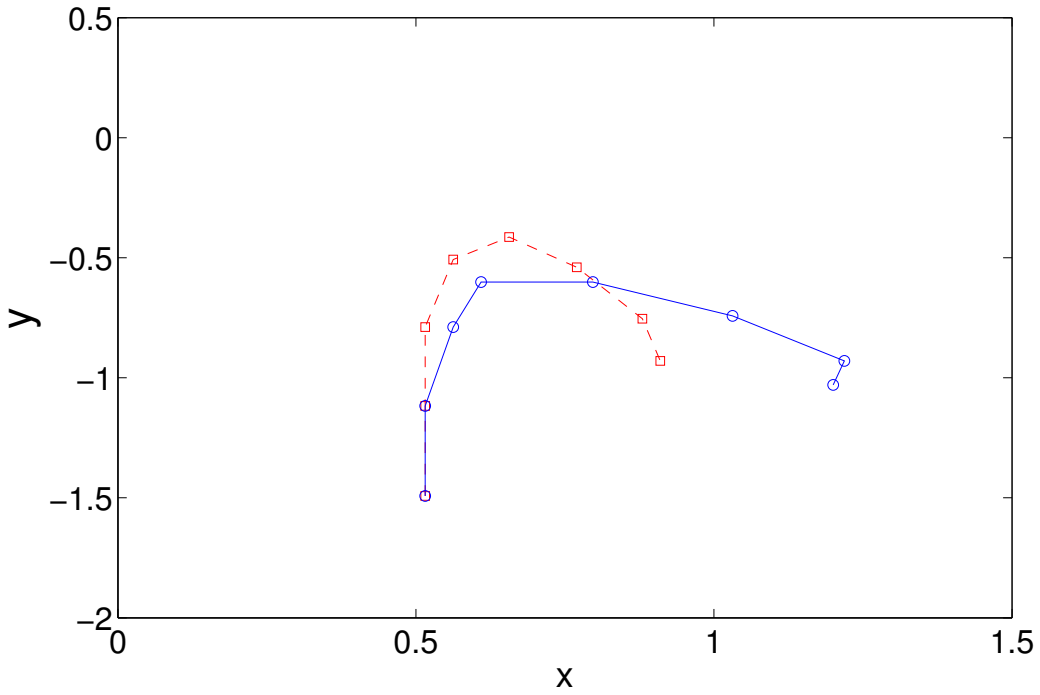

Figure 6-6: Evolution of the core position of the vortex from t=0 to t=28. –○–, low Fr case of $Fr^2 = 10$; - -□- -, high Fr case if $Fr^2 = 18$. The rest parameters are $We = \infty$, $Re = 1000$, $a/L = 0.2$, $\theta = 0$.

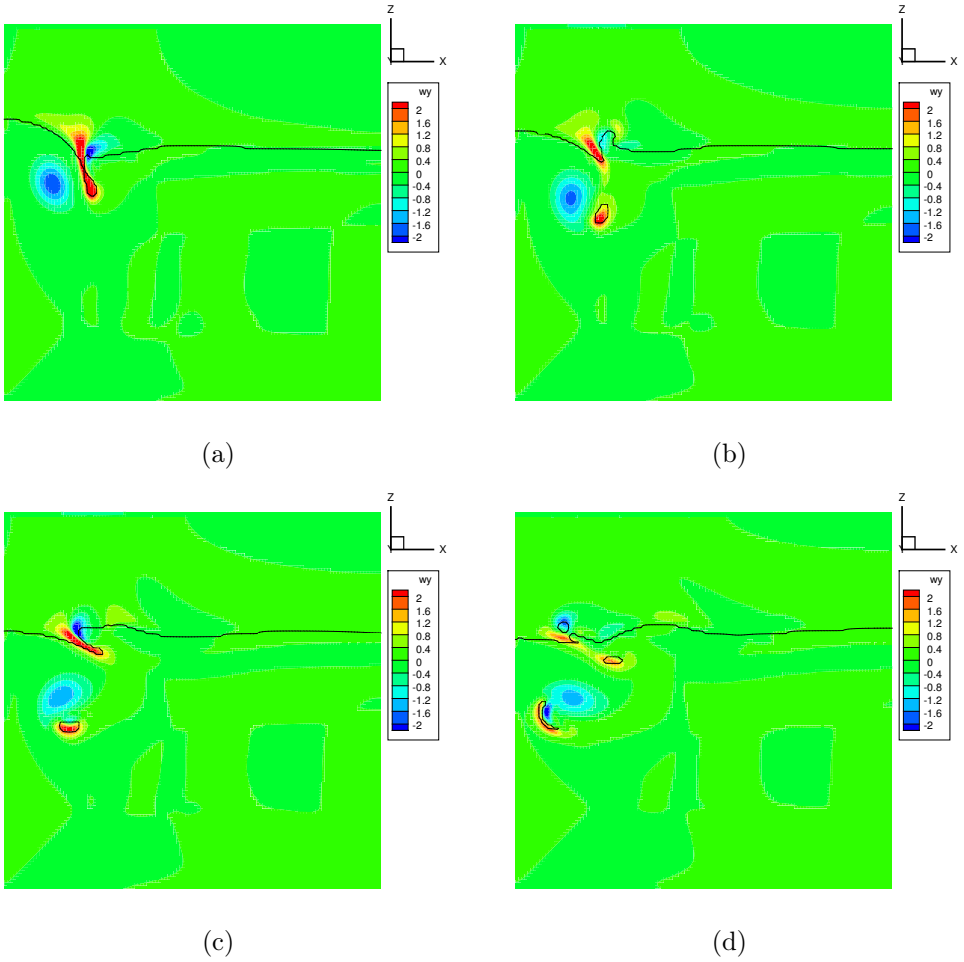

(a) (b)

(c) (d)

Figure 6-7: Process of secondary entrainment event at high Fr. Contour plot is the vorticity component in y direction, ω_y, of a x-z plane of $y = 1$. The free surface is represented by the solid isogram of $f = 0.5$. The parameters of the case are $Fr^2 = 18$, $We = \infty$, $Re = 1000$, $a/L = 0.2$, $\theta = 0$. (a) t=20; (b) t=24; (c) t=28; (d) t=32.

the entrainment is finished at $t = 20$ when the entrainment process by the left-side vortex just starts. The left-side vortex induced entrainment finishes at $t = 32$. When θ increases to $\pi/4$, the entrainment event due to the left-side vortex does not happen as shown figure 6-9. This is mainly because the left vortex is diffused significantly after a long propagation from the bulk flow to the free surface.

6.1.3 Dependence of entrainment volume on Fr, We, a/L, and Re

Following equation (6.3), we investigate the dependence of the entrainment volume on Fr, We, a/L and Re separately. To do so, we vary a particular parameter and fix others. Figure 6-10 shows the entrainment volume A_e as a function of Fr^2 with fixed $We = \infty$, $Re = 1000$, $a/L = 0.2$, and $\theta = 0$. There exists a critical Fr_{cr}, below which no air entrainment happens. In this particular case with the fixed parameters, Fr_{cr} is around 1.6. Below Fr_{cr}, the gravity force becomes so strong and the free surface is significantly stabilized. Large surface deformation and air entrainment are fully suppressed. For $Fr > Fr_{cr}$, A_e shows a linear dependence on Fr^2. By varying Fr^2 with other parameters fixed, we essentially change the gravity force. Therefore, figure 6-10 suggests that the entrainment volume scales as g^{-1}.

Besides gravity, surface tension is also a stabilization force on the free surface. We vary We with fixed $Fr^2 = 16$, $Re = 1000$, $a/L = 0.2$, and $\theta = 0$. Figure 6-11 shows A_e as a function of We. We observe two regimes where surface tension is respectively important or unimportant relative to gravity. These two regimes are delineated by $Bo_r = \rho g l_c^2/\sigma \approx 1$ with the capillary length scale l_c being a characteristic length scale of the entrainment size of order Δ, or $We \approx O(We_1) = O(5 \times 10^3)$. The effect of surface tension on entrainment is negligible for $We \gg O(We_1)$. In figure 6-11, A_e at $We = 2 \times 10^4$ is observed to be close to the value at $We = \infty$. For $We \lesssim O(We_1)$, surface tension becomes important and A_e is observed to be linearly dependent on We in figure 6-11. This result suggests that the entrainment volume scales as σ^{-1} when the surface tension effects are dominant relative to the gravity effects on the

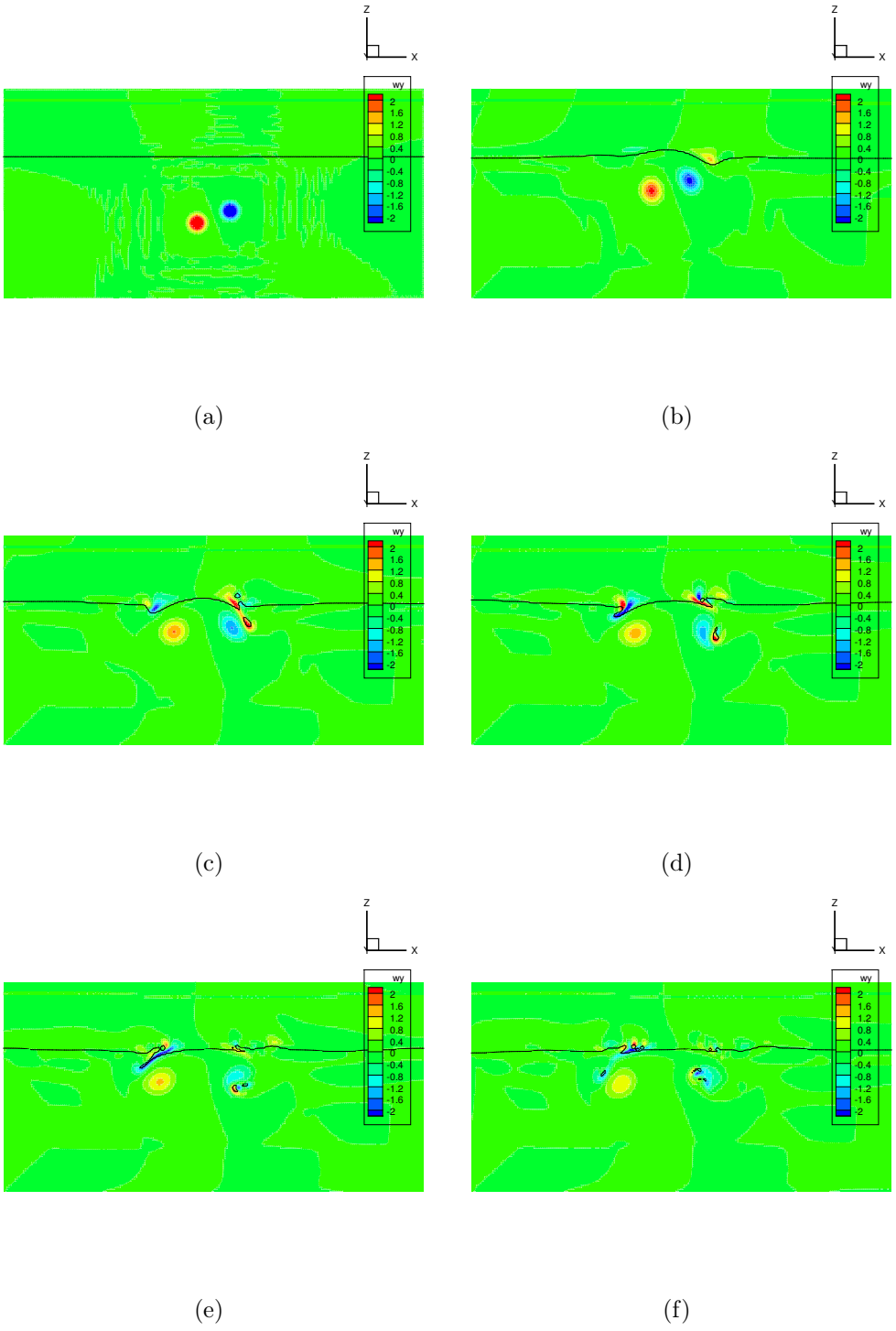

(a) (b)

(c) (d)

(e) (f)

Figure 6-8: Process of the entrainment event induced by the vortex pair with non-zero alignment angle $\theta = \pi/9$. Contour plot is the vorticity component in y direction, ω_y, of a x-z plane of $y = 1$. The free surface is represented by the solid isogram of $f = 0.5$. The parameters of the case are $Fr^2 = 10$, $We = \infty$, $Re = 1000$, $a/L = 0.2$, $\theta = \pi/9$. (a) t=0; (b) t=12; (c) t=20; (d) t=24; (e) t=28; (f) t=32.

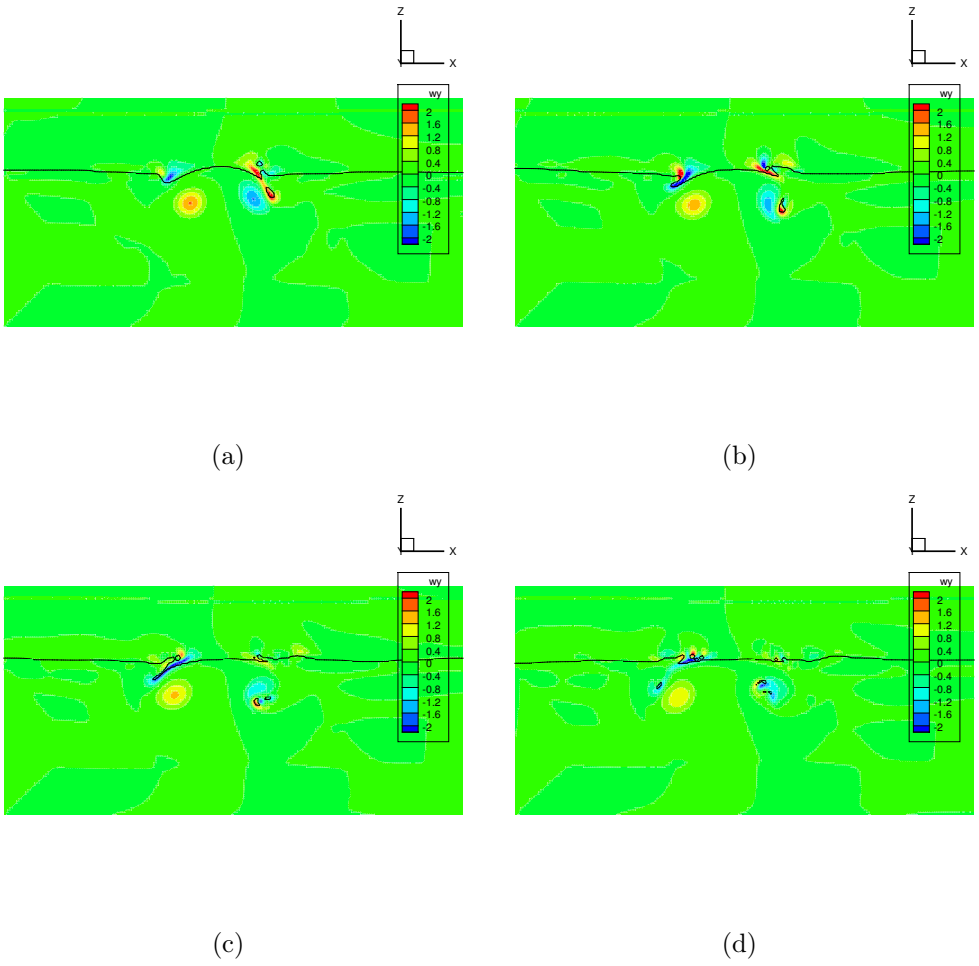

(a) (b)

(c) (d)

Figure 6-9: Process of the entrainment event induced by the vortex pair with non-zero alignment angle $\theta = \pi/4$. Contour plot is the vorticity component in y direction, ω_y, of a x-z plane of $y = 1$. The free surface is represented by the solid isogram of $f = 0.5$. The parameters of the case are $Fr^2 = 10$, $We = \infty$, $Re = 1000$, $a/L = 0.2$, $\theta = \pi/4$. (a) t=20; (b) t=24; (c) t=28; (d) t=32.

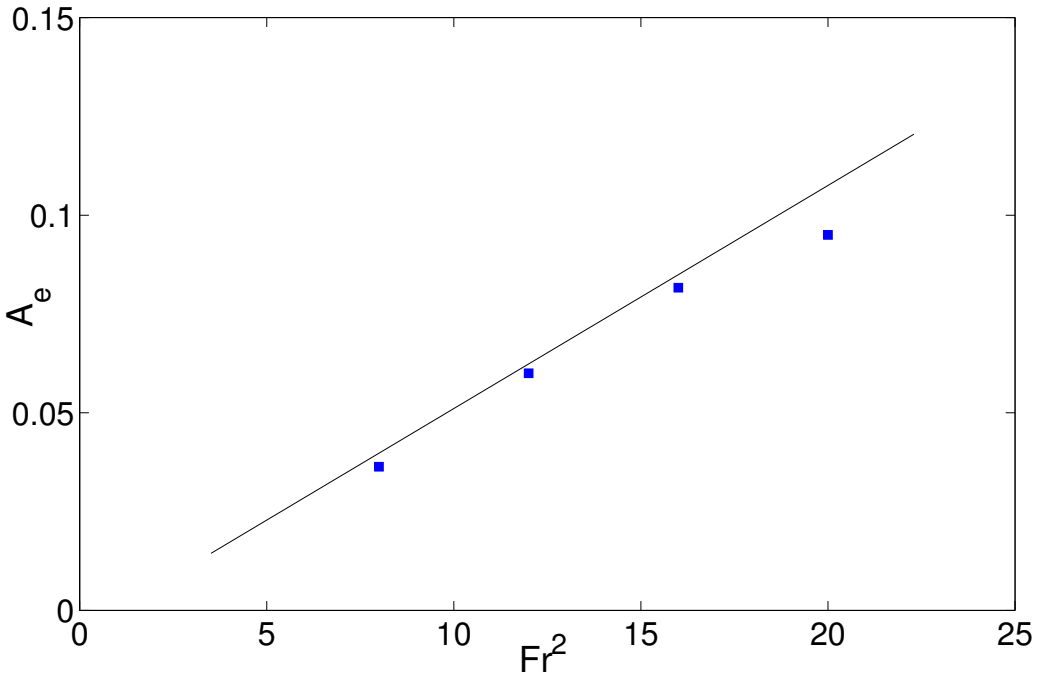

Figure 6-10: Volume of entrainment induced by one of the vortex pair, A_e, as a function of Fr^2. Other parameters of the cases are $We = \infty$, $Re = 1000$, $a/L = 0.2$, and $\theta = 0$.

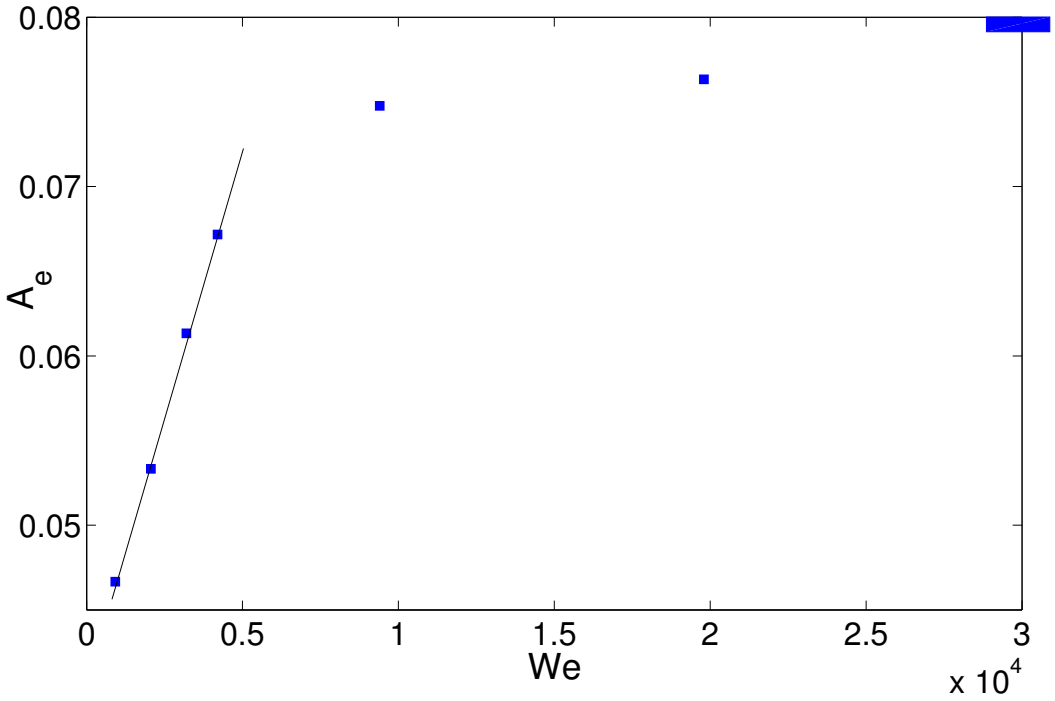

Figure 6-11: Volume of entrainment induced by one of the vortex pair, A_e, as a function of We. Other parameters of the cases are $Fr^2 = 16$, $Re = 1000$, $a/L = 0.2$, and $\theta = 0$.

entrainment process. Similar to Fr_{cr}, there also exists a critical We_{cr}, below which no air entrainment is observed. For this particular case with the fixed parameters, We_{cr} is of order 100.

Figure 6-12 shows A_e as a function of a/L with fixed $Fr^2 = 16$, $We = \infty$, $Re = 1000$, and $\theta = 0$. It is observed that A_e scales as a/L. When a/L varies, the distribution of the vorticity field and the induced velocity changes. Figure 6-13 and 6-14 show the contour of u and w of a x-z plane of $y = 1$ from two cases of $a/L = 0.2$ and $a/L = 0.22$. As observed, larger a/L induces larger velocity. In fact, the effect of a/L is mainly on w instead of u. Therefore, the linear dependence of A_e on a/L indicates that A_e is affected by the induced velocity field as well. Figure 6-15 shows the average vertical velocity in the water domain, $\overline{w^2}^{1/2}$, at $t = 0$ and suggests a linear dependence on a/L.

We consider three different Re with fixed $Fr^2 = 16$, $We = \infty$, $a/L = 0.2$, and $\theta = 0$. A_e obtained using the three Re are summarized in table 6.2. For the three

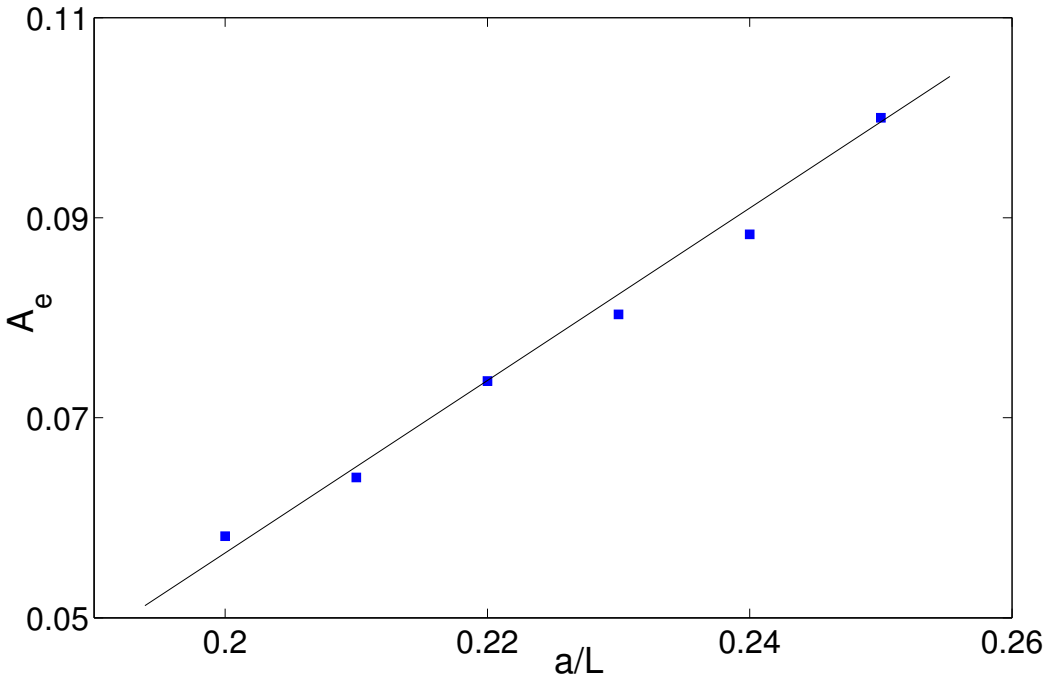

Figure 6-12: Volume of entrainment induced by one of the vortex pair, A_e, as a function of a/L. Other parameters of the cases are $Fr^2 = 10$, $We = \infty$, $Re = 1000$, and $\theta = 0$.

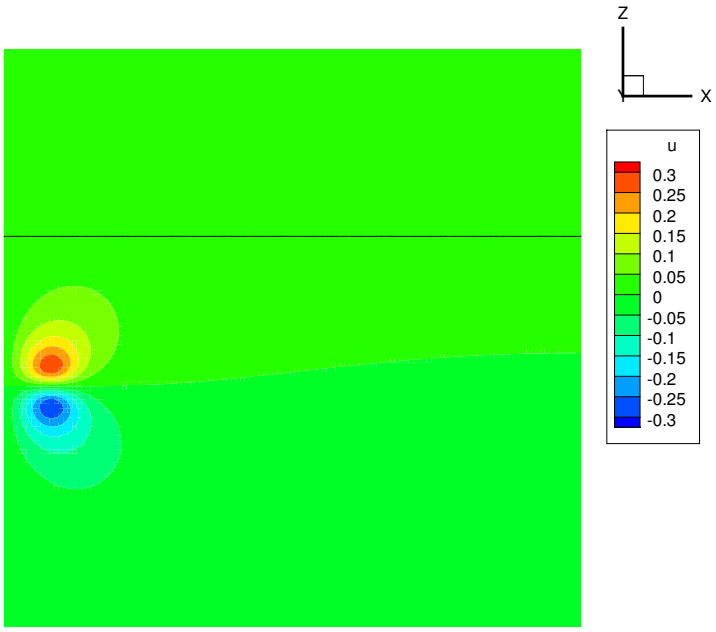

(a)

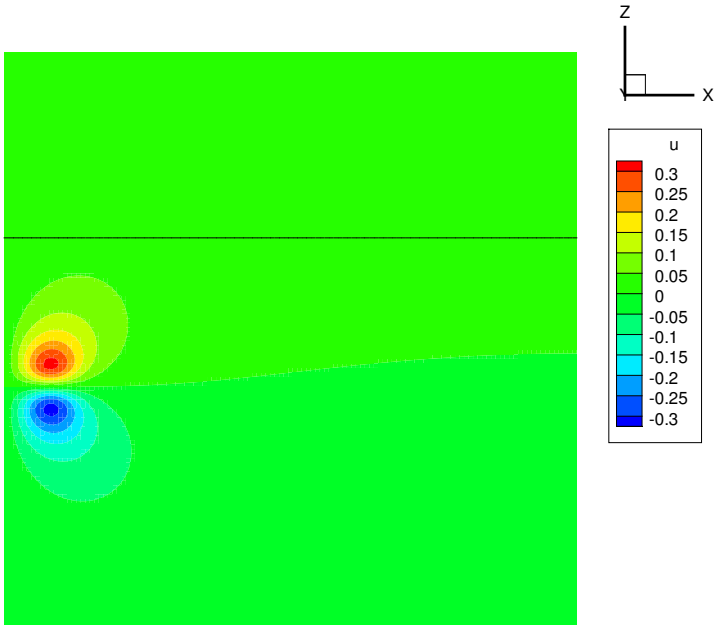

(b)

Figure 6-13: Contour of velocity component in x direction, u, of a x-z plane of $y = 1$ at $t = 0$. The free surface is represented by the solid isogram of $f = 0.5$. (a) case with $a/L = 0.2$; (b) case with $a/L = 0.22$. Others parameters of the casse are $Fr^2 = 10$, $We = \infty$, $Re = 1000$, $\theta = 0$.

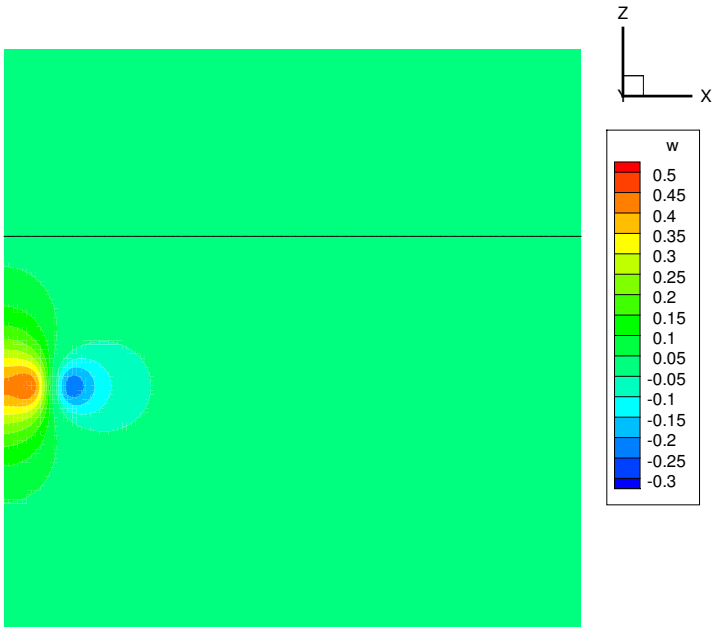

(a)

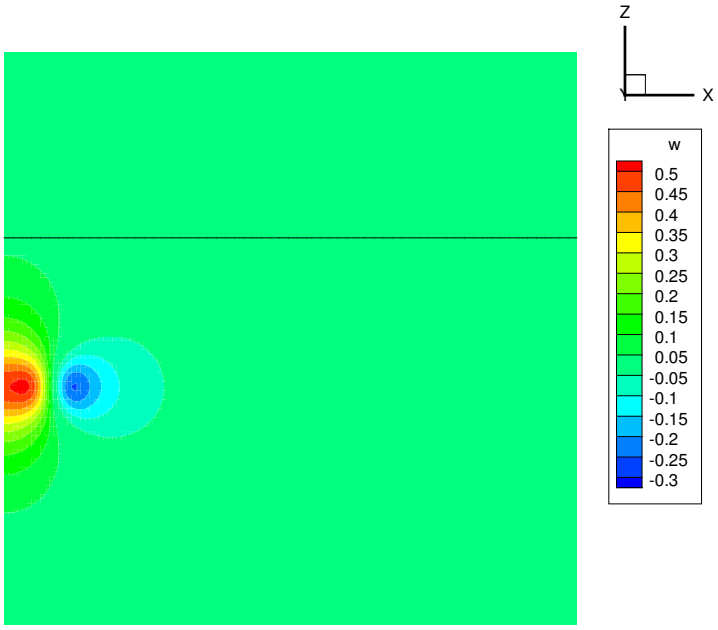

(b)

Figure 6-14: Contour of velocity component in z direction, w, of a x-z plane of $y = 1$ at $t = 0$. The free surface is represented by the solid isogram of $f = 0.5$. (a) case with $a/L = 0.2$; (b) case with $a/L = 0.22$. Others parameters of the casse are $Fr^2 = 10$, $We = \infty$, $Re = 1000$, $\theta = 0$.

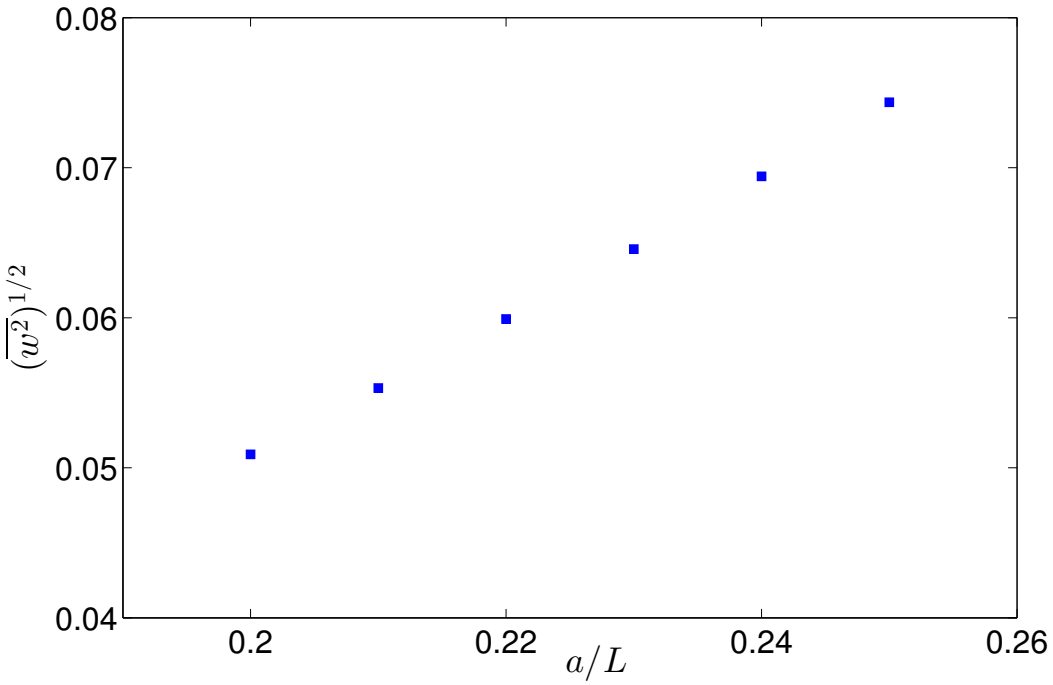

Figure 6-15: Average vertical velocity in the water domain, $\overline{w^2}^{1/2}$, at $t = 0$, as a function of a/L. Other parameters of the cases are $Fr^2 = 10$, $We = \infty$, $Re = 1000$, and $\theta = 0$.

Table 6.2: Volume of entrainment induced by one of the vortex pair with three different Re. The other parameters are $Fr^2 = 12$, $We = \infty$, $a/L = 0.2$, $\theta = 0$.

Re	1000	1200	1400
A_e	0.057	0.058	0.060

Re, the change of A_e is realized to be less than 5%. For sufficiently large Re, small variation of Re has limited effects on the entrainment volume A_e.

6.1.4 Dependence of entrainment volume on vorticity flux

For this particular canonical problem of vortex-pair, we have studied the dependence of air entrainment on the controlling parameters in great detail. In complex FST flows, numerous vortical structures are formed below the free surface. They are connected and interact with each other, so it is impossible to identify and isolate these vortical structures. In RANS of two-phase SFST flows, the governing equations contain several sub-grid terms of entrainment that must be modeled in terms of averaged quantities in order to achieve closures. Therefore, instead of the parameters in (6.3), we need a more general averaged quantity to predict the entrainment volume. In this subsection, we attempt to find such a quantity, and provide useful insight and guidance for further studies, based on our study on the simple vortex pair problem. Here we consider three different series of simulations with varying ω_c, a/L, and both. The information of all the simulations performed and the corresponding resulted entrainment volume are summarized in table 6.3$\sim$ 6.5.

In table 6.3, the initial maximum core vorticity ω_c inside the vortex tubes varies. Figure 6-16 shows A_e as a function of ω_c^2 and confirms that A_e has a linear dependence on ω_c^2. In table 6.4, the radius of the vortex tube a changes. Figure 6-12 in §6.1.3 shows that A_e scales as a/L. In table 6.4, both ω_c and a change. These two parameters affect A_e together and make the prediction of A_e more challenging.

To find a general averaged quantity for modeling the sub-grid terms of entrainment in RANS of two-phase SFST flows, we consider two potential quantities related to

Table 6.3: Numerical simulations of vortex pair with varying initial maximum core vorticity ω_c

Case	Fr^2	We	Re	a/L	θ	ω_c^2	A_e
1	10	∞	1000	0.2	0	1.0	0.057
2	12	∞	1095	0.2	0	1.2	0.066
3	14	∞	1183	0.2	0	1.4	0.072
4	16	∞	1265	0.2	0	1.6	0.077
5	18	∞	1342	0.2	0	1.8	0.082
6	20	∞	1414	0.2	0	2.0	0.087
7	23	∞	1517	0.2	0	2.3	0.095
8	25	∞	1265	0.2	0	2.5	0.103

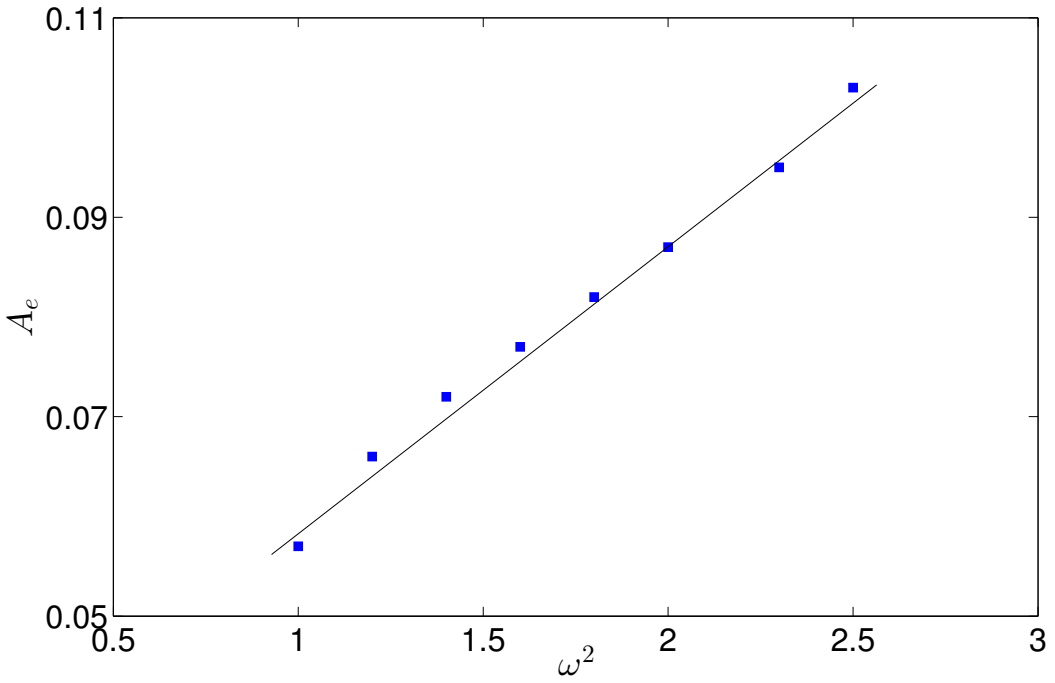

Figure 6-16: Volume of entrainment induced by one of the vortex pair, A_e, as a function of the initial maximum core vorticity ω_c^2. The data is from table 6.3

Table 6.4: Numerical simulations of vortex pair with varying initial radius of vortex tube a

Case	Fr^2	We	Re	a/L	θ	A_e
1	10	∞	1000	0.20	0	0.057
2	10	∞	1000	0.21	0	0.064
3	10	∞	1000	0.22	0	0.074
4	10	∞	1000	0.23	0	0.080
5	10	∞	1000	0.24	0	0.088
6	10	∞	1000	0.25	0	0.100

Table 6.5: Numerical simulations of vortex pair with varying initial maximum core vorticity ω_c and the radius of vortex tube a

Case	Fr^2	We	Re	a/L	θ	ω_c	A_e
1	10	∞	1000	0.20	0	1.0	0.057
2	8.1	∞	900	0.22	0	0.9	0.067
3	6.4	∞	800	0.25	0	0.8	0.076
4	4.9	∞	700	0.28	0	0.7	0.089
5	3.6	∞	600	0.33	0	0.6	0.107

the vorticity field in the bulk. The first is the averaged vorticity intensity over the bulk $\overline{\omega_y^2}$ defined as:

$$\overline{\omega_y^2} = 1/V_b \int_{V_b} \omega_y^2(\boldsymbol{x}) d\boldsymbol{x} \tag{6.5}$$

where V_b is the bulk volume. The other is the averaged vorticity flux in the vertical direction $\overline{|\omega_y|w}$ defined as:

$$\overline{|\omega_y|w} = 1/V_b \int_{V_b} |\omega_y(\boldsymbol{x})| w(\boldsymbol{x}) d\boldsymbol{x} \tag{6.6}$$

$\overline{|\omega_y|w}$ measures the rate of horizontal vorticity transported from the water domain to the free surface. It considers both the vorticity and the velocity field that are observed to affect the eventual entrainment volume. Larger $\overline{|\omega_y|w}$ indicates stronger collision or interaction of the vortex with the free surface. Figure 6-17 shows A_e as a function of $\overline{\omega_y^2}$ for the data listed in the table 6.3$\sim$ 6.5. The three data sets show three different branches, which indicates that $\overline{\omega_y^2}$ is not helpful and general enough for modeling sub-grid terms of entrainment in RANS. On the other hand, figure 6-18 shows a function of $\overline{|\omega_y|w}$. We observe that all the data points collapse into the same line and suggests a scaling law of $A_e \propto \overline{|\omega_y|w}$ no matter how those case-specific parameters (ω_c and a/L) vary. This result is of practical importance and suggests that $\overline{|\omega_y|w}$ is a general averaged quantity that can be used for the development of air entrainment model in RANS or LES simulations for FST flows. In those simulations, $\overline{|\omega_y|w}$, is available to obtain.

6.1.5 Dependence of entrainment volume on θ

The effects of the initial alignment angle θ of the vortex pair on the eventual entrainment volume are investigated in this subsection. Figure 6-19 shows A_e as a function of θ. Instead of a simple linear relation, the dependence of A_e on θ is quite subtle. For the range of $0 < \theta < \pi/4$, the effect of θ is limited. As θ increases, A_e is observed to increase slightly. This is counter to our conclusion in §6.1.4 where A_e is found to increase with the initial averaged vertical vorticity flux $\overline{|\omega_y|w}$. When θ is increased

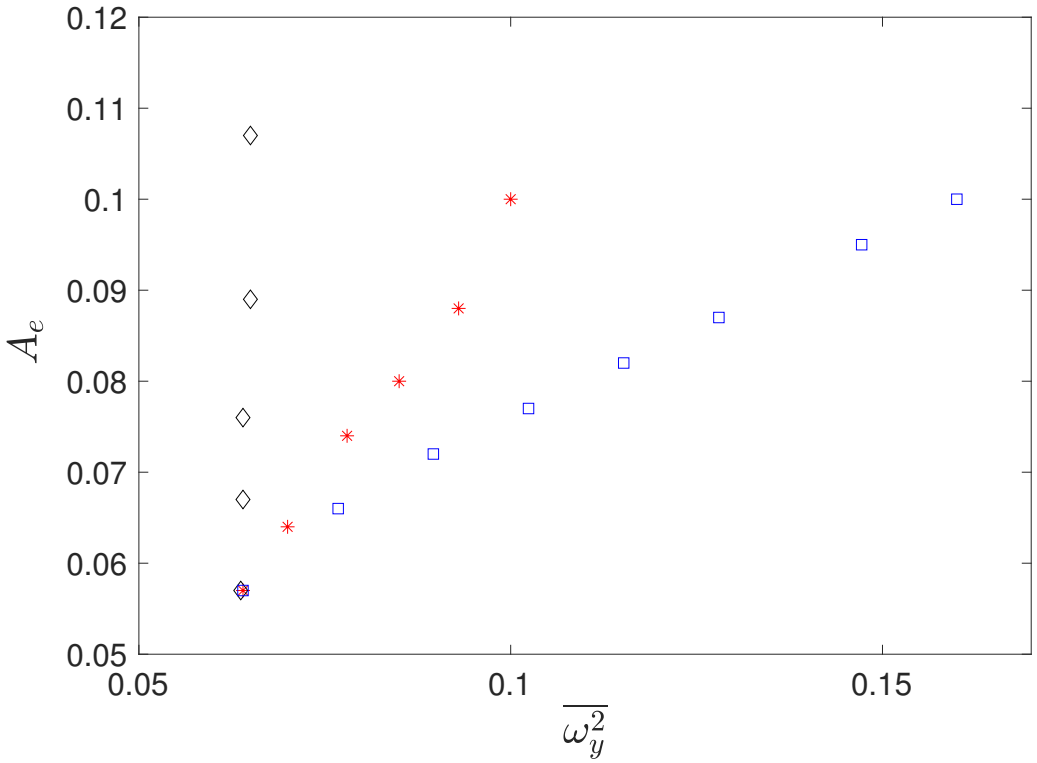

Figure 6-17: Volume of entrainment induced by one of the vortex pair, A_e, as a function of the averaged vorticity intensity over the bulk, $\overline{\omega_y^2}$, for the simulations listed in table from 6.3 to 6.5.

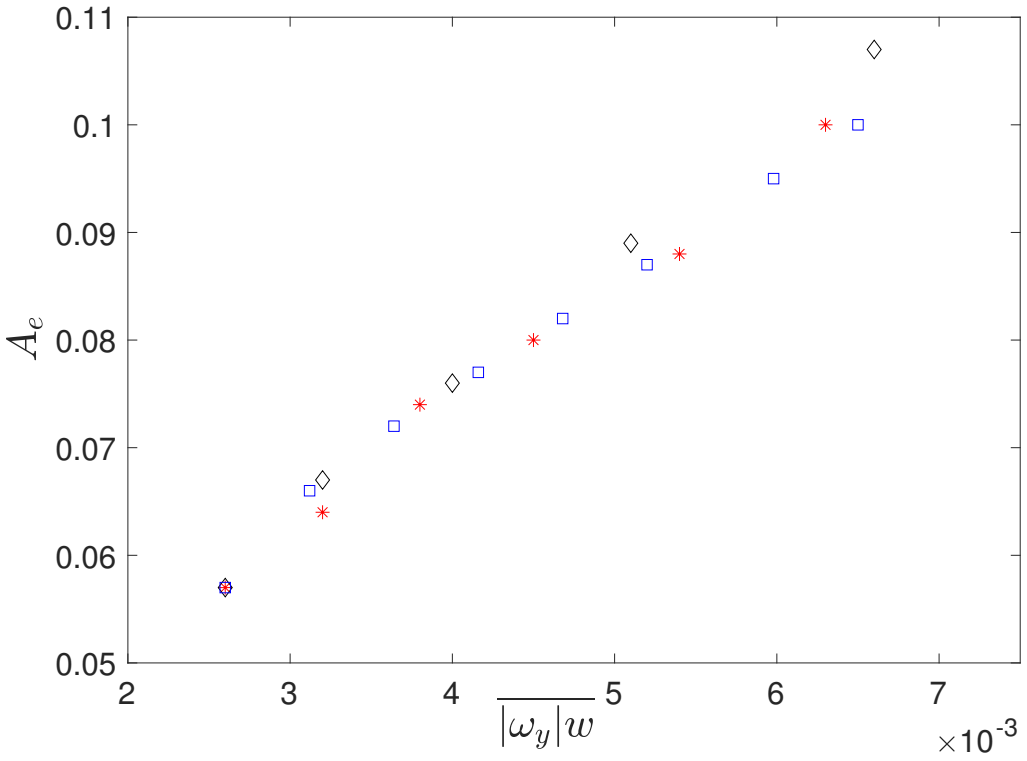

Figure 6-18: Volume of entrainment induced by one of the vortex pair, A_e, as a function of averaged vertical vorticity flux over the bulk, $\overline{|\omega_y|w}$, for the simulations listed in table from 6.3 to 6.5.

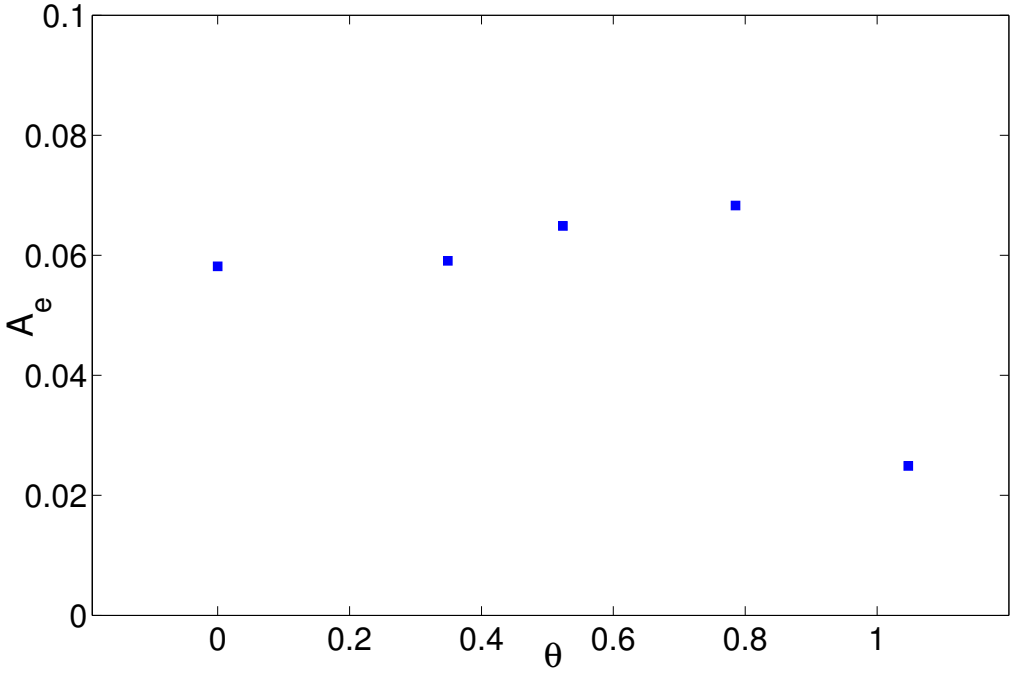

Figure 6-19: Volume of entrainment induced by the right vortex of the pair, A_e, as a function of θ. Other parameters of the cases are $Fr^2 = 10$, $We = \infty$, $Re = 1000$, and $a/L = 0.2$.

with other parameters fixed, $\overline{|\omega_y|w}$ decreases, which is expected to cause a decrease of A_e. However, in figure 6-19, A_e is observed to slightly increase in the range of $0 < \theta < \pi/4$. We argue that the abnormal increase of A_e is due to the influence of the asymmetry of surface deformation. As shown in figure 6-20 (b), when the surface reconnects, the non-zero θ induces a horizontal velocity at the crest of the free surface, which favors the surface reconnection process and the generation of entrainment. However, this influence has not been fully understood and quantified in this thesis. For the development of accurate sub-grid entrainment models, the influence of surface deformation needs to be carefully included and well quantified. For $\theta > \pi/4$, A_e drops rapidly as shown in figure 6-19. Due to the large θ, the vortex pair propagates nearly horizontally and its interaction with the free surface becomes weak, resulting in no entrainment.

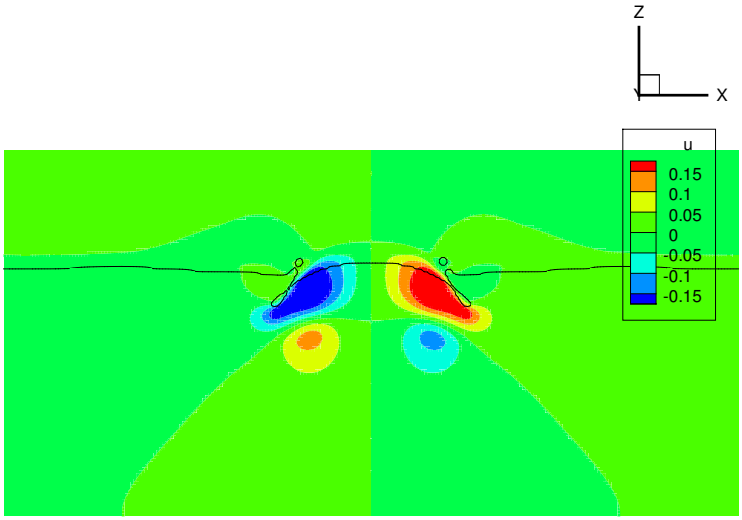

(a)

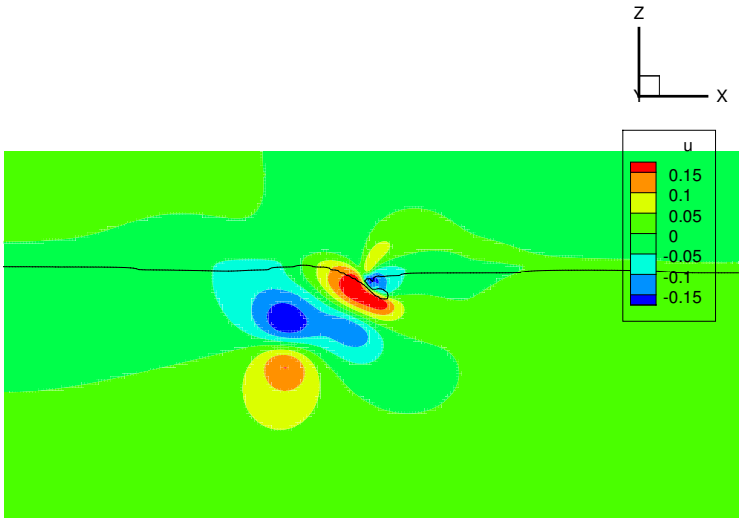

(b)

Figure 6-20: Contour of velocity component in x direction, u, of a x-z plane of $y = 1$ at $t = 20$ when the free surface reconnects. The free surface is represented by the solid isogram of $f = 0.5$. (a) case with $\theta = 0$; (b) case with $\theta = \pi/4$. Others parameters of the casse are $Fr^2 = 10$, $We = \infty$, $Re = 1000$, $a/L = 0.2$.

6.2 Process of entrainment induced by vortex ring

In this section, we consider a three-dimensional ring-structured vortex as an approximation of the Ω-shaped vortex observed in FST flows (Shen *et al.*, 1999; André & Bardet, 2017). Our focuses in the section include 1) the surface effects on underlying vorticity; 2) the entrainment process induced by the vortex ring; 3) the dependence of air entrainment on gravity, surface tension, and the initial circulation in the ring tube.

6.2.1 Problem definition

We consider an inclined vortex ring impinging to the free surface. The sketch of the problem is shown in figure 6-21. The vortex ring has an outer radius R and an inner radius r. The initial circulation inside the ring tube is Γ. And the inclined angle is α. The vorticity field inside the ring tube is specified as a Gaussian distribution from the core (similar to the vortex pair in section 6.1). In this case, we only focus on three factors: gravity g, surface tension σ/ρ, and Γ, and we study the influences of the three factors on the entrainment volume. By choosing R as the characteristic length scale and Γ/R as the velocity scale, this problem is mainly governed by three non-dimensional parameters: $Fr^2 = \Gamma^2/gR^3$, $We = \Gamma^2/R(\sigma/\rho)$, and $Re = \Gamma/\nu$. Hereafter in this section, all the variables are normalized by Γ and R unless otherwise stated. The domain size is $6 \times 6 \times 6$. The initial flat free surface is at $z = 0$. The water domain is $z \in [-4, 0]$ and the air domain is $z \in [0, 2]$. The boundary conditions are periodic boundary in the horizontal x-y plane and no-flux at the top and bottom of the domain. In this case, a high resolution of 384^3 grids is used to capture complex physics in the entrainment process. An extended discussion is in §6.2.3.

To set up the initial velocity field, we follow the method described in §6.1. We first specify the vorticity field in the computational domain. Next, we solve for the stream function $\boldsymbol{\psi}$. The initial velocity field is obtained by $\boldsymbol{u} = \nabla \times \boldsymbol{\psi}$.

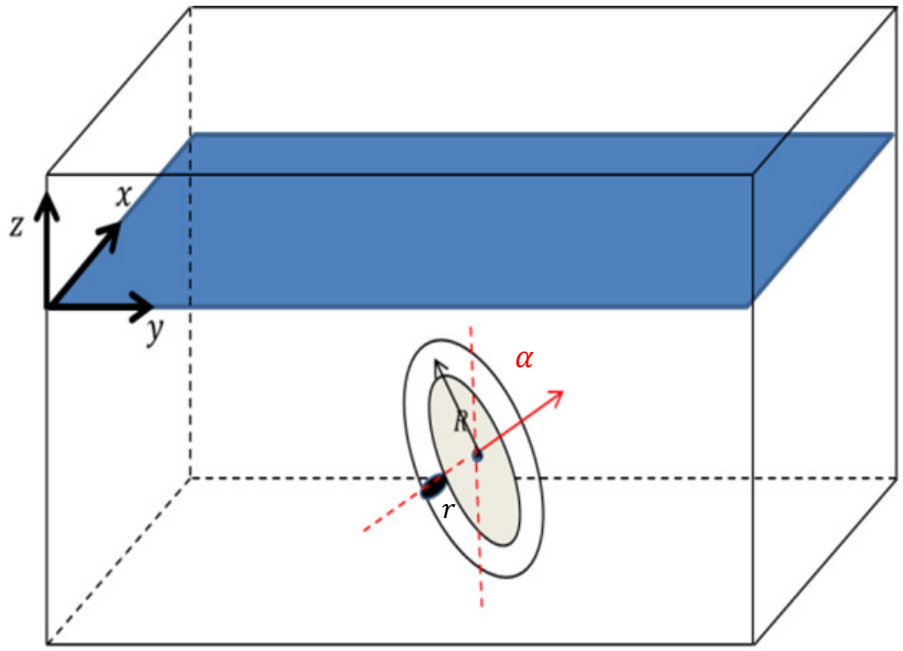

Figure 6-21: Definition sketch showing a free surface present at $z = 0$ with ring-structured vortex with an outer radius R and an inner radius r. The circulation inside the ring tube is Γ and and the inclined angle is α.

6.2.2 Two surface layers under flat free surface

We first investigate the effects of the free surface on the underlying vortex structures during the vortex-surface interaction. We consider a case of $Fr^2 = 0.5$, $We = \infty$, and $Re = 1,000$. Due to the small Fr (relatively strong gravity), gravity effects greatly stabilize the free surface and prevent significant surface deformations. As a consequence, the flat free surface shows strong blockage effects on the underlying vortex ring. Figure 6-22 shows the interacting process of the vortex ring and the free surface. The vortex ring is observed to rise towards the free surface and its head part shows a strong interaction with the free surface. The head part of the vortex disappears quickly, forming a U-shaped vortex structure with two legs connecting to the free surface. This connection process of the vortex ring is consistent with the observation in Zhang *et al.* (1999) and Shen *et al.* (1999). No air entrainment occurs during this process.

Figure 6-23 shows the contour plot of vorticity component in x direction, ω_x, on a y-z plane at $x = 3$ (middle of x dimension) at $t = 4$ when the head part of the vortex ring interacts with free surface. We observe that the free surface shows only local and small deformations during the interaction, and remains nearly flat due to the strong stabilization effects of gravity. At the same time, the deformed surface creates a vorticity field in the air domain.

To further quantify the surface effects on underlying vorticity, we consider a vertical line across the core of the head part of the vortex ring, and plot the vertical profile of vorticity dissipation $\frac{1}{Re}\nabla^2\omega_x$ and vorticity stretching $\omega_x \partial u/\partial x$ of ω_x along the line in figure 6-24 and 6-25. In figure 6-24, we identify an inner layer of thickness of $O(0.1)$ under the free surface where vorticity dissipation of ω_x, $\omega_x \partial u/\partial x$, is enhanced. Notice that the dissipation term $\omega_x \partial u/\partial x$ is positive in the layer since the corresponding ω_x is negative. The enhancement of $\omega_x \partial u/\partial x$ is because of the large vertical gradient of ω_x near the free surface as shown in figure 6-26. Due to the enhanced dissipation, the head part of the vortex ring is dissipated quickly and disappears when interacting with the free surface. In figure 6-25, an outer layer of thickness of $O(0.4)$ is identified

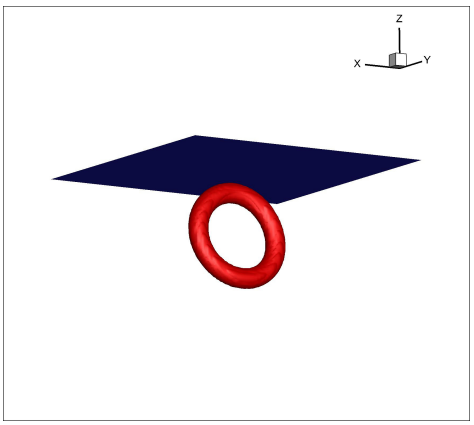

(a)

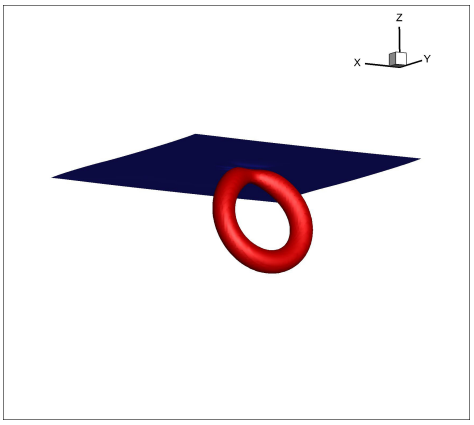

(b)

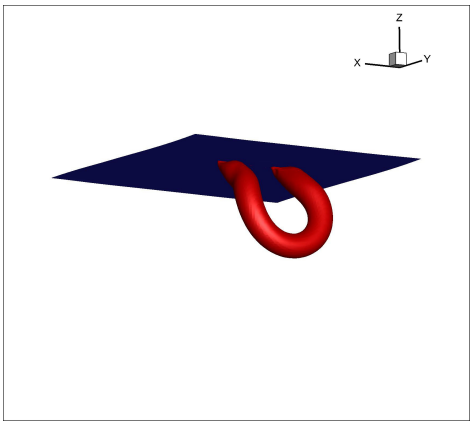

(c)

Figure 6-22: Interaction of a ring-shaped vortex with a flat free surface at different instantaneous times with $Fr^2 = 0.5$ and $We = \infty$. The free surface (Dark blue) is represented by iso-surface of volume fraction $f = 0.5$. The vortex structure (orange) is identified by by $\lambda - 2$ method. (a), t=0; (b), t=8; (c), t=16.

where vorticity stretching of ω_x, $\omega_x \partial u/\partial x$, is enhanced. $\omega_x \partial u/\partial x$ in this outer layer increases the magnitude of ω_x as a production term.

Due to the presence of the two surface layers, ω_x shows a distinguished evolution during the vortex-surface interaction. Figure 6-27 shows the evolution of $|\omega_x|$ at the core of the head part of the vortex ring on the y-z plane defined in figure 6-23. We observe that $|\omega_x|$ decreases initially due to viscous dissipation when it propagates in the bulk to the free surface. As it interacts with the free surface, a plateau behavior is observed. When the head part enters the outer layer, it experiences strong vorticity stretching, which provides production on $|\omega_x|$. As it enters the inner layer, the strong vorticity dissipation causes a rapid reduction of $|\omega_x|$. The observed plateau in figure 6-27 is a consequence of the balance of the two processes. In contrast, $|\omega_x|$ at the core of the bottom part of the vortex ring (on the y-z plane defined in figure 6-23) only experiences viscous dissipation over time and no plateau behavior is observed. As the vortex keeps moving upwards, the strong dissipation near the free surface results in a faster decrease of $|\omega_x|$ at the core of the head part. This explains the disappearance of the head part of the vortex ring during the vortex-surface interaction.

As Fr increases, larger surface deformation is allowed and the surface effects are reduced. To confirm this, a numerical simulation of a case with larger $Fr^2 = 3$ is performed and the numerical results are compared with those of case $Fr^2 = 0.5$ in figure 6-24 $\sim$ 6-26. For the case of $Fr^2 = 3$, instead of the large vertical gradient in the surface layer, the variation of ω_x is observed to be very limited as shown in figure 6-24. The corresponding vorticity dissipation $\frac{1}{Re}\nabla^2\omega_x$ becomes smaller. In the outer layer, the magnitude of vorticity stretching $\omega_x \partial u/\partial x$ in the high Fr case also becomes smaller as shown in figure 6-25.

6.2.3 Air entrainment induced by vortex ring

When Fr^2 further increases to order 10, the surface effects are significantly reduced and strong surface deformations are induced by the vortex ring, leading to substantial air entrainment. We here consider a case with $Fr^2 = 18$, $We = 5000$, and $Re = 1000$. Figure 6-28 shows the process of air entrainment induced by the vortex ring at different

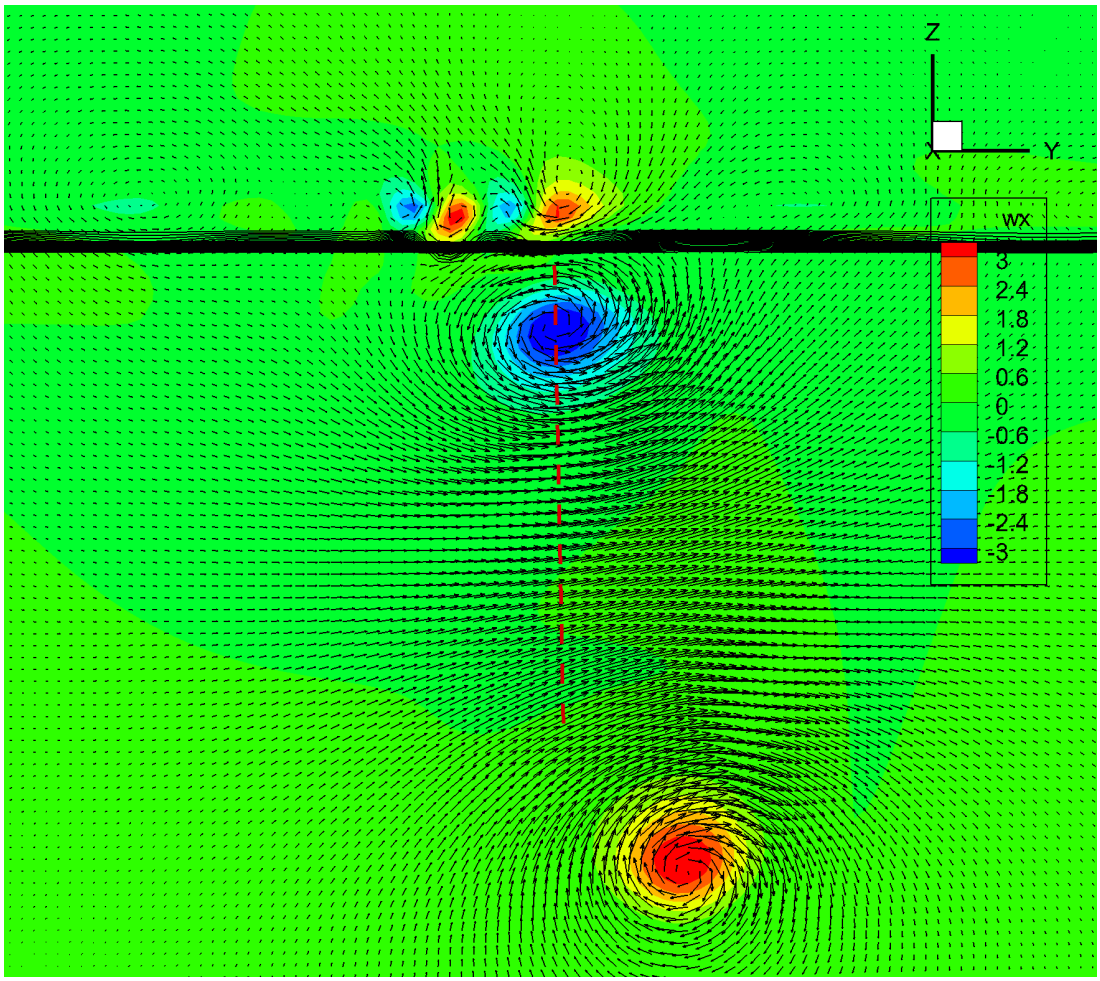

Figure 6-23: Contour plot of vorticity component in x direction, ω_x, on a y-z plane at $x = 3$ (middle of x dimension) at $t = 4$ when the head part of the vortex ring interacts with free surface. The parameters are $Fr^2 = 0.5$, $We = \infty$, and $Re = 1000$. The velocity field is represented using arrows.

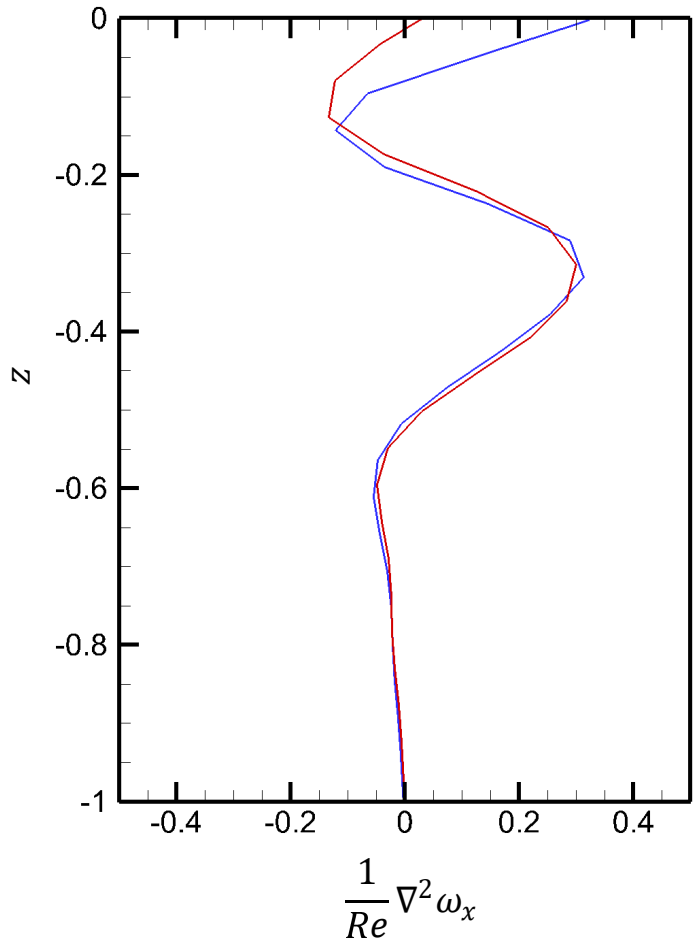

Figure 6-24: Profile of vorticity dissipation of vorticity component ω_x, $\frac{1}{Re}\nabla^2\omega_x$, along the vertical red line defined in figure 6-23. ——, $Fr^2 = 0.5$; ——, $Fr^2 = 3$.

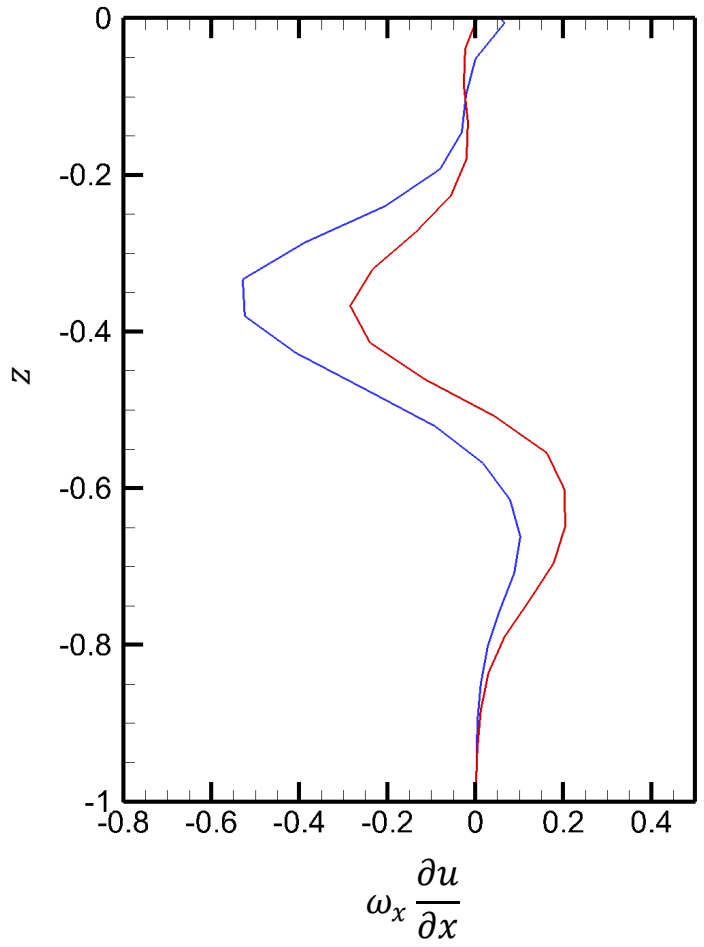

Figure 6-25: Profile of vorticity stretching of vorticity component ω_x, $\omega_x \partial u/\partial x$ of ω_x, along the vertical red line defined in figure 6-23. ——, $Fr^2 = 0.5$; ——, $Fr^2 = 3$.

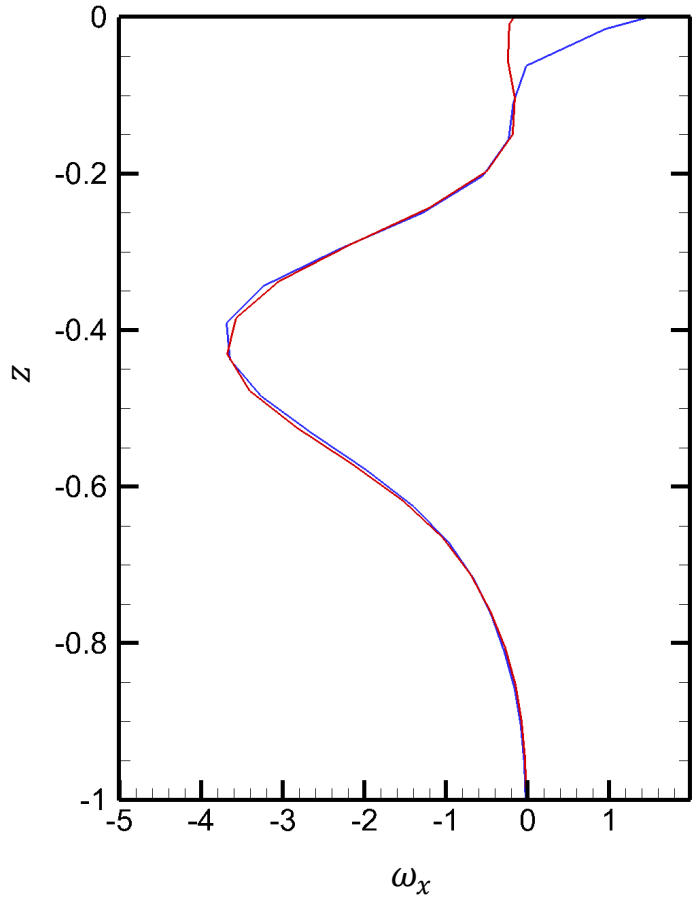

Figure 6-26: Profile of vorticity component ω_x along the vertical red line defined in figure 6-23. ——, $Fr^2 = 0.5$; ——, $Fr^2 = 3$.

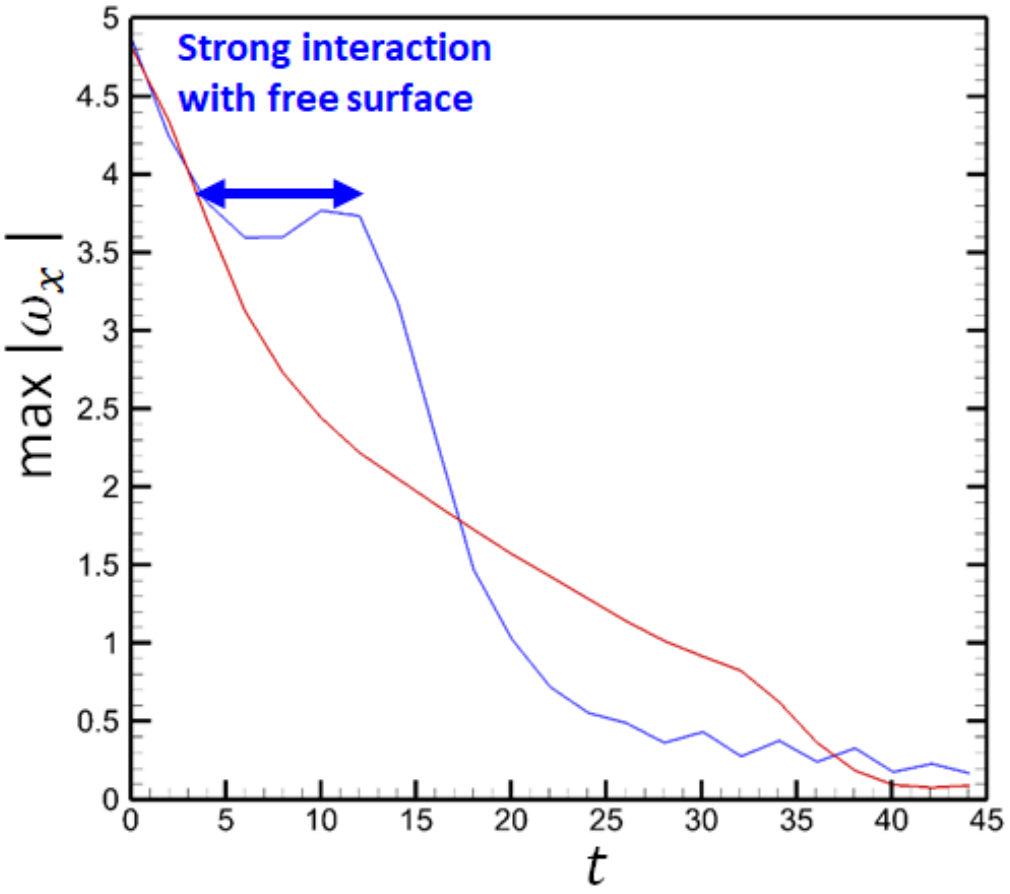

Figure 6-27: Evolution of the magnitude of vorticity component ω_x near the free surface (——) and in the bulk flow (——).

times. As the vortex ring propagates to the free surface, it induces large surface distortion, forming an air tube connecting to the free surface as shown in figure 6-28(a). Notice that no entrained air is identified at this time since the air tube is connected to the air domain. The air tube is stretched and breaks into individual bubbles due to flow instability (see figure 6-28(b) and (c)). The mechanisms of the flow instability involves complex underlying physics and are out of the scope of this thesis. Even through, we argue that surface tension contributes greatly to the breakup process of the air tube. We ensure that the surface tension effects on air entrainment are properly resolved by examining the resolution of the capillary scale ℓ_c, at which $Bo = \rho g \ell_c^2/\sigma = 1$. l_c is equal to 0.06 with the given Fr and We, and is resolved by 4 grid points Δ. After the breakup of the air tube, the created bubbles in the water escape under the buoyancy effect as shown in figure 6-29.

6.2.4 Dependence of air entrainment on Fr, We, and Γ

First of all, we investigate the effect of We by considering three (relative) small $We = 1000, 50000$, and 10000 with a fixed $Fr^2 = 18$. For the three We cases, the corresponding l_c are 0.13, 0.06, and 0.042, resolved by 8, 4, and 3 Δ. Considering the characteristic bubble scale being 4Δ, the effects of We on entrainment are important (relative to Fr). Figure 6-30 shows the time evolution of the total entrainment volume $V(t)$ for the three We cases. The amplitude of $V(t)$ is observed to increase with We. As We increases with other parameters fixed, the stabilization effects of surface tension on the free surface is reduced essentially, resulting in the increase of $V(t)$. In addition, we observe that the breakup time of the air tube, when a large amount of air entrainment is identified with rapid increase of $V(t)$, delays as We increases. For the three We cases, the breakup of the air tube is confirmed to happen at $t = 18$, $t = 28$, and $t = 32$. Figure 6-31 shows the moment of the breakup of the air tube for the three cases. With smaller We, stronger surface tension results in early breakup of the air tube. To quantify the effect of We on air entrainment, figure 6-32 shows the maximum entrainment volume v_{max} as a function of We. It is observed that V_{max} shows a linear dependence on We or $(\sigma/\rho)^{-1}$ when surface tension effects

(a)

(b)

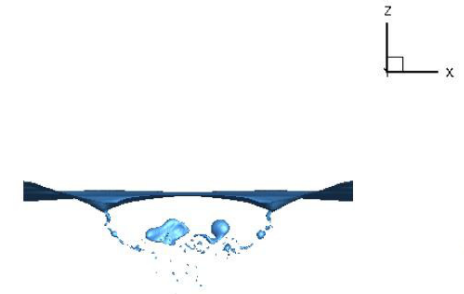

(c)

Figure 6-28: Air entrainment induced by the ring-shaped vortex structure. The free surface is represented by the iso-surface of volume fraction $f = 0.5$. The parameters of the case are $Fr^2 = 18$, $We = 5000$, and $Re = 1000$. (a), t=15; (b), t=25; (c), t=35.

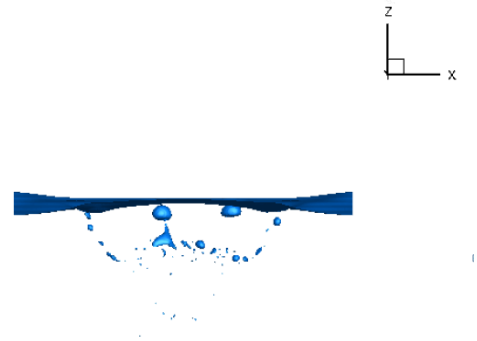

(a)

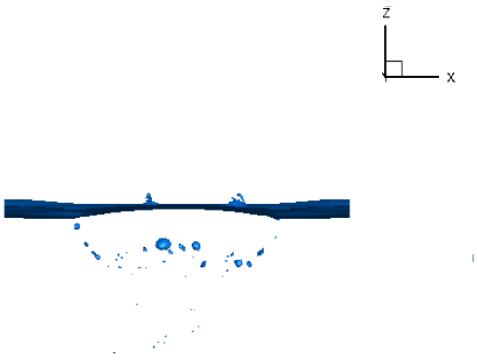

(b)

Figure 6-29: Bubble degassing after entrainment by the vortex ring. The free surface is represented by the iso-surface of volume fraction $f = 0.5$. The parameters of the case are $Fr^2 = 18$, $We = 5000$, and $Re = 1000$. (a), t=45; (b), t=50.

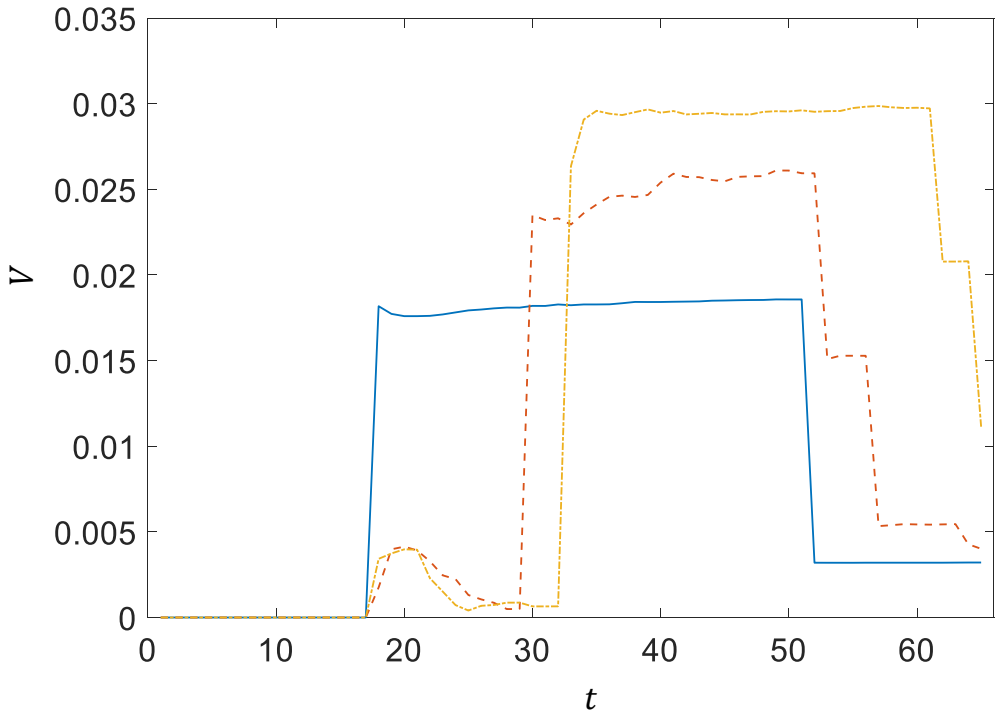

Figure 6-30: Time evolution of total entrainment volume $V(t)$ at different We with $Fr^2 = 18$. ——, $We = 1000$; - - -, $We = 5000$; · · ·, $We = 5000$..

are important (relative to gravity). This is consistent with our observations in FST cases.

Next, we investigate the effect of Fr by considering three (relative) small $Fr^2 = 10, 14$, and 18 with a fixed $We = 10000$. For the three cases, the corresponding l_c are 0.03, 0.037, and 0.042, resolved by 2, 2.5, and 3 Δ. Considering the characteristic bubble scale being 4Δ, the effects of Fr on entrainment are important (relative to We). Figure 6-33 shows the time evolution of $V(t)$ for the three Fr cases. The amplitude of $V(t)$ is observed to increase with Fr. As Fr increases with other parameters fixed, the stabilization effects of gravity on the free surface is reduced essentially, resulting in the increase of $V(t)$. In addition, the breakup time of the air tube delays as Fr increases. A similar delay is observed when different We are considered. However, we point out that the underlying physics are different. With larger Fr, the reduced stabilization effect of gravity results in an air tube with a larger radius as shown in

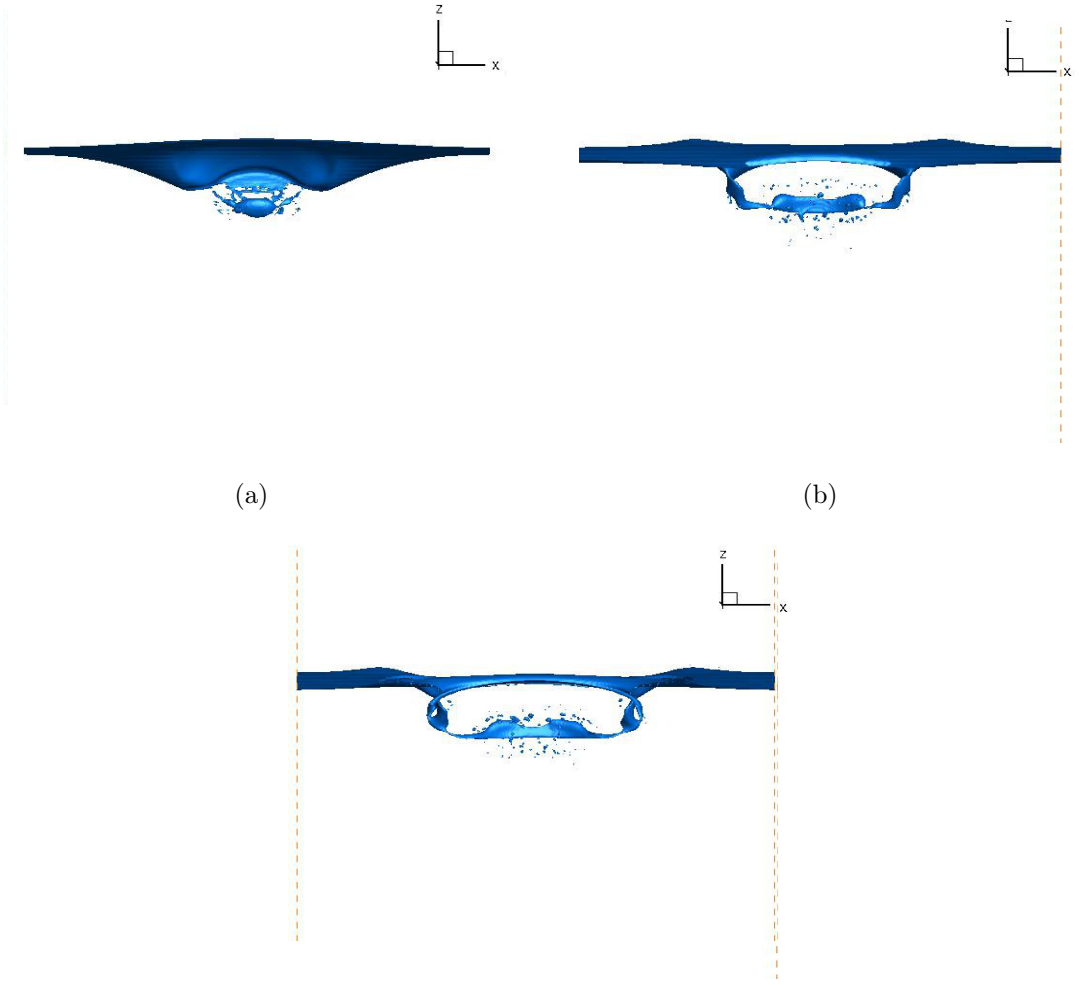

(a) (b)

(c)

Figure 6-31: The moment of breakup of the air tube for the three We cases with $Fr^2 = 18$. The free surface is represented by the iso-surface of volume fraction $f = 0.5$. (a), $We = 1000$; (b), $We = 5000$; (c), $We = 10000$.

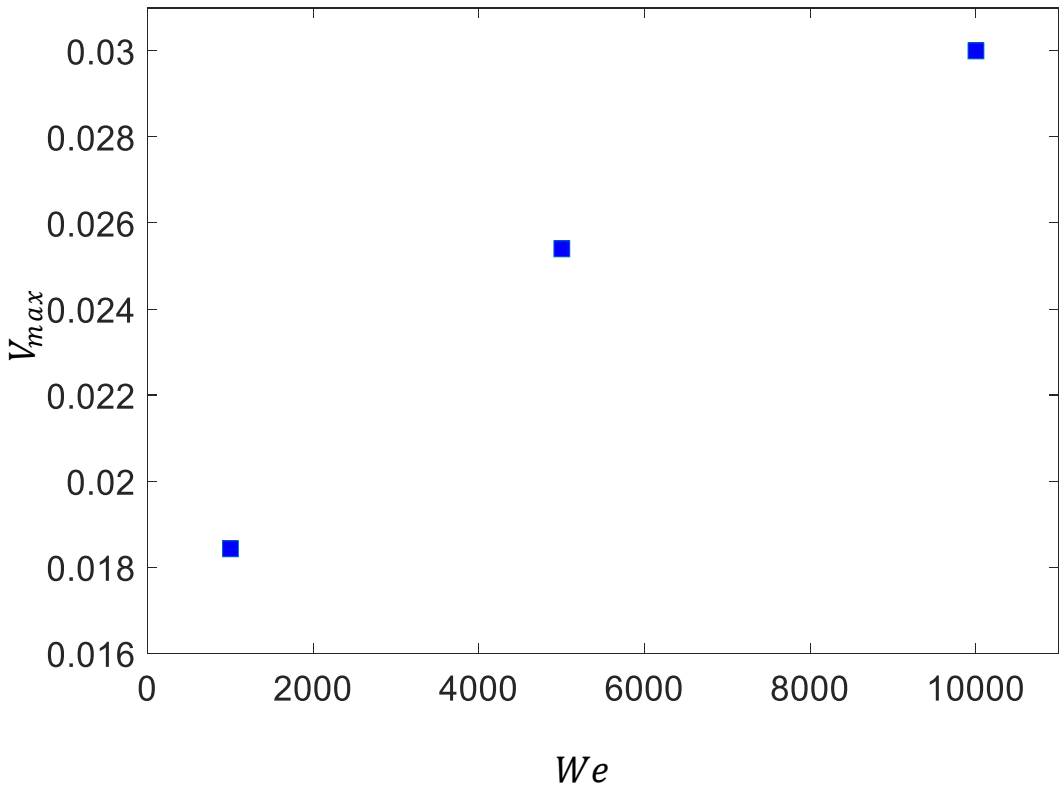

Figure 6-32: Maximum of entrainment volume V_{max} as a function of We with $Fr^2 = 18$.

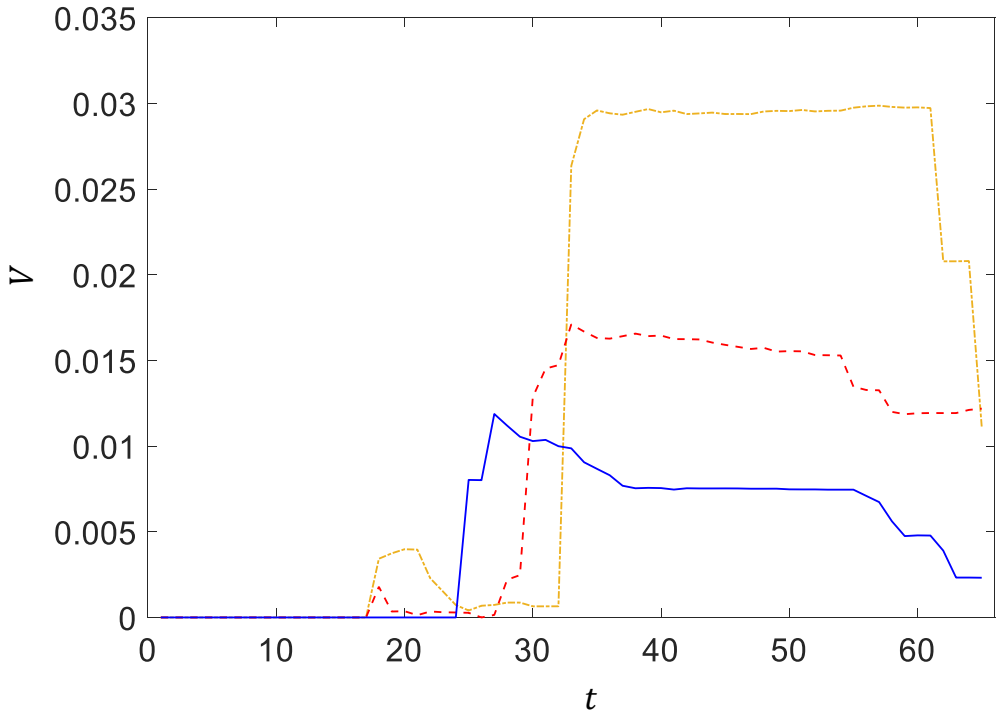

Figure 6-33: Time evolution of total entrainment volume $V(t)$ at different Fr with $We = 10000$. ——, $Fr^2 = 10$; - - -, $Fr^2 = 14$; · · ·, $Fr^2 = 18$.

figure 6-34. The larger air tube experiences a long stretching process until the flow instability breaks it into bubbles. To quantify the effect of Fr on air entrainment, figure 6-35 shows v_{max} as a function of Fr^2. It is observed that V_{max} shows a linear dependence on Fr^2 or g^{-1} when gravity effects are important (relative to surface tension). This is consistent with our observations in FST cases.

Finally, we consider the effect of Γ on air entrainment induced by the vortex ring. The information of the three cases with different Γ is summarized in table 6.6. Figure 6-36 shows the time evolution of $V(t)$ for the three cases. The amplitude of $V(t)$ is observed to increase with Γ. The initial circulation Γ measures the disrupting effect of the vortex structure. As Γ increases with other parameters fixed, the vortex ring contains more energy to induce stronger surface distortions and larger amount of air entrainment. In addition, the breakup time of the air tube delays as Γ increases. The observed delay here shares the similar physics with that in the study of Fr

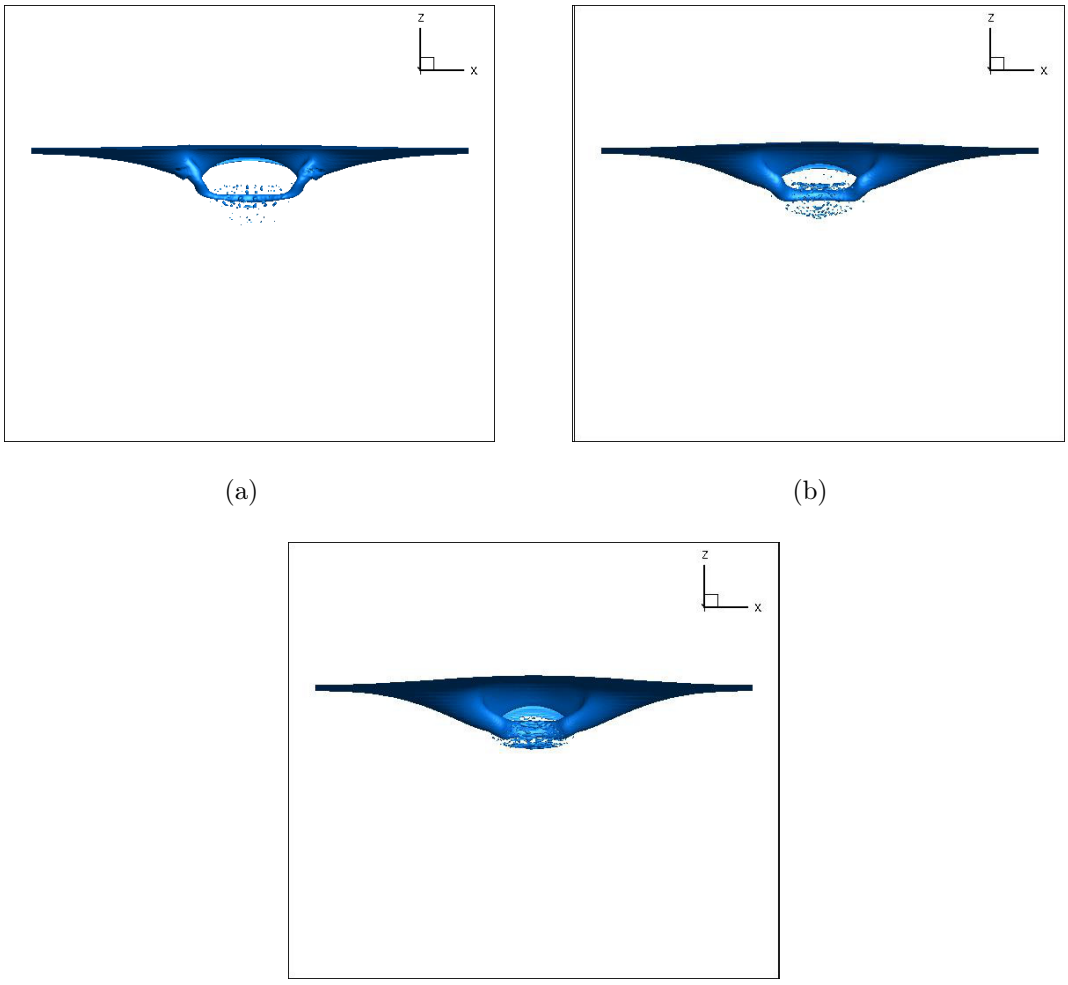

(a) (b)

(c)

Figure 6-34: The moment of air tube formation at $t = 15$ for the three Fr cases with $We = 10000$. The free surface is represented by the iso-surface of volume fraction $f = 0.5$. (a), $Fr^2 = 10$; (b), $Fr^2 = 14$; (c), $Fr^2 = 18$.

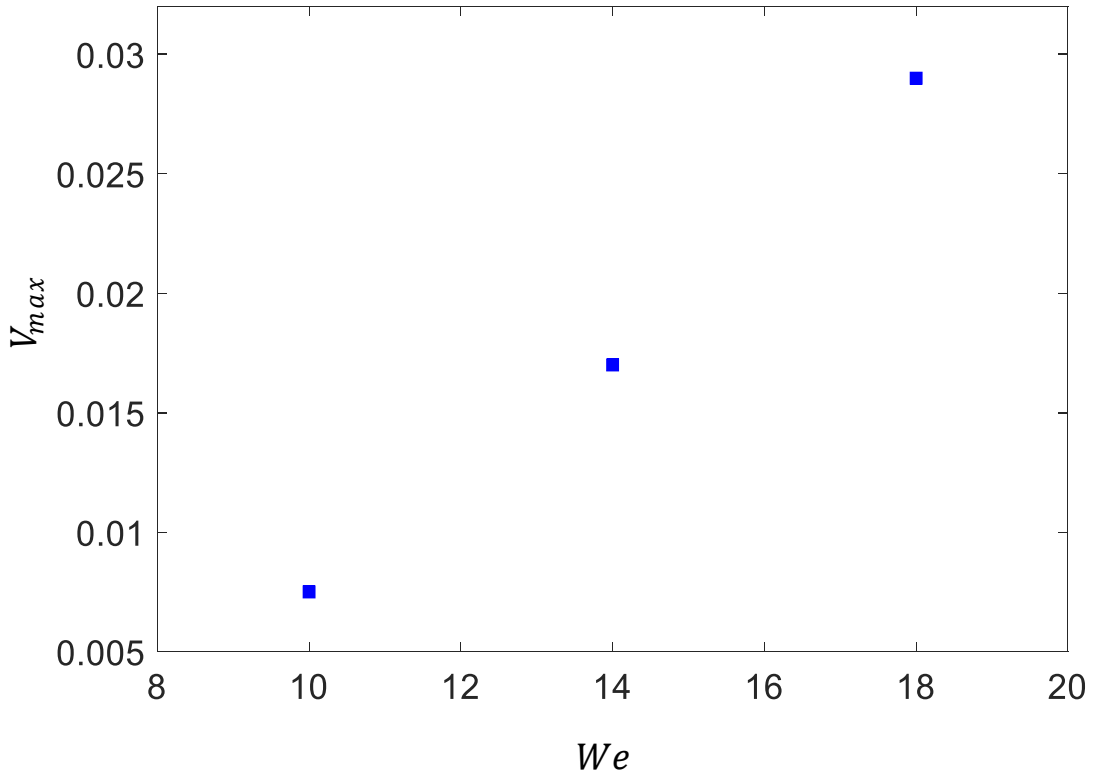

Figure 6-35: Maximum of entrainment volume V_{max} as a function of Fr^2 with $We = 10000$.

Table 6.6: Information of cases considering three different Γ

Γ.	Fr^2	We	Re
1	18	5000	1000
0.8	11.5	3200	800
0.6	6.5	1800	600

effects. Larger Γ induces larger air tube as shown in figure 6-37, which experiences a longer stretching process until the flow instability breaks it into bubbles. Figure 6-38 shows v_{max} as a function of Γ. It is observed that V_{max} increases with Γ and shows a quadratic dependence.

6.3 Summary

In this chapter, we consider air entrainment induced by coherent near-surface vortical structures. We consider two different vortex structures: a pair of counter-rotating vortex tubes and a ring-structured vortex. We perform numerical simulations of the vortex-surface interactions and investigate induced air entrainment. Our objectives are 1) to understand air entrainment induced by vortex-surface interactions and the detailed entrainment process; 2) to study the dependence of vortex induced air entrainment on relevant physical factors; 3) to explore useful averaged quantities for the development of sub-grid air entrainment models.

We start with the canonical problem of the head-on collision of a vortex pair with the free surface. Detailed process of air entrainment induced by the vortex pair is investigated. As the vortex tubes move approaching the free surface, the free surface deforms and forms an anti-splat event with a local trough and a velocity field moving downwards. Later on when the free surface reconnects, an air pocket is enclosed in the water, creating air entrainment. We also study the dependence of air entrainment on relevant physical parameters (gravity g, surface tension σ/ρ, and viscosity ν) and vortex-structure-specific parameters (initial maximum core vorticity ω_c and other geometric parameters). In particular, the linear dependence of the entrainment

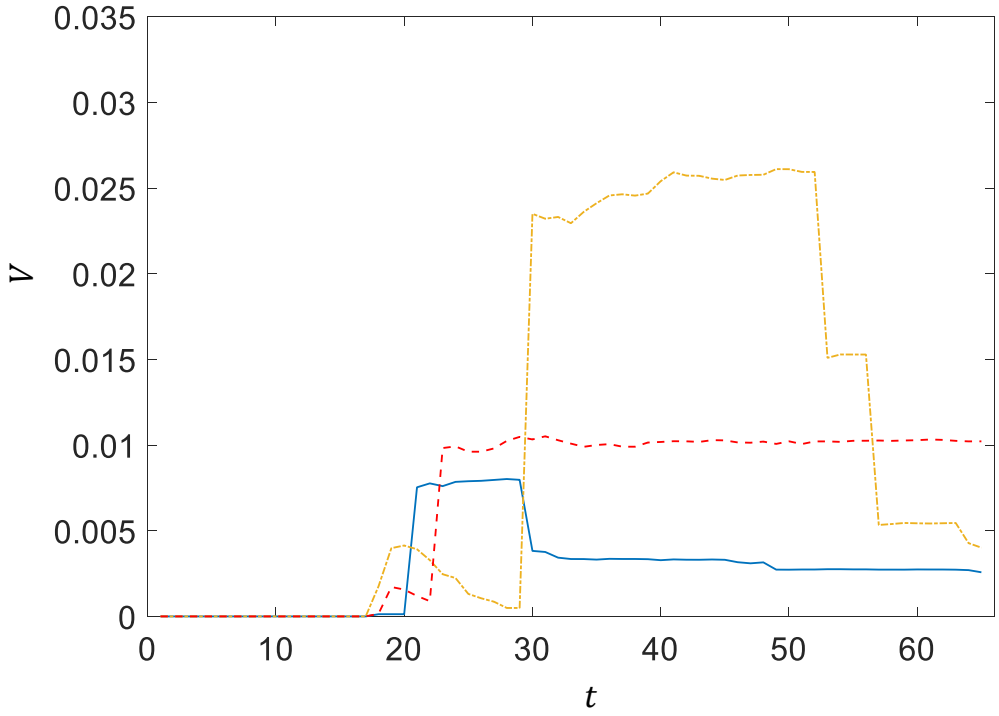

Figure 6-36: Time evolution of total entrainment volume $V(t)$ of different Γ. ——, $\Gamma = 0.6$; - - -, $\Gamma = 0.8$; · · ·, $\Gamma = 1$. The case information is listed in table 6.6

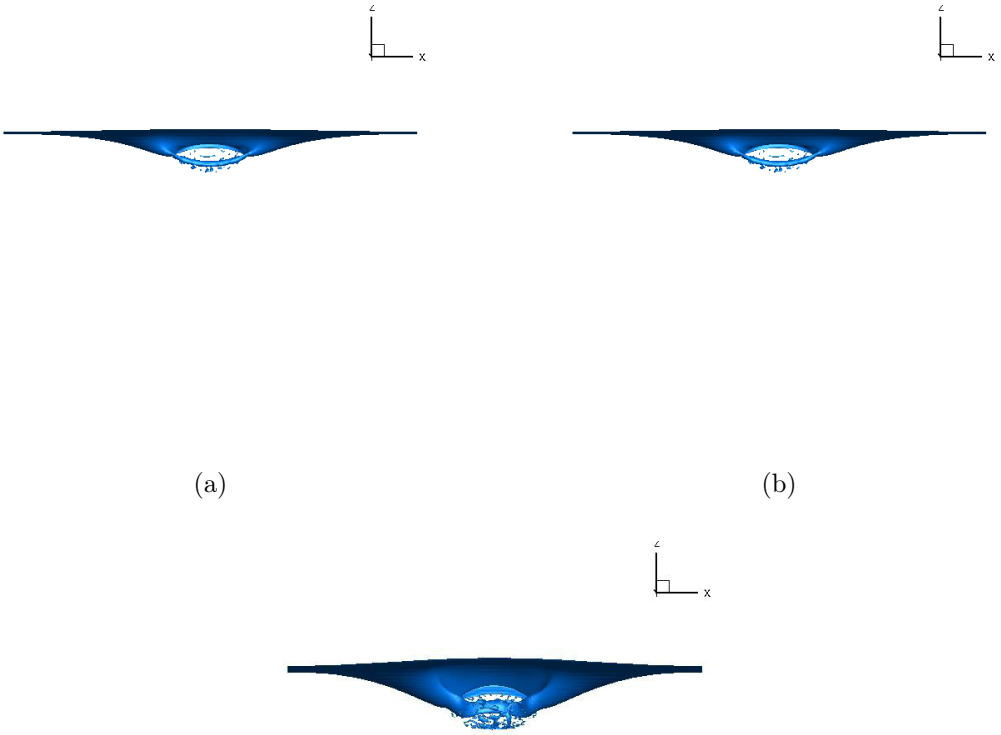

(a) (b)

(c)

Figure 6-37: The moment of air tube formation at $t = 15$ for the three cases with different Γ. The free surface is represented by the iso-surface of volume fraction $f = 0.5$. (a), $\Gamma = 0.6$; (b), $\Gamma = 0.8$; (c), $\Gamma = 1$.

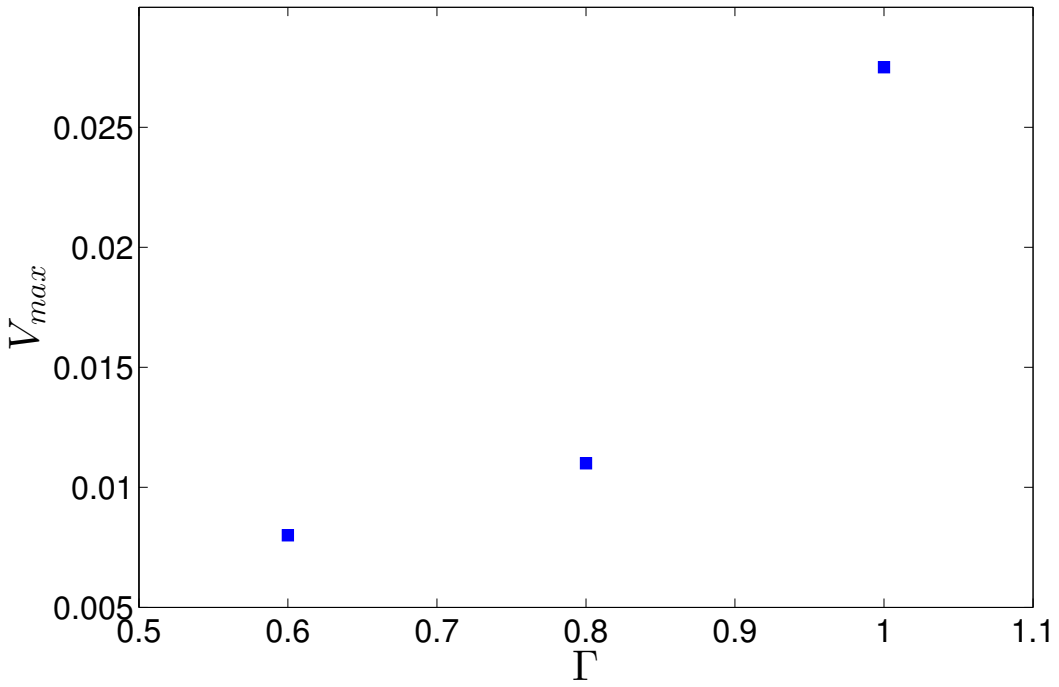

Figure 6-38: Maximum of entrainment volume V_{max} as a function of Γ. The case information is listed in table 6.6.

volume on g^{-1} and $(\sigma/\rho)^{-1}$ obtained in the single vortex induced entrainment event are consistent with those obtained in the SFST flow where numerous entrainment events happen. We also find a linear dependence of the entrainment volume on a quantity of averaged vorticity flux which can be used for modeling of the sub-grid terms of entrainment in RANS to achieve closures.

Then we consider the more realistic three-dimensional vortex ring and its interaction with the free surface. For a flat surface (with small Fr of order 1), the surface effects on the underlying vorticity is found to be strong. Two surface layers are observed under the free surface. In the inner layer, dissipation on the horizontal vorticity component is enhanced. In the outer layer, vorticity stretching on horizontal vorticity is enhanced. When interacting with the flat free surface, the head part of the vortex ring disappears soon due to the strong vorticity dissipation in the inner layer, forming a U-shaped vortex structure with two legs connecting to the free surface. When Fr^2 increases to order 10, large surface distortions are induced and air entrainment

occurs. The detailed entrainment process is investigated. It is observed that an air tube connecting to the air domain is induced by the vortex ring. Then the air tube breaks into individual air bubbles by flow instabilities. Next the dependence of air entrainment on σ/ρ, g, and the initial circulation Γ inside the ring are presented. The linear dependence of the entrainment volume on g^{-1} and $(\sigma/\rho)^{-1}$ are consistent with those obtained in the vortex pair and the SFST flow. We also find that the entrainment volume increases with Γ, but no simple linear dependence is found.

Chapter 7

Conclusions and future work

7.1 Conclusions of thesis

In this thesis, we focus on air entrainment and the resulted bubble size distribution in strong free-surface turbulence (SFST) characterized by large Froude (Fr) and Weber We number. A direct numerical solver is developed for the three-dimensional two-phase incompressible Navier-Stokes equations with a fully nonlinear interface resolved by the conservative volume-of-fluid method (cVOF). We perform direct numerical simulation(s) (DNS) of a canonical FST flow with turbulent kinetic energy supplied by a sheared underlying bulk water flow over a range of Fr and We with a fixed Reynolds number $Re \sim O(1000)$ to 1) characterize the unique characteristics of SFST 2) quantify the entrainment volume and the corresponding size distribution of SFST air entrainment; 3) elucidate the mechanisms/physics of SFST air entrainment.

We qualitatively elucidate the distinct characteristics of SFST versus weak free-surface turbulence (WFST). We perform DNS of both a WFST case with $Fr^2 = 0.5$ and a SFST case with $Fr^2 = 10$. Both the two cases are under negligible surface tension effects by choosing $We = \infty$. For the WFST case, the near-surface flow is characterized by the presence of an inner surface and outer blockage layers, resulting in strong anisotropy of the FST. Furthermore, free surface displacements/disturbances are small and no air entrainment is observed. In contrast, for the SFST case, the free surface is strongly distorted by turbulence with significant displacements, distortions

and, ultimately, break-up of the interface. In the underlying flow, the surface and blockage layers weaken and disappear, and the FST becomes almost isotropic. We document the latter by quantifying the anisotropy tensor b_{ij} and an isotropic parameter J of the SFST. We also find that the corresponding turbulence energy spectrum follows approximately the $k^{-5/3}$ Kolmogorov spectra of isotropic turbulence.

In the SFST case, the free surface is characterized by large distortions and surface breakup, which leads to substantial air entrainment. To obtain the statistics of size distribution of the entrained bubbles, we develop a cavity/bubble identification scheme based on the union-find algorithm to identify individual entrained bubbles in the bulk flow, with which we are ale to calculate the corresponding bubble size spectrum $N_a(r)$ as well as the entrainment volume V. In general, $N_a(r)$ is a consequence of three main processes: entrainment by SFST, bubble fragmentation by turbulence and degassing. During the entrainment period when the entrainment rate $Q = \dot{V}$ remains positive, SFST entrainment is found to occur over a broad range of scales. With $We = \infty$, $N_a(r)$ shows a $r^{-10/3}$ power-law at the early stage of the entrainment period before significant bubble fragmentation happens. As the entrainment process continues accompanied by the fragmentation of already entrained air, $N_a(r)$ deviates from the initial power-law. Incorporating the evolution of the size spectrum of an initial population of bubbles in IHT, we provide a heuristic model that qualitatively matches and explains the salient evolution behavior of $N_a(r)$ obtained from DNS. The bubble degassing is confirmed to be negligible during the entrainment period.

In this thesis, we specifically focus on SFST entrainment and the corresponding entrainment bubble size spectrum $\mathcal{N}_a^E(r)$ which is to be distinguished from $N_a(r)$ in the bulk. To elucidate the underlying mechanisms, a new model considering $\mathcal{N}_a^E(r)$ of SFST entrainment is derived in this thesis. We provide a detailed physical/mechanistic derivation by connecting the energy of turbulence and the energy required for bubble entrainment/formation, as well as a direct dimensional argument for the model. The model predicts two distinct regimes of $\mathcal{N}_a^E(r)$ depending on bubble radius r. The two regimes are separated by the capillary length scale r_c. The model predicts that $\mathcal{N}_a^E(r) \propto g^{-1}\epsilon^{2/3}r^{-10/3}$ in the regime of $r > r_c$, where entrainment of the

bubbles is under strong effects of gravity g (relative to surface tension σ). ϵ is turbulence dissipation. In the regime of $r < r_c$, surface tension effects are more important for entrainment of the bubbles and the model gives that $\mathcal{N}_a^E(r) \propto (\sigma/\rho)^{-1}\epsilon^{2/3}r^{-4/3}$. The model provides physical explanations for the bubble size distribution of SFST air entrainment for the first time. According to the model, the two regimes corresponds to important or unimportant of surface tension relative to gravity for the entrainment of bubbles. The power-law behavior in each regime is a direct result of the power-law energy spectrum of near-surface turbulence which drives air entrainment. Relevant length scales of SFST entrainment and their potential influences on $\mathcal{N}_a^E(r)$ are discussed in great detail. We argue that there exist a lower and an upper bound of entrained bubble size. The explicit expressions of the two bounds are derived. The bubble size range is argued to become wider with increasing ϵ. Furthermore, a critical value ϵ_{cr} is obtained, blow which no air entrainment can happen. For air-water interface and earth gravity, ϵ_{cr} is a constant. Based on these theoretical investigations, we propose a diagram of (r, ϵ)-plane to describe air entrainment in FST.

Then we perform a series of DNS of the canonical FST flow over ranges of Fr and We to confirm the predictions of our new model of $\mathcal{N}_a^E(r)$. We measured the bulk bubble size spectrum $N_a(r)$ from DNS results to imply $\mathcal{N}_a^E(r)$ and to understand its behaviors. High fidelity DNS results confirm the existence of the two regimes of $\mathcal{N}_a^E(r)$ and the corresponding power-laws with respect to r. The scale separating the two regimes is confirmed to be r_c. We also investigate the dependence of SFST air entrainment on g, σ, and ϵ through DNS of the canonical flow. We find that the averaged entrainment rate $\overline{Q}_{\mathcal{E}}$ and the magnitude of averaged increase rate of $N_a(r)$, $\overline{Q}_{\mathcal{N}}(r)$, show a linear dependence on g^{-1} for the entrainment of bubbles under strong gravity effects relative to surface tension. These results imply the scaling dependence of $\mathcal{N}_a^E(r) \propto g^{-1}$. For the entrainment of bubbles under strong surface tension effects, both $\overline{Q}_{\mathcal{E}}$ and $\overline{Q}_{\mathcal{N}}(r)$ show a linear dependence on $(\sigma/\rho)^{-1}$, implying $\mathcal{N}_a^E(r) \propto \sigma/\rho)^{-1}$. We also study the influence of near-surface dissipation ϵ, which measures the turbulence disrupting effect on the free surface, on SFST entrainment. The DNS results indicate that $\mathcal{N}_a^E(r) \propto \epsilon^{2/3}$. We analyze the results of several DNS

cases and mark the corresponding data points on the diagram of (r, ϵ)-plane. All the cases with/without air entrainment correctly fall in the regime of strong/weak free-surface turbulence regime.

In SFST, coherent vortical structures near the free surface are observed to induce entrainment events. In the last part of this thesis, we study air entrainment induced by near-surface vortex structures. We first consider a problem of the head-on collision of a pair of counter-rotating vortex tubes with the free surface and perform numerical simulations to investigate the corresponding induced entrainment processes. As the vortex tubes move approaching the free surface, the free surface deforms and forms an anti-splat event with a local trough and a velocity field moving downwards. Later on when the free surface reconnects, an air pocket is enclosed in the water, creating air entrainment. We also study the dependence of the entrainment volume V on relevant physical parameters (gravity, surface tension, and viscosity) and vortex-structure-specific parameters (initial core vorticity and tube radius) in great detail. In particular, V shows a linear dependence on g^{-1} when the entrainment process is under strong gravity effects. V shows a linear dependence of σ^{-1} when surface tension effects are more important. The two dependencies obtained in the single entrainment event induced by the vortex pair are consistent with those obtained in the SFST flow where numerous entrainment events happen. In addition, we find a linear dependence of V on an averaged quantity of vertical vorticity flux which can be used for modeling of the sub-grid terms of entrainment in RANS to achieve closures. We also consider a three-dimensional ring-structured vortex, as an approximation of the realistic Ω-shaped vortex observed in the SFST flow. For a flat surface (with small Fr number of order 1), the surface effects on the underlying vorticity is found to be strong. Two surface layers are observed under the free surface. In the inner layer, dissipation on horizontal vorticity components is enhanced. In the outer layer, vorticity stretching on horizontal vorticity is strong. When interacting with the flat free surface, the head part of the ring disappears soon due to the strong vorticity dissipation in the inner layer, forming a U-shaped vortex structure with two legs connecting to the free surface. When Fr^2 increases to order 10, large surface distortions are induced and air

entrainment occurs. The detailed entrainment process is investigated. It is observed that an air tube connecting to the air domain is induced by the vortex ring. Then the air tube breaks into individual air bubbles by flow instabilities. The dependence of V on g and σ in this case remain the same with ones we observe in the vortex pair case. In addition, we find that V increases with the initial circulation Γ inside the ring , but no simple linear dependence is found.

In this thesis, we perform both numerical and theoretical studies on air entrainment and the bubble size distribution in strong free-surface turbulence (SFST) at (relative) large Froude and Weber number. The thesis work elucidates the key mechanisms/physics of the bubble size distribution of SFST entrainment for the first time, and provides useful insight and guidance to the development of sub-grid air entrainment models.

7.2 Future work

In the thesis, we provide theoretical and numerical studies on air entrainment in SFST. However, the story is far more than the end. Future research is necessary.

First of all, for the bubble size spectrum of SFST entrainment, there exit two regimes depending on the bubble radius. Our theoretical model indicates that the scale separating the two regimes is the capillary length scale instead of the Hinze scale as is generally believed. This argument is supported by the results of the high-resolution DNS. Even though, it is necessary to conduct more experimental measurements to further confirm the venality of this point. Potential research in the future includes:

- Vary turbulence dissipation rate ϵ in FST flows and measure the bubble size spectrum. The separating point of the two regimes should always happen at $1.5mm$, which is the capillary length scale with air-water interface and earth gravity. The Hinze scale, instead, changes with ϵ.

- Consider air entrainment in stratified flows, in which the surface tension and

the effective gravity can be changed. The separating point of the two regimes should change accordingly.

Second, we discuss the lower bound r_l and upper bound r_u of the entrained bubble size. For instance, r_l is derived to have an expression of $r_l = 2^{-8/5}(\sigma/\rho We_l)^{3/5}\epsilon^{-2/5}$, where We_l is a constant $\ll 1$ and is argued to be of order $O(0.1)$. For r_u, a constant Fr_u is involved in the expression of r_u. These two constants need to be determined by experimental measurements or numerical simulations. In addition, we derive a critical ϵ_{cr} below which no air entrainment happens. $\epsilon_c = C_\epsilon g^{5/4}(\sigma/\rho)^{1/4}$ is believed to be a constant with given σ/ρ and g. This value needs to be measured for air-water interface and earth gravity. In addition, by considering stratified flows, potential research can be done to confirm the expression of ϵ_c.

Third, we qualitatively confirm that bubble fragmentation causes the evolution of the bubble size spectrum in the bulk. Potential physical processes and scenarios of bubble fragmentation in turbulence are discussed in Chapter 4. Further research is necessary to improve our understanding in these processes. In addition, the exact influences of bubble fragmentation on bubble size distribution, especially the role played by the Hinze scale, need to be quantified.

Finally, in the last part of the thesis, we investigate air entrainment induced by coherent vortex structures. We introduce an averaged quantity of vorticity flux that can be used for modelling sub-grid entrainment terms in two-phase RANS equations. However, this is the very first step. Further research is necessary to mainly address the following two issues.

- For a complete closure model for sub-grid entrainment terms, it should be able to predict the entrainment rate and location in FST flows. Our current research suggests that the quantity vorticity flux near the free surface is a potential key variable that should be considered in such a model. However, how to incorporate this quantity into the model and whether extra quantities should be included in the model are the two main remaining questions. To answer them, future studies becomes necessary.

- In the study of the air entrainment induced by a vortex pair, we find that the entrainment process is affected by the alignment angle θ of the vortex pair. In fact, with non-zero θ, a strong horizontal velocity at the free surface is induced, which favors surface reconnection and air entrainment. How to quantitatively incorporate this complex effect of the free surface deformation on air entrainment remains a challenging and open question.

Appendix A

Ensemble average and statistical error in the mean of DNS data

The DNS data of the canonical FST flow presented in this thesis represents a single realization with a particular initial perturbation. Statistical analysis (Morales *et al.*, 1990) of the cases using this initial perturbation obtains that the maximum error in the mean is less than 4%. To establish the independence of the data from the initial perturbation, we perform additional 4 simulations of the SFST case in Chapter 3 with Fr^2=10 and $We = \infty$. We find that all of the turbulence and air entrainment quantities show similar behavior and statistics. For example, figure A-1 shows the evolution of the turbulent kinetic energy $\frac{1}{2}\langle q^2 \rangle_\delta$ and entrainment volume $V(t)$, using ensemble average. Therefore, the data from the single simulation is representative of the ensemble average.

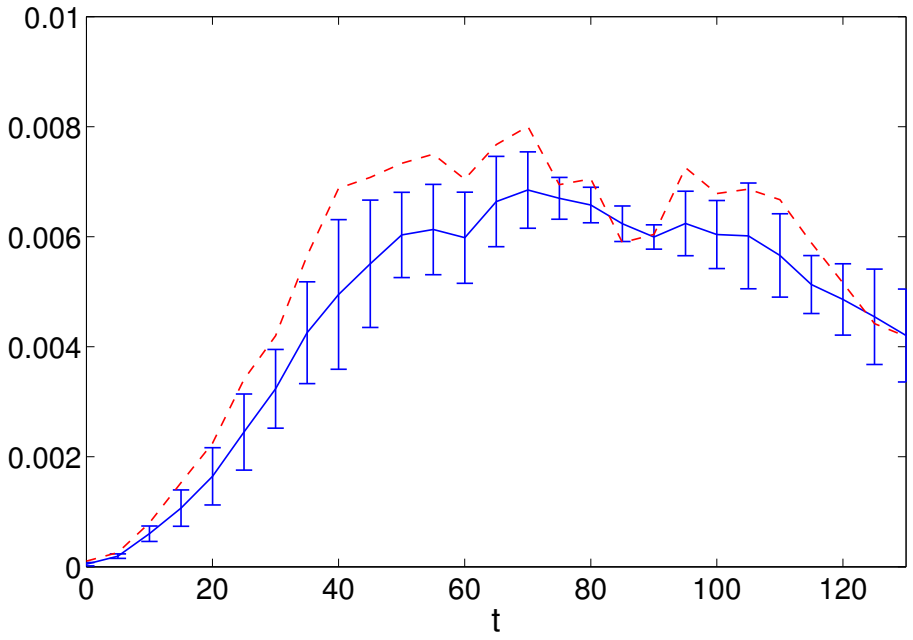

(a)

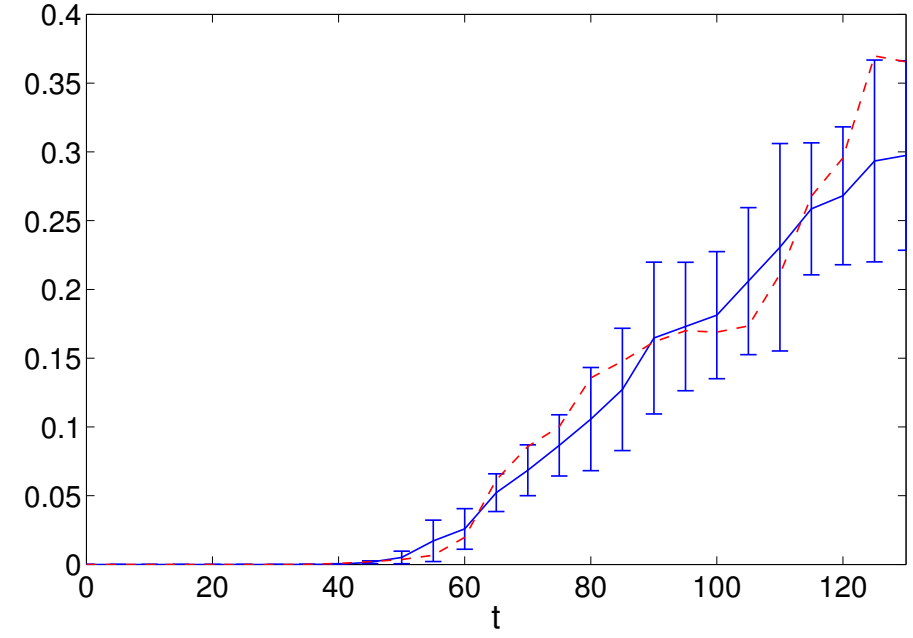

(b)

Figure A-1: Evolution of (a) turbulent kinetic energy $\frac{1}{2}\langle q^2 \rangle_\delta$ and (b) total entrainment volume $V(t)$ of the canonical FST flow. — ensemble average of 5 different initial perturbations with error bar identifying one standard deviation; - - - data from the single perturbation presented in this thesis.

Appendix B

Bubble fragmentation in isotropic homogeneous turbulence

In this appendix, we consider the case of the fragmentation of a prescribed bubble field in isotropic homogenous turbulence (IHT). Initially, a one-phase DNS is simulated using white noise as an initial condition. The computational domain is a cube of length $3L$, where L is a length scale used for normalization. The domain is triply periodic with a resolution of 128^3. As the flow evolves, the initial white noise field evolves to an IHT field. Figure B-2 shows the one-dimensional energy spectrum $E_{ii}(k)$ of the developed IHT. The magnitude of E_{11}, E_{22} and E_{33} plots are comparable with each other and follow the expected $k^{-5/3}$ power-law. Once the IHT is established, we introduce a bubble field and apply linear forcing (Lundgren, 2003) to maintain the turbulent energy in the field. The initial bubble field consists of two hundred randomly placed bubbles sampled from a prescribed size spectrum of $N_a(r) \propto r^{-10/3}$. The possible intersections of sampled bubbles are checked and avoided. The range of the bubble size is between $0.1k\eta$ and $0.5k\eta$, corresponding to the horizontal axis in figure B-2, which has an overlap with the inertial subrange of IHT. Figure B-1 shows the initial bubble population in the domain. The bubbles are introduced with the velocity filed intact so that the velocity field still satisfies continuity. In addition, the total void fraction of the bubbles is small, less than 1%. Thus, the basic characteristics of the IHT field remain unaffected (Garrett *et al.*, 2000). The correct

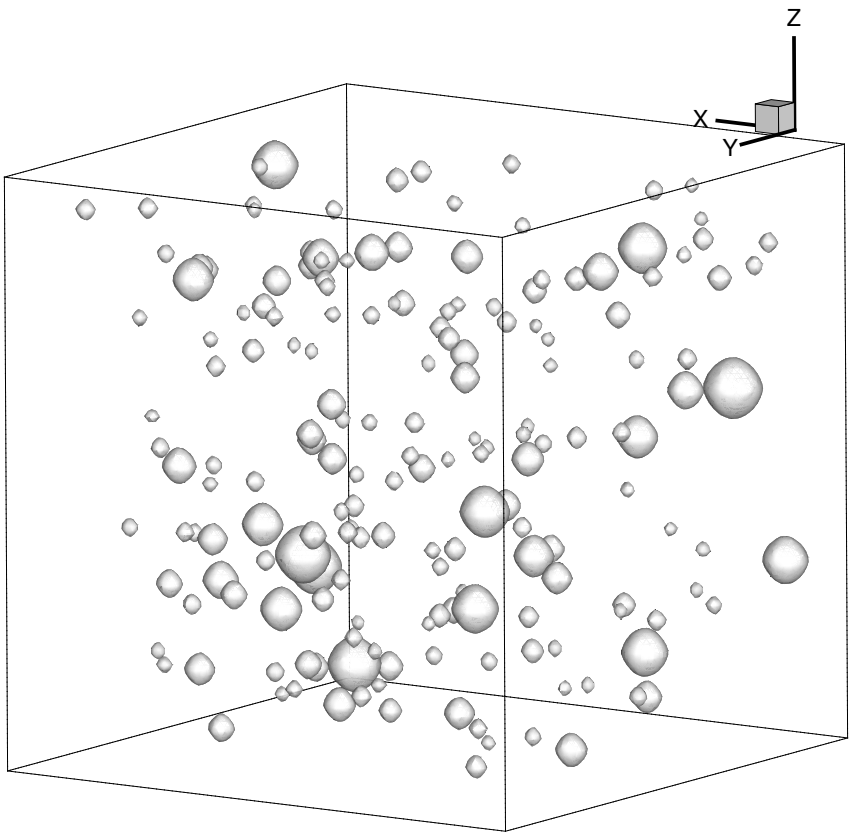

Figure B-1: Initial air bubbles, represented by iso-surface of volume fraction $f = 0.5$, in the case of bubble fragmentation in isotropic homogenous turbulence field. The bubbles follow a bubble size spectrum of $N_a(r) \propto r^{-10/3}$

interfacial conditions are imposed by the cVOF method when the simulation starts. The Reynolds number, the range of bubble size, total void fraction and turbulence intensity are chosen to match the SFST case. Gravity and surface tension effects are not included. With negligible surface tension, the bubble formation dynamics are governed by turbulence fluctuations, in which case bubbles fragment nearly freely in turbulence until the Kolmogorov scale.

Figure B-3 shows $N_a(r)$ at $t = 0$ and $t = 10$. Under the effect of turbulence fragmentation, large bubbles are broken into smaller bubbles, resulting in the decrease of the number of large bubbles and the increase of the number of small ones. At both $t = 0$ and $t = 10$, $N_a(r)$ exhibits a power-law behavior $N_a(r) \propto r^{-\beta}$, but with different

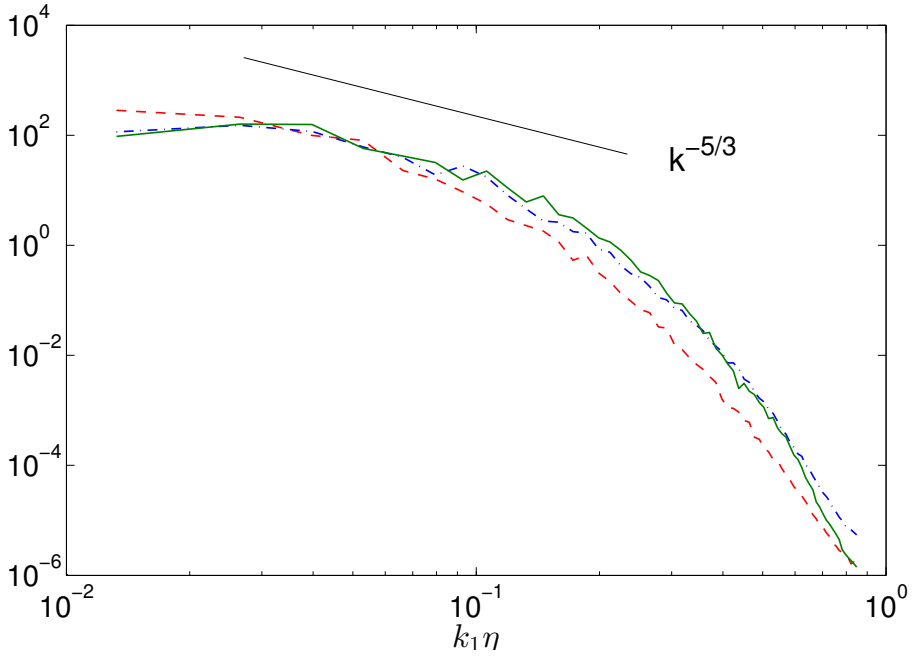

Figure B-2: One-dimensional energy spectrum $E_{11}(k_1)$ - - -, $E_{22}(k_1)$ — · —, $E_{33}(k_1)$ —— of the initial IHT of the bubble fragmentation in IHT case.

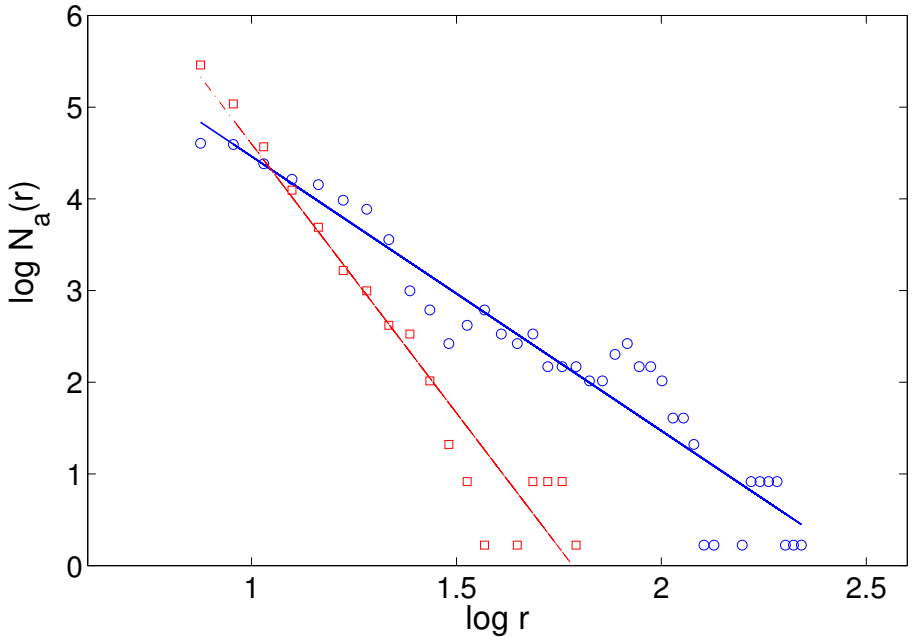

Figure B-3: Bubble size spectrum $N_a(r)$ as a function of r of the bubbles in IHT field at $t = 0$ (○), and $t = 10$ (□). Lines are fitted lines of the original data: —— $N_a(r) \propto r^{-3.0}$ and — · — $N_a(r) \propto r^{-5.9}$.

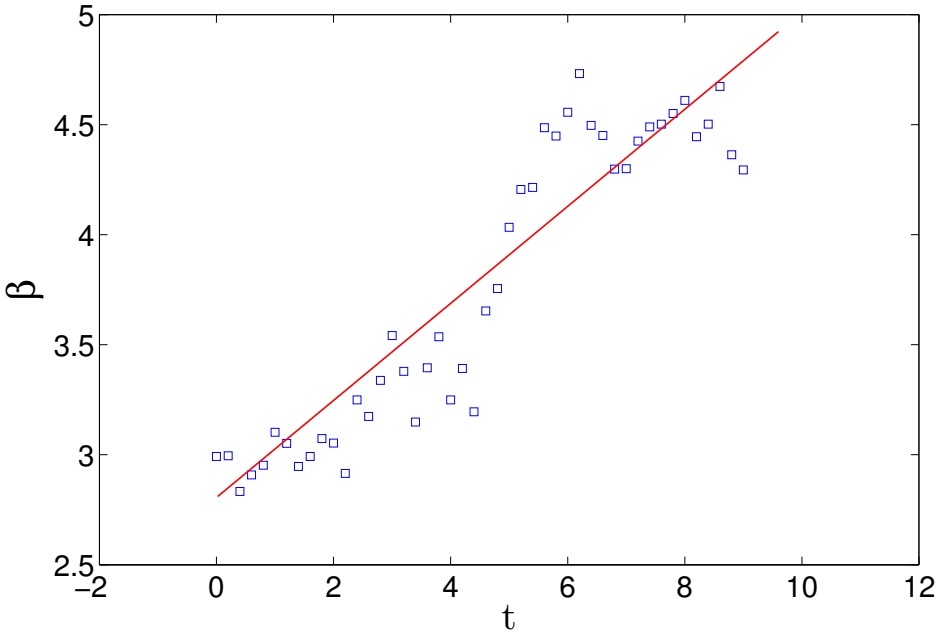

Figure B-4: The value of β as a function of time, where β is a positive number of the power-law $N_a(r) \propto r^{-\beta}$ in the case of bubble fragmentation in IHT . —— linear fitting of the original data.

values of β. At $t = 0$, the fitted value of $\beta \approx 3$. The deviation from the prescribed slope of $\beta = 10/3$ is introduced by the inherent randomness of the sampling method due to the relatively small number of sampled bubbles. However, this number is limited by the DNS domain size, the resolution and the desired (small) void fraction. With greater numbers of sampled bubbles, the bubble seeding procedure correctly obtains the prescribed $r^{-10/3}$ slope. At $t = 10$, the value of β becomes 5.9 by data fitting. Figure B-4 plots the (increasing) value of β as a function of time obtained from this simulation. For simplicity and future reference (§3.3), a simple linear model $\beta(t) = at+b$, with $a \approx$0.24 (R-square$\approx$0.8), is used to approximate the time evolution of β in figure B-4. It is worth of noticing that the linear model is not proposed for a predictive model. Instead, we attempt to propose a simple approximation to quantify the influence of bubble fragmentation on the evolution of bubble size spectrum. In §3.3, this approximation is combined with the one of the continuous entrainment process to justify the evolution of $N_a(r)$ shown in figure 3-16.

Appendix C

Effects of Fr and We on free surface deformation

Both gravity and surface tension have the effects of stabilizing the free surface, but their effects are effective at different length scales. Here, we perform DNS of the canonical FST flow in Chapter 3 and investigate the effects of Fr and We on the deformation of the free surface. The effect of gravity is of importance at the whole range of length scales, while surface tension is at small length scales. To demonstrate this, the energy spectrum of the free surface height $E_{\eta\eta}(k_1)$ at different Fr and We are presented in figure C-1 and C-2. Figure C-1 shows $E_{\eta\eta}(k_1)$ at four different Fr ($Fr^2 = 0.5$, 3, 8, and 14) for $We = \infty$. The value of $E_{\eta\eta}(k_1)$ over the whole range of k is observed to increases with Fr. This suggests that the free surface is more free to deform when the effect of gravity becomes weaker. And the effect of gravity is effective at the free surface deformations with length scale over the whole range. In figure C-2, $E_{\eta\eta}(k_1)$ at four different We (We = 1000, 4000, 10000, and ∞) for $Fr^2 = 10$ are shown. Only notable increases of $E_{\eta\eta}(k_1)$ are observed at large k when We increases. Different than gravity, the effect of surface tension is more effective at the small scaled deformations of the free surface. With strong surface tension, these small scaled deformations are largely suppressed. Figure C-3(a) presents the time evolution of the averaged curvature of the free surface $\langle\kappa^2\rangle^{1/2}$ at the four different We for $Fr^2 = 10$. $\langle\kappa^2\rangle^{1/2}$ is a representative quantity of small scaled deformations of the free surface.

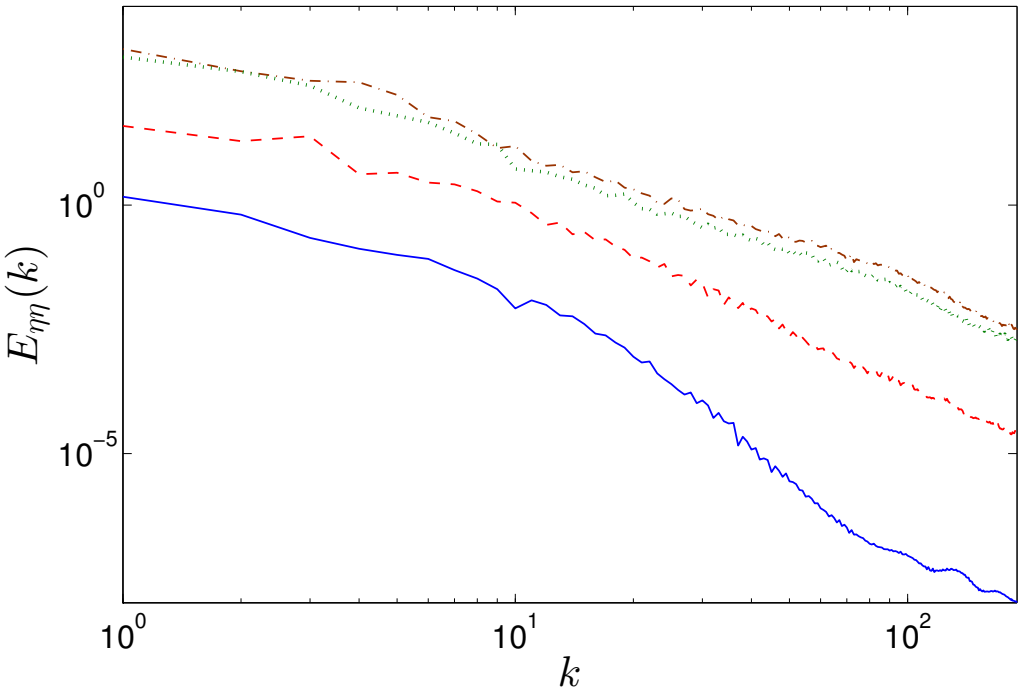

Figure C-1: Energy spectrum of the free surface height $E_{\eta\eta}(k_1)$ as a function of k at different Fr for $We = \infty$ at $t = 80$. Solid, $Fr^2 = 0.5$; Dash, $Fr^2 = 3$; Dotted, $Fr^2 = 8$; Dash-dot, $Fr^2 = 14$;

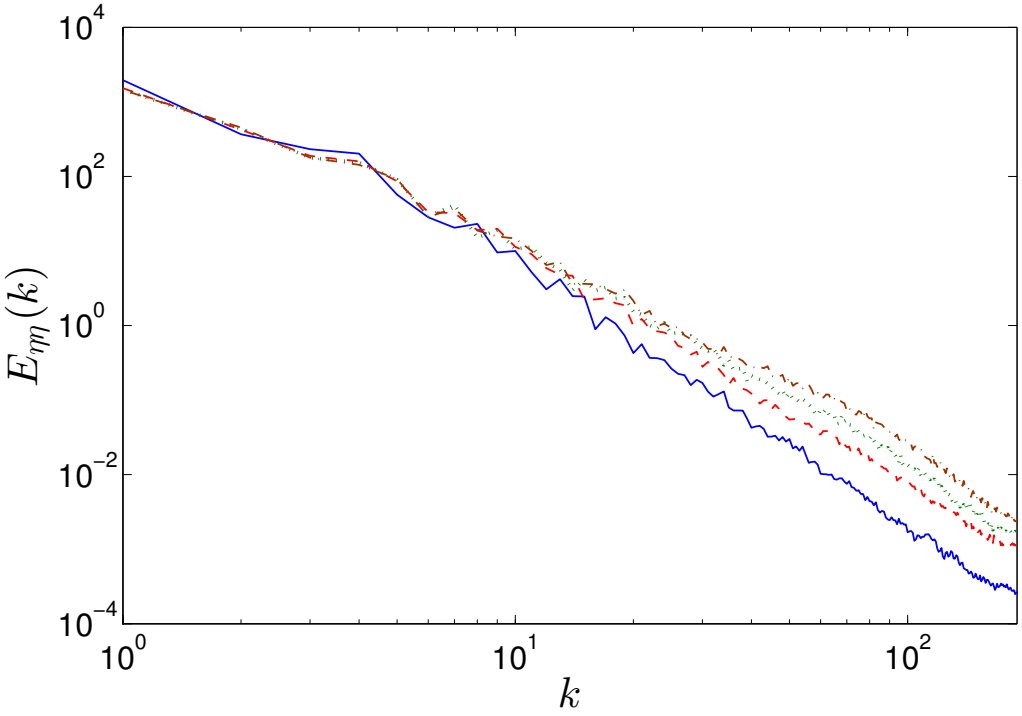

Figure C-2: Energy spectrum of the free surface height $E_{\eta\eta}(k_1)$ as a function of k at different We for $Fr^2 = 10$ at $t = 80$. Solid, $We = 1000$; Dash, $We = 4000$; Dotted, $We = 10000$; Dash-dot, $We = \infty$;

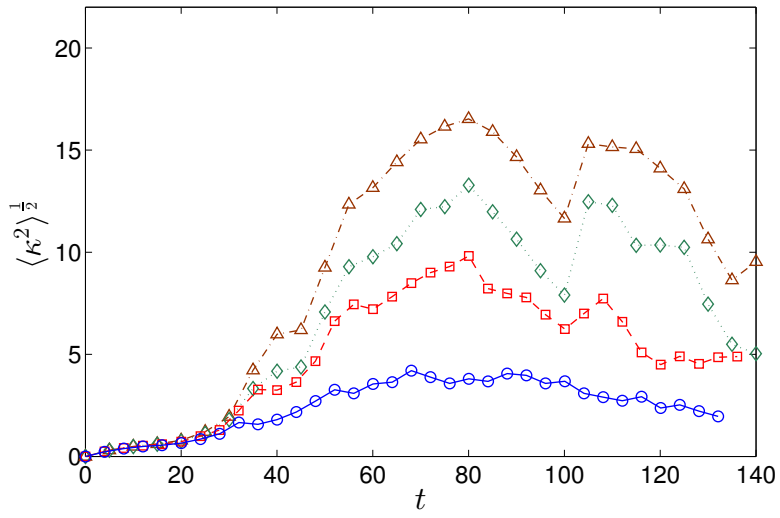

(a)

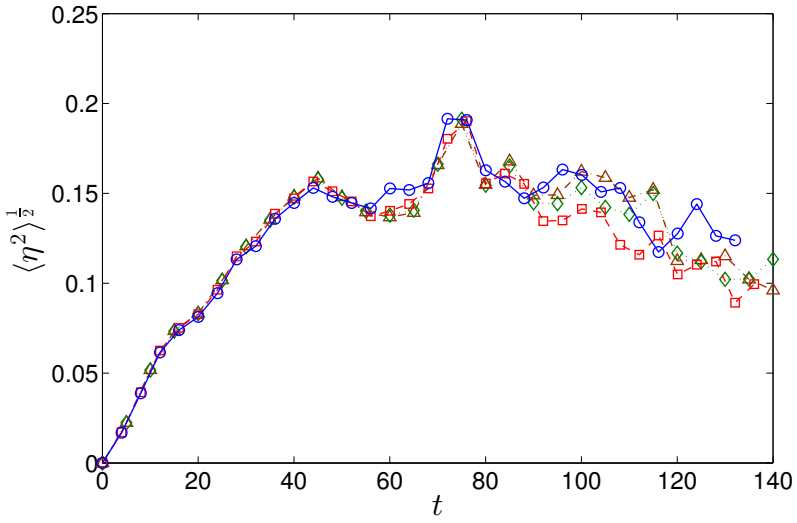

(b)

Figure C-3: Time evolution of (a) average surface curvature $\langle \kappa^2 \rangle^{1/2}$ and (b) average surface elevation $\langle \eta^2 \rangle^{1/2}$ at different We for $Fr^2 = 10$. $\circ$, $We = 1000$; $\square$, $We = 4000$; $\Diamond$, $We = 10000$; $\triangle$, $We = \infty$.

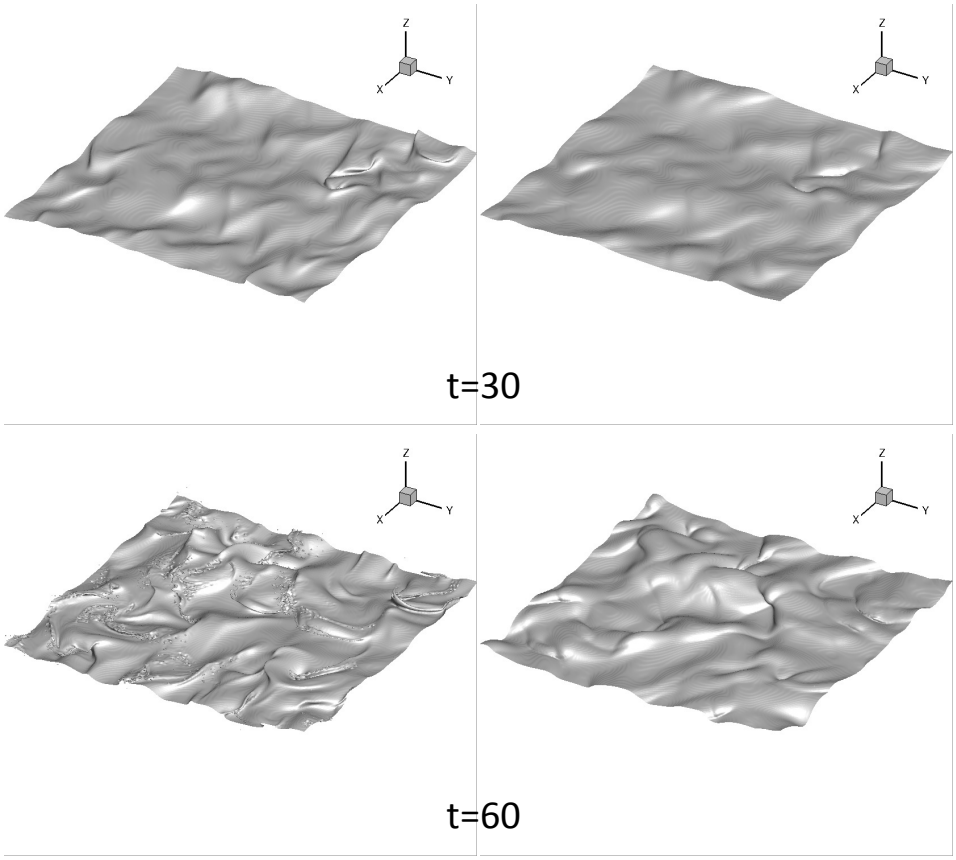

Figure C-4: Instantaneous iso-surface of volume fraction $f = 0.5$ at two times ($t = 30$ and $t = 60$) with (left column) $We = \infty$ and (right column) $We = 1000$

The value of $\langle \kappa^2 \rangle^{1/2}$ is observed to drop dramatically as We decreases, which confirms the strong suppression of surface tension on the small scaled surface deformations. Instead, the plots of the average surface elevation $\langle \eta^2 \rangle^{1/2}$ at different We overlap with each other as shown in figure C-3(b), indicating the effect of surface tension on large scaled surface deformations is limited. Figure C-4 provides a visual illustration of the effect of surface tension on the free surface deformation by comparing the free surfaces (instantaneous iso-surface of volume fraction $f = 0.5$) of $We = \infty$ and $We = 1000$. With negligible surface tension, many small and sharp structures appear on the free surface as shown in the left column of figure C-4. When surface tension becomes strong, these sharp structures are smoothed out as shown in the right column and the free surface is mainly characterized by deformations with relatively large length scales.

Bibliography

André, M. A. & Bardet, P. M. 2017 Free surface over a horizontal shear layer: vorticity generation and air entrainment mechanisms. *J. Fluid Mech.* **813**, 1007–1044.

Blenkinsopp, C. E. & Chaplin, J. R. 2010 Bubble size measurements in breaking waves using optical fiber phase detection probes. *IEEE J. Ocean. Engng* **35** (2), 388–401.

Borue, V., Orszag, S. A. & Staroselsky, I. 1995 Interaction of surface waves with turbulence: direct numerical simulations of turbulent open-channel flow. *J. Fluid Mech.* **286**, 1–23.

Brackbill, J. U., Kothe, D. B. & Zemach, C. 1992 A continuum method for modeling surface tension. *J. Comput. Phys.* **100** (2), 335–354.

Brocchini, M. 2002 Free surface boundary conditions at a bubbly/weakly splashing air-water interface. *Phys. Fluids* **14** (6), 1834–1840.

Brocchini, M. & Peregrine, D. H. 2001*a* The dynamics of strong turbulence at free surfaces. part 1. description. *J. Fluid Mech.* **449**, 225–254.

Brocchini, M. & Peregrine, D. H. 2001*b* The dynamics of strong turbulence at free surfaces. part 2. free-surface boundary conditions. *J. Fluid Mech.* **449**, 255–290.

Campbell, B. K. 2015 A mechanistic investigation of nonlinear interfacial instabilities leading to slug formation in multiphase flows. PhD thesis, Massachusetts Institute of Technology.

Chachereau, Y. & Chanson, H. 2011 Free-surface fluctuations and turbulence in hydraulic jumps. *Exp. Therm. Fluid Sci.* **35** (6), 896–909.

Chanson, H. & Toombes, L. 2003 Strong interactions between free-surface aeration and turbulence in an open channel flow. *Exp. Thermal and Fluid Science* **27** (5), 525–535.

Cormen, T. H., Leiserson, C. E., Rivest, R. L. & Stein, C. 2009 *Introduction to algorithms*. MIT press.

Cummins, S. J., Francois, M. M. & Kothe, D. B. 2005 Estimating curvature from volume fractions. *Computers & structures* **83** (6-7), 425–434.

Deane, G. B. & Stokes, M. D. 2002 Scale dependence of bubble creation mechanisms in breaking waves. *Nature* **418** (6900), 839–844.

Deike, L., Melville, W. K. & Popinet, S. 2016 Air entrainment and bubble statistics in breaking waves. *J. Fluid Mech.* **801**, 91–129.

Falgout, R. D., Jones, J. E. & Yang, U. M. 2006 The design and implementation of hypre, a library of parallel high performance preconditioners. In *Numerical Solution of Partial Differential Equations on Parallel Computers*, pp. 267–294. Springer.

Falgout, R. D. & Yang, U. M. 2002 hypre: A library of high performance preconditioners. *Computational Science — ICCS 2002* pp. 632–641.

Fulgosi, M., Lakehal, D., Banerjee, S. & De Angelis, V. 2003 Direct numerical simulation of turbulence in a sheared air–water flow with a deformable interface. *J. Fluid Mech.* **482**, 319–345.

Garrett, C., Li, M. & Farmer, D. 2000 The connection between bubble size spectra and energy dissipation rates in the upper ocean. *J. Phys. Oceanogr.* **30** (9), 2163–2171.

Guo, X. & Shen, L. 2010 Interaction of a deformable free surface with statistically steady homogeneous turbulence. *J. Fluid Mech.* **658**, 33–62.

Handler, R. A., Swean, T. F., Leighton, R. I. & Swearingen, J. D. 1993 Length scales and the energy balance for turbulence near a free surface. *AIAA journal* **31** (11), 1998–2007.

Hinze, J. O. 1955 Fundamentals of the hydrodynamic mechanism of splitting in dispersion processes. *AIChE* **1** (3), 289–295.

Hong, W. L & Walker, D. T. 2000 Reynolds-averaged equations for free-surface flows with application to high-froude-number jet spreading. *J. Fluid Mech.* **417**, 183–209.

Hunt, J. C. R., Stretch, D. D. & Belcher, S. E. 2011 Viscous coupling of shear-free turbulence across nearly flat fluid interfaces. *J. Fluid Mech.* **671**, 96–120.

Lewis, D. A. 1982 Bubble splitting in shear flow. *Trans. Inst. Chem. Eng.* **60**, 283–291.

Loewen, M. R., O'Dor, M. A. & Skafel, M. G. 1996 Bubbles entrained by mechanically generated breaking waves. *J. Geophys. Res.* **101** (C9), 20759–20769.

Lundgren, T. S. 2003 Linearly forced isotropic turbulence. *Tech. Rep.*. Minnesota Univ. Minneapolis.

Ma, J., Oberai, A. A., Drew, D. A., Lahey J., Richard T. & Hyman, M. C. 2011 A comprehensive sub-grid air entrainment model for rans modeling of free-surface bubbly flows. *J. Comput. Multiphase Flows* **3** (1), 41–56.

MARTÍNEZ-BAZÁN, C., Montanes, J. L. & Lasheras, J. C. 1999 On the breakup of an air bubble injected into a fully developed turbulent flow. part 1. breakup frequency. *J. Fluid Mech.* **401**, 157–182.

Mattingly, G. E. & Criminale, W. O. 1972 The stability of an incompressible two-dimensional wake. *J. Fluid Mech.* **51** (2), 233–272.

Morales, J. J., Nuevo, M. J. & Rull, L. F. 1990 Statistical error methods in computer simulations. *J. Comput. Phys.* **89** (2), 432–438.

Mortazavi, M., Le Chenadec, V., Moin, P. & Mani, A. 2016 Direct numerical simulation of a turbulent hydraulic jump: turbulence statistics and air entrainment. *J. Fluid Mech.* **797**, 60–94.

Murzyn, F., Mouaze, D. & Chaplin, J. R. 2007 Air-water interface dynamic and free surface features in hydraulic jumps. *J. Hydraul. Res.* **45** (5), 679–685.

Nagaosa, R. 1999 Direct numerical simulation of vortex structures and turbulent scalar transfer across a free surface in a fully developed turbulence. *Phys. Fluids (1994-present)* **11** (6), 1581–1595.

Ohring, S. & Lugt, H. J. 1991 Interaction of a viscous vortex pair with a free surface. *J. Fluid Mech.* **227**, 47–70.

Pan, Y. & Banerjee, S. 1995 A numerical study of free-surface turbulence in channel flow. *Phys. Fluids (1994-present)* **7** (7), 1649–1664.

Pope, S. B. 2001 Turbulent flows.

Popinet, S. 2009 An accurate adaptive solver for surface-tension-driven interfacial flows. *J. Comput. Phys.* **228** (16), 5838–5866.

Prosperetti, A. 1981 Motion of two superposed viscous fluids. *Phys. Fluids (1958-1988)* **24** (7), 1217–1223.

Rogers, M. M. & Moin, P. 1987 The structure of the vorticity field in homogeneous turbulent flows. *J. Fluid Mech.* **176**, 33–66.

Rojas, G. & Loewen, M. R. 2007 Fiber-optic probe measurements of void fraction and bubble size distributions beneath breaking waves. *Exp. Fluids* **43** (6), 895–906.

Sarpkaya, T. & Suthon, P. 1991 Interaction of a vortex couple with a free surface. *Exp. Fluids* **11** (4), 205–217.

Savelsberg, R. & van de Water, W. 2008 Turbulence of a free surface. *Phys. Rev. Lett* **100** (3), 034501.

Savelsberg, R. & van de Water, W. 2009 Experiments on free-surface turbulence. *J. Fluid Mech.* **619**, 95–125.

Shen, L., Triantafyllou, G. S. & Yue, D. K. P. 2000 Turbulent diffusion near a free surface. *J. Fluid Mech.* **407**, 145–166.

Shen, L., Triantafyllou, G. S. & Yue, D. K. P. 2001 Mixing of a passive scalar near a free surface. *Phys. Fluids (1994-present)* **13** (4), 913–926.

Shen, L. & Yue, D. K. P. 2001 Large-eddy simulation of free-surface turbulence. *J. Fluid Mech.* **440**, 75–116.

Shen, L., Zhang, X., Yue, D. K. P. & Triantafyllou, G. S. 1999 The surface layer for free-surface turbulent flows. *J. Fluid Mech.* **386**, 167–212.

Smolentsev, S. & Miraghaie, R. 2005 Study of a free surface in open-channel water flows in the regime from “weak" to “strong" turbulence. *Intl J. Multiphase flow* **31** (8), 921–939.

Tryggvason, G., Scardovelli, R. & Zaleski, S. 2011 *Direct numerical simulations of gas–liquid multiphase flows*. Cambridge University Press.

Tsai, W.-T 1998 A numerical study of the evolution and structure of a turbulent shear layer under a free surface. *J. Fluid Mech.* **354**, 239–276.

Walker, D. T., Chen, C.-Y & Willmarth, W. W. 1995 Turbulent structure in free-surface jet flows. *J. Fluid Mech.* **291**, 223–261.

Walker, D. T., Leighton, R. I. & Garza-Rios, L. O. 1996 Shear-free turbulence near a flat free surface. *J. Fluid Mech.* **320**, 19–51.

Wang, Z., Yang, J. & Stern, F. 2016 High-fidelity simulations of bubble, droplet and spray formation in breaking waves. *J. Fluid Mech.* **792**, 307–327.

Weymouth, G. D. & Yue, D. K. P. 2010 Conservative volume-of-fluid method for free-surface simulations on cartesian-grids. *J. Comput. Phys.* **229** (8), 2853–2865.

Yamamoto, Y. & Kunugi, T. 2011 Direct numerical simulation of a high-froude-number turbulent open-channel flow. *Phys. Fluids (1994-present)* **23** (12), 125108.

Yu, D. & Tryggvason, G. 1990 The free-surface signature of unsteady, two-dimensional vortex flows. *J. Fluid Mech.* **218**, 547–572.

Yu, X., Hendrickson, K. & Yue, D. K. P. 2016 Air entrainment in free-surface turbulence. In *Proc. 31st Symposium on Naval Hydrodynamics, Monterey, CA, USA*.

Zhang, C., Shen, L. & Yue, D. K. P. 1999 The mechanism of vortex connection at a free surface. *J. Fluid Mech.* **384**, 207–241.